

Finite Temperature Dynamics
of
One-Dimensional Quantum Magnets

Von der Fakultät für Mathematik und Physik
der Gottfried Wilhelm Leibniz Universität Hannover

zur Erlangung des Grades
Doktor der Naturwissenschaften
– Dr. rer. nat. –

genehmigte Dissertation

von

Dipl.-Phys. Carsten Luckmann
geboren am 10. Oktober 1973 in Hannover

2008

Copyright © 2007 by Carsten Luckmann. All rights reserved.

This book or any part thereof must not be reproduced in any form without the written permission of the publisher.

Typeset by \LaTeX , $\mathcal{A}\mathcal{M}\mathcal{S}$ - \LaTeX , and the memoir class.
Typeset in Minion.

Referent: Prof. Dr. H.-J. Mikeska
Korreferent: Prof. Dr. H. Frahm
Tag der Promotion: 23. November 2007

Zusammenfassung

In der vorliegenden Arbeit wird die Dynamik ein- bzw. quasi-eindimensionaler, antiferromagnetischer $S = \frac{1}{2}$ Quantenspinsysteme über einen großen Bereich von Frequenzen, externen Magnetfeldern und insbesondere endlichen Temperaturen untersucht. Die dynamischen Strukturfaktoren werden durch numerische Berechnung von Spinoperator-Matrixelementen basierend auf allen Eigenenergien und Eigenfunktionen, die durch vollständige, exakte Diagonalisierung gewonnen werden, bestimmt.

Der erste Teil dieser Arbeit untersucht die Dynamik der alternierenden, antiferromagnetischen Heisenberg-Kette anhand von spezifischer Wärme und dynamischen Strukturfaktoren für Ketten mit bis zu 20 Spins. Die Auswertung der Ergebnisse erfolgt unter Anlehnung an die analytischen Ergebnisse des Grenzfalls der nicht wechselwirkenden Dimer, was bis zu einem Verhältnis $\lambda \lesssim 0.3$ der Kopplungsstärken qualitativ gültig ist. Den Betrachtungen der spezifischen Wärme und des integrierten Strukturfaktors folgt die Analyse des Verhalten des zentralen, des Ein- und des Zweimagnonen-Peaks des longitudinalen und transversalen Strukturfaktors in Abhängigkeit von Impulsübertrag, Temperatur und Magnetfeld.

Der zweite Teil untersucht die rautenförmige Kette (engl.: distorted diamond chain), eine Variante der antiferromagnetischen Heisenberg-Kette mit übernächster-Nachbar-Wechselwirkung mit bis zu 18 Spins. Die Auswertung stützt sich dabei auf die elementaren Blöcke Dimer und Tetramer und behandelt sowohl die spin-flüssigen Phase als auch die Tetramer-Dimer Phase. Die spin-flüssige Phase wird durch eine niederenergetische, effektive antiferromagnetische Heisenberg-Kette und hochenergetischen Dimeranregungen charakterisiert, die durch ein Magnetisierungsplateau bei $\frac{1}{3}$ charakterisiert wird. Die Tetramer-Dimer Phase besitzt einen zweifach ($3N$ gerade) bzw. $\frac{2}{3}$ -fach ($3N$ ungerade) entarteten Grundzustand und weist Solitonen als elementare Anregungen auf. Das Verhalten wird auf zwei Pfaden im Phasendiagramm, die den Kosterlitz-Thouless Phasenübergang überqueren, anhand der spezifischen Wärme untersucht.

Schlagworte: Dynamischer Strukturfaktor, Heisenberg-Modell, Quantenspinsysteme

PACS: 75.10.Jm, 75.10.Pq, 75.40.Gb, 78.70.Nx

Abstract

In this thesis I examine the dynamics of one-dimensional or quasi one-dimensional, anti-ferromagnetic, $S = \frac{1}{2}$ quantum spin systems over a broad range of frequencies, external magnetic fields and in particular finite temperatures. Dynamic structure factors are calculated numerically from spin operator matrix elements based on all eigenenergies and eigenfunctions obtained by full exact diagonalization.

In the first part of this thesis, I investigate the dynamics of the bond alternating Heisenberg antiferromagnetic chain by means of specific heat and dynamic structure factors for chains of up to 20 spins. The interpretation of the results is based on the analytic results of the non-interacting dimer limit, which is qualitatively valid up to a coupling ratio $\lambda \lesssim 0.3$. Following the discussion of the specific heat and the integrated (exclusive) structure factors, I analyse the behaviour of the central, one-magnon, and two-magnon peak of the longitudinal and transverse structure factor with respect to transferred momentum, temperature, and magnetic field.

In the second part, I examine the distorted diamond chain, a variant of the Heisenberg antiferromagnetic chain with next-nearest neighbour interaction with up to 18 spins. The analysis is based on the fundamental building blocks dimer and tetramer and covers the spin-fluid as well as the tetramer-dimerized phase. The spin-fluid phase is characterized by a low energetic, effective Heisenberg antiferromagnetic chain and high energetic dimer excitations, which are separated by a $\frac{1}{3}$ magnetization plateau. The tetramer-dimerized phase features a twofold ($3N$ even) or $N/3$ -fold ($3N$ odd) degenerate ground state and show solitons as low energetic excitations. By means of the specific heat, I investigate the behaviour of the distorted diamond chain on two paths in the phase diagram crossing the Kosterlitz-Thouless phase transition.

Keywords: dynamic structure factor, Heisenberg model, quantum spin systems

PACS: 75.10.Jm, 75.10.Pq, 75.40.Gb, 78.70.Nx

Contents

Contents	7
List of Figures	9
List of Tables	13
1 Introduction	15
2 The Bond Alternating Heisenberg Chain	19
2.1 Introduction	19
2.2 The non-interacting dimer limit	22
2.3 The dynamic structure factor in an isotropic set-up	26
2.4 The dynamic structure factor in an external magnetic field	34
2.4.1 Specific Heat	37
2.4.2 Qualitative Properties of the Dynamic Structure Factor	39
2.4.3 The Dynamic Structure Factor at Zero Temperature	47
2.4.4 The dynamic structure factor at finite temperature	49
3 The Diamond Type Chain	97
3.1 Introduction	97
3.1.1 Hamiltonian of the diamond chain	97
3.1.2 The symmetric tetramer	99
3.1.3 The distorted tetramer	100
3.1.4 The quantum phase diagram of the diamond chain	100
3.2 Excitations in the spin fluid regime	107
3.2.1 Effective Heisenberg model	107

CONTENTS

3.3	Excitations in the tetramer-dimerized regime	112
3.4	Specific heat	116
4	Conclusion	125
	Appendix	129
A	The Numerical Approach	131
A.1	Diagonalization	132
A.2	Dynamic structure factor	133
A.3	Specific heat	136
	Bibliography	139
	Publications	145
	Acknowledgements	147
	Index	151

List of Figures

2.1	Schematic diagram of the bond alternating Heisenberg chain	19
2.2	Density of states for $N = 20, \lambda = 0.30, q = \pi$	22
2.3	Density of states for $N = 16, \lambda = 0.30, q = \pi$	23
2.4	Density of states for $N = 16, \lambda = 0.45, q = \pi$	24
2.5	Density of states for $N = 16, \lambda = 0.60, q = \pi$	25
2.6	Exclusive structure factors vs. q	27
2.7	Exclusive structure factors vs. T	28
2.8	$S^{zz}(q, \omega)$ overall picture	29
2.9	$S^{zz}(q, \omega)$ one-magnon peak	30
2.10	$S^{zz}(q, \omega)$ central peak	31
2.11	$S^{zz}(q, \omega)$ two-magnon peak	33
2.12	$S^{zz}(\pi, \omega)$ two-magnon peak, comparison of $N = 16$ and $N = 20$	34
2.13	Magnetization curve of the bond alternating Heisenberg chain	37
2.14	Dependence of the energy spectrum on the magnetic field	38
2.15	Specific heat of non-interacting dimers and $\lambda = 0.3J$ vs. T	40
2.16	Specific heat vs. T for $N = 20, H = 0.8J$ and $\lambda = 0.1, 0.3,$ and 0.5	41
2.17	Specific heat vs. T for $N = 20, H = 0.9J$ and $\lambda = 0.1, 0.3,$ and 0.5	41
2.18	Specific heat vs. T for $N = 20, H = 1.0J$ and $\lambda = 0.1, 0.3,$ and 0.5	42
2.19	Specific heat vs. T for $N = 20, H = 1.1J$ and $\lambda = 0.1, 0.3,$ and 0.5	42
2.20	$C(T)$ at low T for $\lambda = 0.3, N = 20,$ and $H = 1.1J$	43
2.21	Magnetic field dependence of single dimer transitions.	44
2.22	Exclusive structure factors $I^{zz}(\pi, \omega)$ vs. H	52
2.23	Exclusive structure factors $I^{+-}(\pi, \omega)$ vs. H	54
2.24	$S^{zz}(q, \omega)$ vs. M	55
2.25	$S^{+-}(q, \omega)$ vs. M	55

LIST OF FIGURES

2.26	ln($S^{zz}(q, \omega)$) vs. ln(N)	56
2.27	ln($S^{+-}(q, \omega)$) vs. ln(N)	56
2.28	One-magnon contributions to ln $S^{zz}(q, \omega)$ vs. ω	57
2.29	$S^{zz}(\pi, \omega)$ for $N = 16$ and $H = 1.01J$	58
2.30	$S^{zz}(2\pi, \omega)$ for $N = 16$ and $H = 1.01J$	60
2.31	$S^{zz}(\pi, \omega)$ for $N = 20$ and $T = 0.01J$	62
2.32	$S^{zz}(\pi, \omega)$ for $N = 16$ and $T = 0.01J$	63
2.33	$S^{zz}(\pi, \omega)$ for $N = 16$ and $T = 0.03J$	64
2.34	$S^{zz}(\pi, \omega)$ for $N = 16$ and $T = 0.10J$	65
2.35	$S^{zz}(\pi, \omega)$ for $N = 16$ and $T = 1.00J$	66
2.36	$S^{zz}(2\pi, \omega)$ for $N = 20$ and $T = 0.01J$	67
2.37	$S^{zz}(2\pi, \omega)$ for $N = 16$ and $T = 0.01J$	68
2.38	$S^{zz}(2\pi, \omega)$ for $N = 16$ and $T = 0.03J$	69
2.39	$S^{zz}(2\pi, \omega)$ for $N = 16$ and $T = 0.10J$	70
2.40	$S^{zz}(2\pi, \omega)$ for $N = 16$ and $T = 1.00J$	71
2.41	Two-magnon peak of $S^{zz}(q, \omega)$ for $N = 20$ and $T = 0.01J$	72
2.42	Two-magnon peak of $S^{zz}(q, \omega)$ for $N = 16$ and $T = 0.01J$	73
2.43	Two-magnon peak of $S^{zz}(q, \omega)$ for $N = 16$ and $T = 0.03J$	74
2.44	Two-magnon peak of $S^{zz}(q, \omega)$ for $N = 16$ and $T = 0.10J$	75
2.45	$S^{+-}(\pi, \omega)$ at magnetization $M = N/4 - 1$	78
2.46	$S^{+-}(2\pi, \omega)$ at magnetization $M = N/4 - 1$	80
2.47	$S^{+-}(\pi, \omega)$ for $N = 20$ and $T = 0.01J$	82
2.48	$S^{+-}(\pi, \omega)$ for $N = 16$ and $T = 0.01J$	83
2.49	$S^{+-}(\pi, \omega)$ for $N = 16$ and $T = 0.03J$	84
2.50	$S^{+-}(\pi, \omega)$ for $N = 16$ and $T = 0.1J$	85
2.51	$S^{+-}(\pi, \omega)$ for $N = 12$ and $T = 0.1J$	86
2.52	$S^{+-}(\pi, \omega)$ for $N = 12$ and $T = 1.0J$	87
2.53	$S^{+-}(2\pi, \omega)$ for $N = 20$ and $T = 0.01J$	88
2.54	$S^{+-}(2\pi, \omega)$ for $N = 16$ and $T = 0.01J$	89
2.55	$S^{+-}(2\pi, \omega)$ for $N = 16$ and $T = 0.03J$	90
2.56	$S^{+-}(2\pi, \omega)$ for $N = 16$ and $T = 0.1J$	91
2.57	$S^{+-}(2\pi, \omega)$ for $N = 12$ and $T = 0.1J$	92
2.58	$S^{+-}(2\pi, \omega)$ for $N = 12$ and $T = 1.0J$	93
2.59	Two-magnon peak of $S^{+-}(q, \omega)$ for $N = 16$ and $T = 0.01J$	94
2.60	Two-magnon peak of $S^{+-}(q, \omega)$ for $N = 16$ and $T = 0.03J$	95
2.61	Two-magnon peak of $S^{+-}(q, \omega)$ for $N = 16$ and $T = 0.10J$	96
3.1	Schematic diagram of the diamond chain	98
3.2	The symmetric tetramer	99

LIST OF FIGURES

3.3	The distorted tetramer	102
3.4	Phase diagram of the diamond chain	104
3.5	Ground states of the symmetric diamond chain for $\gamma < 1$	105
3.6	Ground states of the symmetric diamond chain for $\gamma > 1$ and N_3 even	106
3.7	Ground states of the symmetric diamond chain for $\gamma > 1$ and N_3 odd	112
3.8	Domain wall movement in the diamond chain	113
3.9	$C(T)$ of the $N = 18$ diamond chain with $J_1 = 0.60J$ and $H = 0$	118
3.10	$C(T)$ of the $N = 18$ diamond chain with $J_1 = 0.60J$ and $H = 0$	118
3.11	$C(T)$ of the $N = 18$ diamond chain with $J_1 = 0.60J$ and $J_3 = 0.05J$	119
3.12	$C(T)$ of the $N = 18$ diamond chain with $J_1 = 0.60J$ and $J_3 = 0.05J$	119
3.13	$C(T)$ of the $N = 18$ diamond chain with $J_1 = 0.60J$ and $J_3 = 0.25J$	120
3.14	$C(T)$ of the $N = 18$ diamond chain with $J_1 = 0.60J$ and $J_3 = 0.32J$	120
3.15	$C(T)$ of the $N = 18$ diamond chain with $J_1 = 0.60J$ and $J_3 = 0.38J$	121
3.16	$C(T)$ of the $N = 18$ diamond chain with $J_1 = 0.60J$ and $J_3 = 0.44J$	121
3.17	$C(T)$ of the $N = 18$ diamond chain with $J_1 = 0.60J$ and $J_3 = 0.55J$	122
3.18	$C(T)$ of the $N = 18$ diamond chain with $J_1 = 0.46$ and $J_3 = 0.44$	122
3.19	$C(T)$ of the $N = 18$ diamond chain with $J_1 = 0.48$ and $J_3 = 0.46$	123
3.20	$C(T)$ of the $N = 18$ diamond chain with $J_1 = 0.50$ and $J_3 = 0.48$	123
3.21	$C(T)$ of the $N = 18$ diamond chain with $J_1 = 0.52$ and $J_3 = 0.50$	124
3.22	$C(T)$ of the $N = 18$ diamond chain with $J_1 = 0.54$ and $J_3 = 0.52$	124

List of Tables

2.1	Critical fields for $\lambda = 0.3$ and $N = 12, 16,$ and $20.$	36
3.1	Eigenstates of the symmetric tetramer	101
3.2	Eigenstates of the distorted tetramer	103
3.3	18 spin diamond vs. 6 spin Heisenberg chain	108
3.4	18 spin diamond vs. 6 spin Heisenberg chain	109
3.5	18 spin diamond vs. 6 spin Heisenberg chain	110
3.6	Effective Heisenberg coupling	111
3.7	Tight binding model fit	115

CHAPTER 1

Introduction

Low dimensional antiferromagnetic quantum spin systems have been of interest over the past years and even decades. They offer an approach to some real world materials which are of limited complexity, which allows to unravel the details of quantum effects.

Until recently, theoretical and experimental analysis were difficult to unite, because the theoretical investigations mainly covered the quantum properties, ignoring thermal fluctuations. This restriction effectively reduces the spectrum to low-lying, excited states and therefore decreases the complexity of the system allowing for approximate analytical treatment or numerical computations, *e. g.*, using the Lanczos algorithm. Experimental results, on the other hand, were obtained at finite temperature where thermal fluctuations may cover quantum effects.

With the increase of computational power, it is possible to perform numerical calculations at almost arbitrary temperatures, using either approximate methods like DMRG applied to quantum transfer matrices[1] or full exact diagonalization. The former allows for larger system sizes and is therefore very attractive to be used and has already been applied in various works but lacks the ability to compute dynamic features of the underlying quantum model. The latter, being an exact procedure, is rather limited in the system size, but given an appropriate system with short correlations, it produces good results. Since full exact diagonalization offers the possibility to investigate dynamic features, I opted for the latter for this thesis.

The first system I will analyse in this thesis is conceptually very simple. The bond alternating Heisenberg chain, or short BAHC , consists of a set of coupled dimers, *i. e.*, pairs of strongly coupled spins $\frac{1}{2}$ whose interaction is sufficiently weak to not

close the dimer gap. Technically speaking, the Hamilton operator

$$\mathcal{H}_{\text{BAHC}} = J \sum_{n \text{ even}} (\vec{S}_n \cdot \vec{S}_{n+1} + \lambda \vec{S}_{n+1} \cdot \vec{S}_{n+2}) \quad (1.1)$$

is a generalization of the Heisenberg antiferromagnetic chain with alternating coupling strengths with a relative factor of λ . Without loss of generality, this coefficient is $0 \leq \lambda \leq 1$. The upper limit $\lambda = 1$ is well known as the Heisenberg antiferromagnetic chain, and the lower limit $\lambda = 0$ is a simple set of non-interacting dimers. In order to ensure sufficiently short correlations, I will limit my analysis to $\lambda \leq 0.3$, which is large enough to find real world materials, *e. g.*, $\text{Cu}(\text{NO}_3)_2$ with $\lambda \approx 0.23$, and the experimental results support the computations of this work.

The other system I will investigate is the distorted diamond chain, which can be interpreted as a variation of the Heisenberg antiferromagnetic chain with next-nearest neighbour interaction:

$$\begin{aligned} \mathcal{H}_{\text{DDC}} = \sum_{n=0,3,\dots} & J_1 (\vec{S}_n \cdot \vec{S}_{n+1} + \vec{S}_{n+2} \cdot \vec{S}_{n+3}) \\ & + J_2 \vec{S}_{n+1} \cdot \vec{S}_{n+2} \\ & + J_3 (\vec{S}_n \cdot \vec{S}_{n+2} + \vec{S}_{n+1} \cdot \vec{S}_{n+3}) \end{aligned} \quad (1.2)$$

where J_1 and J_2 correspond to the nearest neighbour and J_3 and 0 (one next-nearest neighbour interaction is not present) correspond to the next-nearest neighbour interactions.

The distorted diamond chain exhibits some interesting physical properties. For small J_1 and J_3 compared to J_2 , the quantum phase diagram features a spin-fluid phase with dimers along the J_2 bonds and a Heisenberg antiferromagnetic chain on the spins in between. For larger $J_1, J_3 < J_2$ the system enters a tetramer-dimer phase with tetramers formed from J_2 bonds with the two surrounding spins alternating with dimers on J_2 bonds. In contrast to the spin-fluid phase, low-lying excitations in this phase are found to be s.

Furthermore, the distorted diamond chain features a magnetization plateau at $1/3$ magnetization in the spin-fluid phase, which originates from the low energetic Heisenberg antiferromagnetic subsystem at its full magnetization.

One material currently of interest which can be described by a distorted diamond chain is azurite, and first experimental results support the calculations of this work.

The dynamics of such quantum systems are best discussed in terms of the dynamic structure factor, *i. e.*, the Fourier transform of the time dependent spin correlation function. Experimentally, the dynamic structure factor is proportional to

the spectral weight of the cross section of magnetic inelastic neutron scattering.

$$S^\alpha(q, \omega) \propto \sum_{n,i,f} e^{-\frac{\beta E_i}{k_B T}} \left| \langle f | e^{iqn} S_n^\alpha | i \rangle \right|^2 \delta(\omega - (E_f - E_i)) \quad (1.3)$$

Furthermore, given the full spectrum of these Hamiltonians the specific heat, which gives among others clues with respect to the excitation gap and the level distribution, can be computed for arbitrary temperatures and magnetic fields.

In Chapter 2 I will investigate and discuss the properties of the bond alternating Heisenberg chain. The distorted diamond chain will be discussed in Chapter 3. Finally, Chapter A gives a short view on the numerical methods.

The Bond Alternating Heisenberg Chain

2.1 Introduction

The bond alternating Heisenberg chain with periodic boundary conditions is a variant of the isotropic Heisenberg antiferromagnetic chain where every second bond has got a coupling strength $J' = \lambda J$. Additionally, these two alternating couplings are characterized by two distances. First, the lattice constant b is the inter-dimer distance, *i. e.*, the distance between equivalent spins in neighbouring dimers, and second, the intra-dimer distance d , which is the distance between the two spins of the same dimer. In this work I will mostly consider $d = \frac{b}{2}$, although in real world materials generally independent and different d and $\frac{b}{2}$ occur.

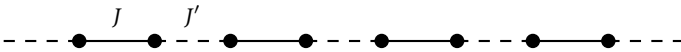


Figure 2.1: Schematic diagram of the bond alternating Heisenberg chain

$$\mathcal{H}_{\text{BAHC}} = \sum_j (J \vec{S}_{2j} \cdot \vec{S}_{2j+1} + J' \vec{S}_{2j+1} \cdot \vec{S}_{2j+2}) \quad (2.1a)$$

$$= \sum_j J (\vec{S}_{2j} \cdot \vec{S}_{2j+1} + \lambda \vec{S}_{2j+1} \cdot \vec{S}_{2j+2}) \quad (2.1b)$$

In the special case $\lambda = 1$, this system is equal to the ordinary, isotropic Heisenberg antiferromagnetic chain, but for other values of λ , it is obvious that the translational symmetry is reduced from a one spin to a two spin elementary cell. This feature is eminently prominent for $\lambda = 0$ where the bond alternating Heisenberg chain decomposes into a set of non-interacting dimers.

In contrast to the isotropic Heisenberg antiferromagnetic chain, which is gapless, the bond alternating Heisenberg chain is gapped for $\lambda \neq 1$. The lowest excited state is an $S^{\text{tot}} = 1$ magnon band. Higher excited states have been investigated in detail in [2].

The Hamilton operator of the bond alternating Heisenberg chain shows several conserved quantities. From rotational invariance follows immediately

$$[\mathcal{H}, S_{\text{tot}}] = 0 \quad (2.2a)$$

$$[\mathcal{H}, S_{\text{tot}}^z] = 0 \quad (2.2b)$$

As result, the Hilbert space can be divided into subspaces of constant, total spin projection S_{tot}^z .

Furthermore, the Hamilton operator is translationally invariant, implying commutation of Hamilton and translation (by two spins, hence the subscript 2 on T_2) operators

$$[\mathcal{H}, T_2] = 0. \quad (2.3)$$

As a consequence, it is possible to find a set of common eigenstates of both operators

$$\mathcal{H}|i, q\rangle = E_i|i, q\rangle \quad (2.4a)$$

$$T_2|i, q\rangle = e^{iqb}|i, q\rangle. \quad (2.4b)$$

where the newly introduced variable q is the wave vector with respect to the lattice of dimers with lattice constant b , where q can take the values

$$q = \frac{1}{b}(0 \dots 2\pi) \quad (2.5)$$

A wave vector definition adapted to homogeneously interacting ($\lambda = 1$) and equally spaced ($d = b/2$) N spins would give $\tilde{q} = \frac{1}{b/2}(0 \dots 2\pi) = \frac{1}{b}(0 \dots 4\pi)$. The transition from the dimer lattice to become the homogeneous chain implies a shifting of the second (degenerate) mode as second half of the larger Brillouin zone of the chain. I will also use the larger wave vector range $q = \frac{1}{b}(0 \dots 4\pi)$ for dimers instead of using two degenerate modes in the basic cell of the dimer lattice.

For an N -spin chain with $\frac{N}{2}$ cells of size b , $\frac{N}{2}$ translations reproduce the original state, thus $T_2^{\frac{N}{2}} \equiv 1$. This gives the following constraint on the wave vector q

$$q = \frac{2\pi}{\frac{N}{2}b} m, \quad m \in \{0, \dots, \frac{N}{2}\}. \quad (2.6)$$

However, some spin configurations, *e. g.*, $\uparrow\downarrow\uparrow\downarrow\uparrow\downarrow \cdots \uparrow\downarrow$, show a higher translational symmetry as they are already reproduced after $\frac{N}{2P_a}$, $P_a \geq 1$ translations T_2 , so not all values of q occur with the same number of eigenstates.

The respective eigenstates are then found to be

$$|i, q\rangle = \sqrt{\frac{2P_{a_i}}{N}} \sum_{j=0}^{\frac{N}{2P_{a_i}}-1} e^{iqj} T_2^j |a_i\rangle. \quad (2.7)$$

Here, $|a_i\rangle$ denotes a representing spin configuration, and the factor P_{a_i} accounts for a possibly higher symmetry of the spin configuration a_i .

The spectrum of the bond alternating Heisenberg chain as well as the dynamic structure factor at low temperatures ($T \ll J$) have been studied before by employing various techniques including random phase approximation [2], perturbation theory [3], and linked cluster expansion [4, 5, 6]. The following features of the spectrum have been found:

- (1) A gapped, propagating one-magnon excitation above the singlet ground state,
- (2) a two-magnon continuum as well as very small intensity higher magnon continua, and
- (3) one singlet and one triplet bound state below the two-magnon continuum.
These bound states are only distinguishable from the continuum for wave vectors close to $q = \pi$.

Studies of the dynamic structure factor have shown that the transition from the singlet ground state to the one-magnon triplet is the dominant excitation at low temperatures and low magnetic fields. For the values of $\lambda \neq 0$ I will consider, only the two-magnon continuum at $\omega \approx 2J$ quantitatively is of some importance, higher contributions are negligible.

Numerical calculations employing full, exact diagonalization require — like many other methods as well — a finite size system with a fixed number of particles N . For full, exact diagonalization the limit imposed on N by the available computing

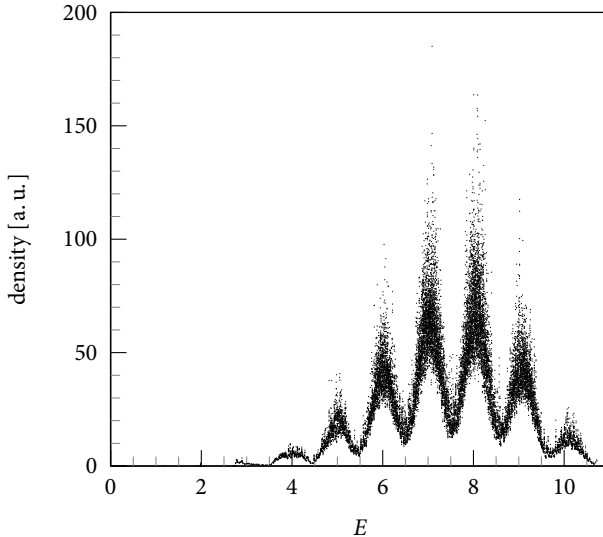


Figure 2.2: Density of states for $N = 20, \lambda = 0.30, q = \pi$

resources is rather low compared to DMRG, and so I need to ensure that the investigated system is dominated by short range interactions. In Figs. 2.2 to 2.5, the density of states of the bond alternating Heisenberg chain is depicted for $q = \pi$, $N = 20, \lambda = 0.30$ and $N = 16, \lambda = 0.30, \lambda = 0.45$ and $\lambda = 0.60$. At $\lambda = 0.30$ the band structure can be clearly seen for both $N = 20$ and $N = 16$, but at higher values of λ the band structure is blurred ($\lambda = 0.45$, Fig. 2.4) or completely destroyed ($\lambda = 0.60$, Fig. 2.5). It is therefore valid to assume dominating short range interactions for $\lambda \lesssim 0.30$. Experimental results with neutron scattering have confirmed my results. [7]

2.2 The non-interacting dimer limit

As mentioned before, the bond alternating Heisenberg chain reduces to a set of non-interacting dimers for $\lambda = 0$. The Hamilton operator becomes block-diagonal, decoupling into a sum of non-interacting two-spin systems. The eigenstates of each

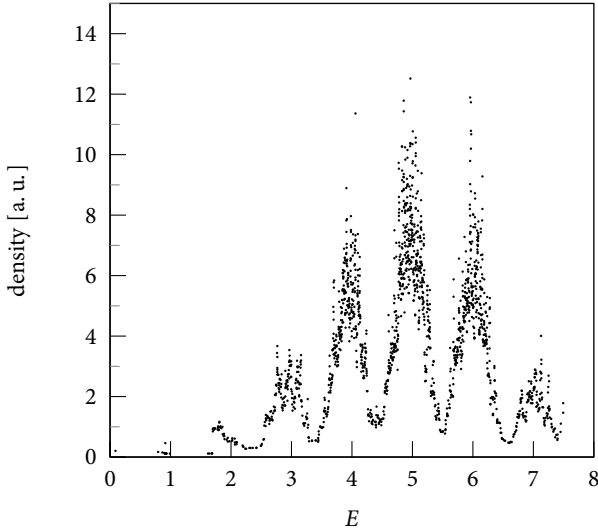


Figure 2.3: Density of states for $N = 16$, $\lambda = 0.30$, $q = \pi$

dimer are found to be a singlet ground state at energy $\varepsilon_0 = -\frac{3}{4}J$ and a triplet excited state at energy $\varepsilon_0 + J = \frac{1}{4}J$, and the partition function is $z = 1 + 3e^{-\beta J}$. The overall ground state is a product of dimer singlets, *i. e.*, a singlet with energy

$$E_0 = -\frac{N}{2} \frac{3}{4} J; \quad (2.8)$$

the overall partition function is

$$Z = (1 + 3e^{-\beta J})^{\frac{N}{2}}. \quad (2.9)$$

Then the dynamic structure factor turns out to be

$$S_{\lambda=0}^{zz}(q, \omega) = \frac{1}{2} S_{\lambda=0}^{+-}(q, \omega) = \frac{1}{2} S_{\lambda=0}^{-+}(q, \omega) = B_0(q, \beta) \delta(\omega) + B_1(q, \beta) [\delta(\omega - J) + e^{-\beta J} \delta(\omega + J)] \quad (2.10a)$$

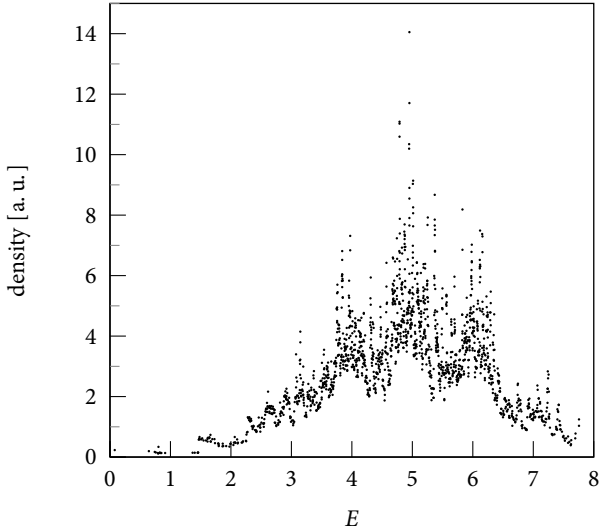


Figure 2.4: Density of states for $N = 16$, $\lambda = 0.45$, $q = \pi$

with

$$B_0(q, \beta) = \frac{1 + \cos(qd)}{3 + e^{\beta J}} \frac{1}{2} \quad (2.10b)$$

$$B_1(q, \beta) = \frac{1 - \cos(qd)}{3 + e^{\beta J}} \frac{e^{\beta J}}{4} \quad (2.10c)$$

The factors B_ℓ denote the weight of transitions with $\omega = \pm \ell J$. Thus, B_0 corresponds to the central peak, which in this system can only occur for transitions within the triplet excited state. B_1 corresponds to the sum of the one-magnon peak, *i. e.*, excitations from the singlet ground state to the triplet excited states and the corresponding inverse transitions, decorated with a factor $e^{-\beta J}$. Higher magnon peaks are not present in the non-interacting dimer limit due to the missing coupling between the dimers.

For $q = 0$, the central peak is maximal and the one-magnon peak vanishes, while for $q = 2\pi$ it is vice versa, the central peak vanishes and the one-magnon peak is maximal. Concerning the temperature dependence, the central peak vanishes for

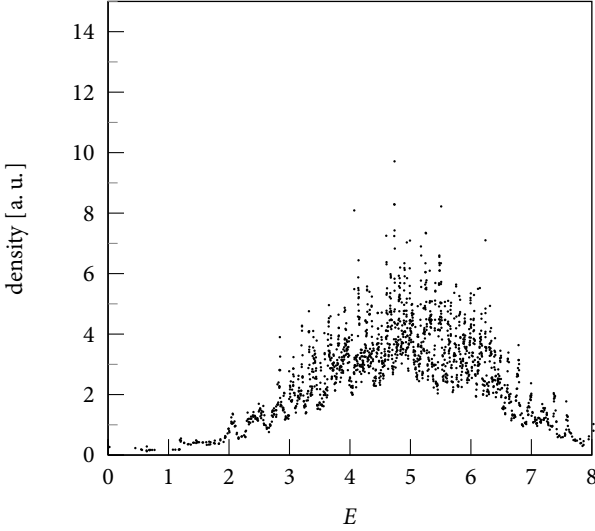


Figure 2.5: Density of states for $N = 16$, $\lambda = 0.60$, $q = \pi$

$T = 0$ and increases with higher T towards its maximum value at $T \rightarrow \infty$. The one-magnon peak on the other hand has its maximum value at $T = 0$ and decreases with higher T towards its limit at $T \rightarrow \infty$. Limiting values for these weights of particular interest are

$$B_0(q = 0, \beta) = \frac{1}{3 + e^{\beta J}} \quad B_0(q = \frac{2\pi}{b}, \beta) = 0 \quad (2.11a)$$

$$B_1(q = 0, \beta) = 0 \quad B_1(q = \frac{2\pi}{b}, \beta) = \frac{1}{3 + e^{\beta J}} \frac{e^{\beta J}}{2} \quad (2.11b)$$

$$B_0(q, T = 0) = 0 \quad B_0(q, T \rightarrow \infty) = \frac{1 + \cos(qd)}{8} \quad (2.11c)$$

$$B_1(q, T = 0) = \frac{1 - \cos(qd)}{4} \quad B_1(q, T \rightarrow \infty) = \frac{1 - \cos(qd)}{16} \quad (2.11d)$$

Central and one-magnon peak have equal weight for $\cos(qd) = \frac{1 - 2e^{-\beta J}}{1 + 2e^{-\beta J}}$ or $\beta J = \ln\left(2 \frac{1 + \cos(qd)}{1 - \cos(qd)}\right)$.

Introducing an external magnetic field, isotropy is lost and these formulae become field dependent. However, the extended formulae will be presented in context with the discussion of the field dependence of the dynamic structure factor in Section 2.4.

Although these formulae are only strictly valid for $\lambda = 0$, they set the frame for the behaviour in the range $0 < \lambda < 1$ as well. Due to the complete degeneracy of states in the non-interacting dimer limit, the central and one-magnon peaks are sharp for arbitrary temperature. With increasing inter-dimer coupling, the peaks broaden, but however, the exclusive structure factor defined in the next section can still be related to the results in the non-interacting dimer limit.

2.3 The dynamic structure factor in an isotropic set-up

In an isotropic set-up, the three dynamic structure factors $S^x(q, \omega)$, $S^y(q, \omega)$, and $S^z(q, \omega)$ have equal values and it is therefore sufficient to calculate $S^z(q, \omega)$, which alleviates the numerical problem in the sense that this structure factor only requires a diagonal matrix operation, reducing the order of complexity.

On the way from the non-interacting dimer limit to the dynamic structure factors for interacting dimers, I first want to discuss the exclusive structure factors, *i. e.*, the integrated structure factor over one peak.

$$I_n(q) = \int_{(n-\frac{1}{2})J}^{(n+\frac{1}{2})J} d\omega S(q, \omega) \quad (2.12)$$

For inter-dimer couplings $\lambda \lesssim 0.5$ the band gap is large enough to specify the boundaries between the peaks unambiguously.

In Fig. 2.6, the dependence of the exclusive structure factors I_n on the momentum transfer q is shown for a system of 16 spins with $\lambda = 0.3$. For comparison, the solid lines denote the analytic solution in the non-interacting dimer limit (non-zero for $n = 0$ and $n = 1$ only). Since I_0 vanishes for $q = 2\pi$, and I_1 and I_2 vanish for $q = 0$, I shall focus on $q = \pi$ in the following discussion. Other values of q are not easily comparable for finite chains, because the allowed q -values change with the system size, and thus the results for different system sizes cannot be compared directly.

For the same system, the dependence of the exclusive structure factors I_n on the temperature for $q = \pi$ is shown in Fig. 2.7. Again, the solid lines denote the analytic result in the non-interacting dimer limit. As to the numerical data I could not determine a difference for systems of 12 and 16 spins.

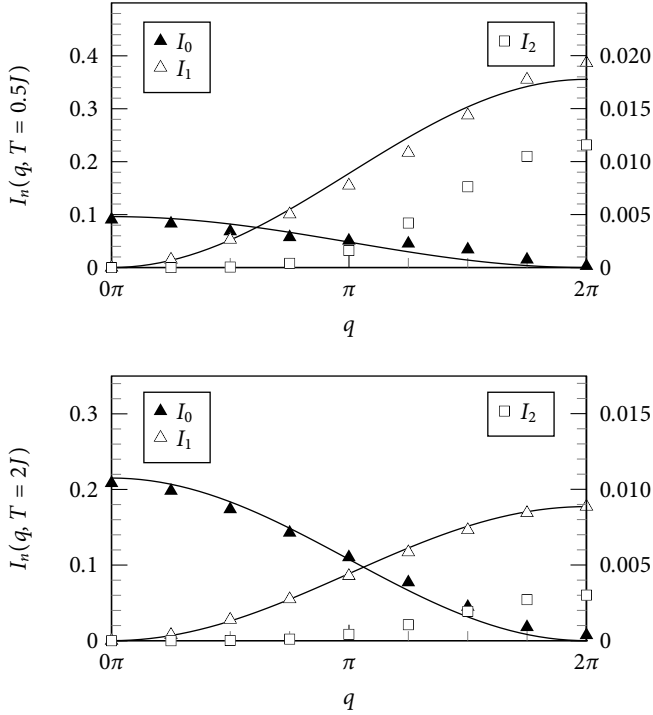


Figure 2.6: Exclusive structure factors vs. q for $N = 16$, $\lambda = 0.3$, and the two temperatures $T = 0.5$ and $T = 2$. The solid line corresponds to the analytic solution for $\lambda = 0$.

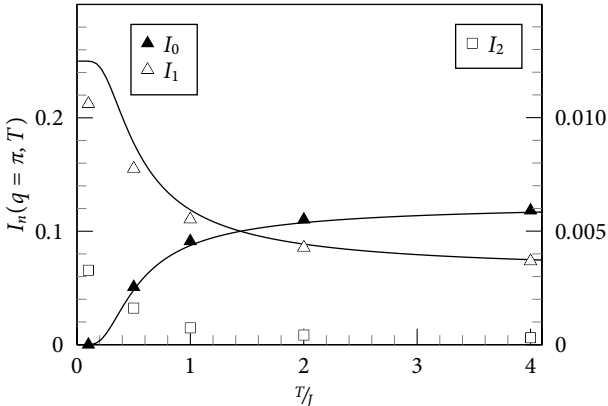


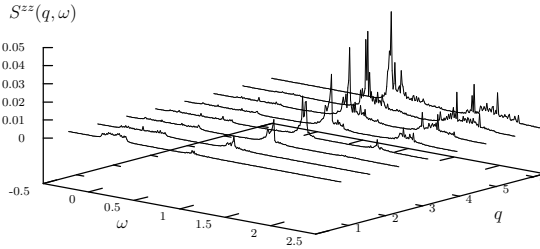
Figure 2.7: Exclusive structure factors I_n vs. T for $N = 16$, $\lambda = 0.30$, and $q = \pi$. The solid line corresponds to the analytic solution for $\lambda = 0$.

The good conformance of the data points with the analytic results for $\lambda = 0$ confirms the correctness of the numerical approach and demonstrates that many body quantum effects, *i. e.*, dimer interactions, are not important for the static quantities $I_0(q)$ and $I_1(q)$ up to $\lambda \lesssim 0.3J$.

An overall view of the dynamic structure factor $S^{zz}(q, \omega)$ is shown in Fig. 2.8. As already clear from Figs. 2.6 and 2.7, the weight of the central peak is maximal at $q = 0$ and vanishes at $q = 2\pi$, whereas the weights of the one- and two-magnon peaks vanish at $q = 0$ and are maximal at $q = 2\pi$. Similarly, the central peak increases with growing temperature whilst the one- and two-magnon peaks decrease.

The most prominent feature of the dynamic structure factor is the one-magnon peak, whose evolution with temperature is illustrated in Fig. 2.9 for $\lambda = 0.3$ and $N = 16$. With increasing temperature, the peaks extend over a nearly constant range in frequency, although the decrease of the maximum of intensity formally implies an increase in the width at half maximum. For both $q = \pi$ and 2π the position of the maximum shifts to lower frequencies, but the shape of the peak develops an asymmetry with more intensity on the high frequency side. This effect is most pronounced for $q = 2\pi$, *i. e.*, the wave vector of the energy gap, and may not be noticeable at all for small values of q , *cf.* Fig. 2.8. Thus the detailed description of

$S^{zz}(q, \omega)$ for $N = 16, \lambda = 0.3, T = 0.5$



$S^{zz}(q, \omega)$ for $N = 16, \lambda = 0.3, T = 2.0$

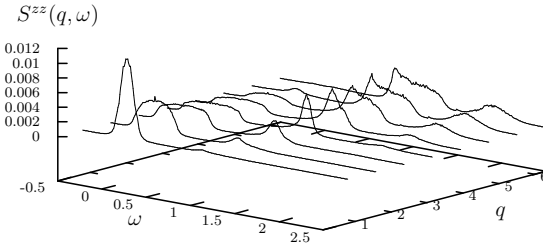


Figure 2.8: $S^{zz}(q, \omega)$ overall picture for $N = 16, \lambda = 0.3$, and temperatures (a) $T = 0.5$ and (b) $T = 2.0$. The two-magnon peak has been enlarged by a factor 20 for visibility.

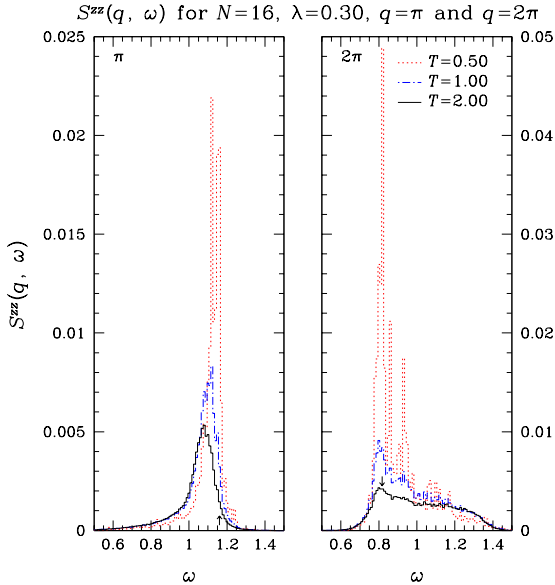


Figure 2.9: $S^{zz}(q, \omega)$ one-magnon peak. The resolution $\Delta\omega$ is 0.02,

the line shape provides an understanding of the intriguing observation that the gap energy seems to increase with temperature [8] (comparable to an analogous observation in the Haldane chain [9, 10, 11]). It would certainly be interesting to compare the line shape to the result of the theoretical approach of [12], however, with $N = 16$ a continuous line shape results only for temperatures above the energy gap and is thus in the non-universal approach of [12]. When looking at the microscopic origin of the peak broadening, one finds that, *e. g.*, at $T = J$ the basic transition from the ground state to the one-magnon excitation at $q = \pi$ is responsible for 30 % of the weight at that frequency and that for the neighbouring frequencies transitions starting from the one-magnon band contribute about 10 % of the total weight, whereas the by far largest part of the intensity originates from transitions starting at states with two or more excited dimers.

The one-magnon peak represents transitions from one band to the next higher band, the central peak represents transitions within one single band. Compared to the central peak, the one-magnon peak is larger — especially at lower temperatures — because it includes transitions from the singlet ground state, which are present without thermal excitation.

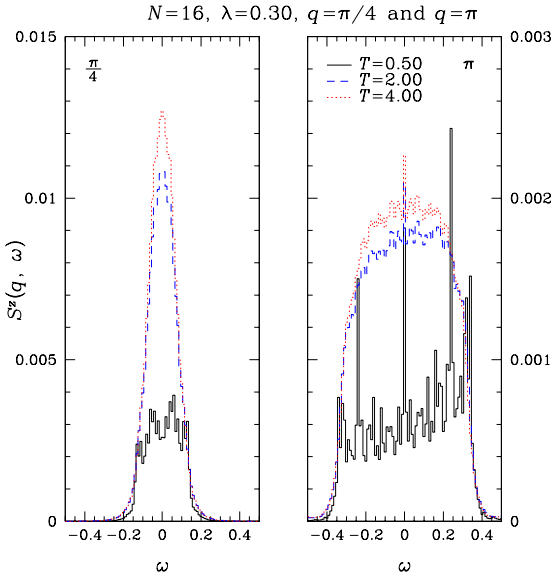


Figure 2.10: $S^{zz}(q, \omega)$ central peak. The resolution $\Delta\omega$ is 0.02.

Fig. 2.10 illustrates for $\lambda = 0.3$, $N = 16$, and $q = \pi/4$ and π the evolution of the central peak with temperature. At zero temperature, the central peak vanishes (*cf.* Fig. 2.7). At low temperatures and $\lambda \ll 1$, the shape of the central peak is dominated by transitions within the weakly interacting one-magnon band with q -independent matrix elements, seen as spikes in the $T = 0.5J$ curve of Fig. 2.10b. With increasing temperature, transitions within higher bands become more and more relevant, which can be seen in the increasing background in Fig. 2.10b. The physical process may be thought of as an external probe accelerating a thermally

populated excitation and is thus similar to well known processes in soliton bearing one-dimensional magnets [13]. As in these models, the limiting form of the structure factor is

$$S_{(0)}^{zz}(q, \omega) \propto e^{-\beta J} \frac{1}{\sqrt{1 - \frac{\omega^2}{\omega_m^2(q)}}} \theta(\omega_m^2(q) - \omega^2) \quad (2.13)$$

with $\omega_m(q) = \lambda \sin(\frac{q}{2})$ just from phase space effects (a small variation with temperature resulting from the dispersion has been neglected). Numerically the cut-off frequency of the central peak is found to remain localized at $\omega \approx \omega_m(q)$ for all wave vectors and temperatures (apart from corrections of $O(\lambda^2)$). The line shape, however, cannot be expected to be reproduced because only a few discrete transitions in the one-magnon band are available for $N = 16$ and dominate the spectrum at the lowest temperatures. Nevertheless, for $q = \pi$, $T = 0.5J$ the inverted line shape of eq. (2.13) starts to become visible even with this restriction. Between medium ($T = 0.5J$) and high ($T = 4J$) temperatures a crossover of the line shape from square like to Gaussian is observed for small wave vectors.

At zero temperature the central peak vanishes (*cf.* Fig. 2.7). At low temperatures, transitions within the one-magnon band set in first, in Fig. 2.10b clearly seen as peaks of the $T = 0.5$ solid curve. With increasing temperature, transitions within higher bands become more and more relevant, which can be seen in increasing background in Fig. 2.10b.

Fig. 2.11 shows the two-magnon peak at $q = \pi$ (where the bound states are most clearly visible) and $q = 2\pi$ for $\lambda = 0.3J$ and $N = 16$ in the temperature range $T = 0.5 \dots 2J$ (note the enhancement in intensity scaling compared to the central and one-magnon peak). For $q = \pi$ the low temperature spectra are entirely governed by the triplet bound state at $\omega \approx 1.938 \dots J$, whereas the continuum (whose intensity at $T = 0$ is smaller by a factor of λ^2) is of no significant role. The bound state stays clearly visible up to $T \approx J$ and then disappears in parallel with a rapid decrease in the integrated intensity of the two-magnon peak for temperatures above $T \approx J$ (see also Fig. 2.7). This reflects the fact that the dimers become independent of each other with increasing temperature such that the correlations between spins of two different dimers required for a finite two-magnon peak vanish.

Fig. 2.12 illustrates a comparison between the results for $N = 16$ and $N = 20$.¹ In going from $N = 16$ to $N = 20$, some improvement is obtained: the continuum becomes smoother and the bound state less dominant, but the main characteristics remain unchanged. Therefore, the increase in particle number is not crucial. The

1. Available only for $q = \pi$ and the limited frequency range $1.84J < \omega < 2.02J$.

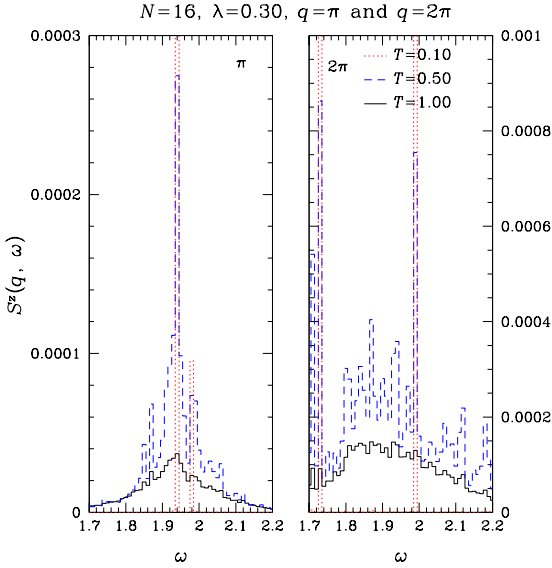


Figure 2.11: $S^{zz}(q, \omega)$ two-magnon peak. The resolution $\Delta\omega$ is 0.02.

spectra invoke the impression that at intermediate temperatures additional transitions — in particular the singlet state at $\omega \approx 1.868J$, which could be reached by a from a thermally excited triplet state — become visible. This, however, is misleading as the comparison between the data for $N = 16$ and $N = 20$ shows: a change in the number of spins leads to a different set of allowed wave vectors and therefore, from the accompanying change the initial and final energies, to trivially different excitation frequencies — although the energies at, *e. g.*, $q = \pi$ are remarkably independent of N). For $q = 2\pi$ there is no bound state; the two discrete transitions at $T \approx 0$ in Fig. 2.11b are the remainder of the continuum for the limited number of 16 spins.

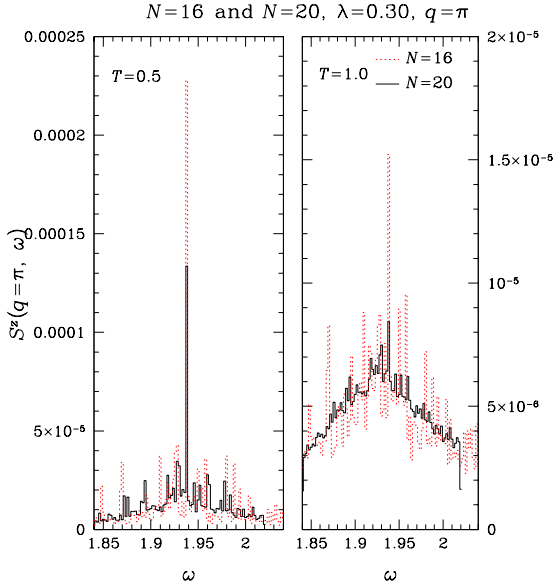


Figure 2.12: $S^{zz}(\pi, \omega)$ two-magnon peak, comparison of $N = 16$ and $N = 20$. The resolution $\Delta\omega$ is 0.02.

2.4 The dynamic structure factor in an external magnetic field

An external magnetic field breaks full rotational symmetry, and thus allows me to further investigate the properties of the bond alternating Heisenberg chain, as the dynamic structure factors $S^{xx}(q, \omega)$ and $S^{yy}(q, \omega)$ are not linearly dependent on the longitudinal structure factor $S^{zz}(q, \omega)$ any more. Typically, one is interested in the transverse dynamic structure factor

$$S^{xx}(q, \omega) + S^{yy}(q, \omega) = \frac{1}{2}(S^{+-} + S^{-+}) \quad (2.14)$$

at a given frequency ω . Given the form of the Hamilton operator in terms of S^\pm and S^z , it is reasonable to evaluate $S^{+-}(q, \omega)$ and $S^{-+}(q, \omega)$ instead of $S^{xx}(q, \omega)$ and

$S^{yy}(q, \omega)$. However, $S^{+-}(q, \omega)$ and $S^{-+}(q, \omega)$ are still related by detailed balance

$$S^{+-}(q, \omega) = e^{-\beta\omega} S^{-+}(-q, -\omega) \quad (2.15)$$

and thus it is only necessary to calculate $S^{+-}(q, \omega)$ and $S^{-+}(q, \omega)$ for positive frequencies $\omega > 0$.

In this work, I shall restrict my interest on the influence of static, homogeneous magnetic fields. An inhomogeneous field breaks translational symmetry, and a dynamic field adds time evolution, but both effects would go beyond the scope of this work.

In the presence of an external, static, homogeneous magnetic field, a field dependent term

$$\mathcal{H}_{\text{Zeeman}} = - \sum_i H S_i^z \quad (2.16a)$$

$$= -H S_{\text{tot}}^z \quad (2.16b)$$

is added to the Hamilton operator (2.1).

Whereas this additional term does not change the wave functions of the eigenstates (eq. (2.2)) with S^z as good quantum number, the energy levels are shifted simply by the Zeeman term according to their total spin projection S_{tot}^z , $-S_{\text{tot}} \leq S_{\text{tot}}^z \leq S_{\text{tot}}$, leading to several effects. Eventually, the relative decrease of energy levels with higher magnetization, *i. e.*, total spin projection S_{tot}^z leads to a level crossing of states with different magnetization S_{tot}^z .

It is particularly noteworthy that this effect also applies to the ground state, meaning on the other hand, that the ground state changes with the strength of the external magnetic field. The first change of the ground state for a gapped system like the bond alternating Heisenberg chain with $\lambda \neq 1$ occurs at finite field, namely the lower critical field

$$H_{\text{crit}} = E_{\text{min},1} - E_{\text{min},0}, \quad (2.17a)$$

where $E_{\text{min},n}$ denotes the minimal energy level in the subspace with total spin projection $S_{\text{tot}}^z = n$, minimizing over all wave vectors q . In standard models such as the bond alternating Heisenberg chain, subsequent changes occur (in total $N/2$) at

$$H_{\text{step},n} = E_{\text{min},n} - E_{\text{min},n-1}. \quad (2.17b)$$

Let me note that models exist where $\frac{1}{2}(E_{\text{min},n+1} - E_{\text{min},n-1}) < E_{\text{min},n} - E_{\text{min},n-1}$ resulting in magnetization steps of 2 units.[14] The last change — and thus saturation — is achieved when the ground state becomes fully polarized:

$$H_{\text{sat}} = E_{\text{min},N} - E_{\text{min},N-1}. \quad (2.17c)$$

Table 2.1: Critical fields for $\lambda = 0.3$ and $N = 12, 16,$ and 20 .

Magnetization	$N = 12$	$N = 16$	$N = 20$
1	0.81670	0.81685	0.81684
2	0.90250	0.86222	0.84431
3	1.04600	0.95459	0.90490
4	1.17713	1.06362	0.98724
5	1.26220	1.16169	1.07399
6	1.3	1.23446	1.15234
7		1.27964	1.21484
8		1.3	1.25956
9			1.28731
10			1.3

For the bond alternating Heisenberg chain, the ground state for zero field is found at $q = 0$. For the ground states with $E_{\min,1}$ and E_{sat} this can be shown easily as well. The first excited band is an $S = 1$ magnon with dispersion $\sim (1 - \cos(\frac{q}{2}))$, so the lowest lying state (the next ground state, energy $E_{\min,1}$) again is found at $q = 0$. Finally, by symmetry of its spin configuration, the saturation ground state (energy E_{sat}) is found at $q = 0$, too.

The total spin projection S_{tot}^z of the ground state reflects the magnetization $M(H)$. For a finite system size N , the range between the first critical field $H_{\text{crit},1}$ — which is obtained as a power series in λ from [3] — and the saturation field H_{sat} consists of discrete steps, whereas for an infinite chain, the change of the magnetization is continuous. Outside the interval from $H_{\text{crit},1}$ to H_{sat} , the magnetization is constant.

In this system, the first critical field $H_{\text{crit},1}$ is a quantum critical point, analogous to what has been discussed in other gapped one- or quasi one dimensional systems [the Haldane chain, the spin $\frac{1}{2}$ ladder and two-dimensional dimers] in an external magnetic field, where this is known as ‘Bose-Einstein-condensation of magnons’. In this sense, the bond alternating Heisenberg chain is very interesting, because it offers a simpler model for the complex behaviour of the aforementioned systems.

Of course, these formulae only hold true as long as the energy levels are finitely spaced such that the change in the ground state always fulfils $\Delta S_{\text{tot}}^z = 1$. This constraint is satisfied for the bond alternating Heisenberg chain as long as $\lambda \neq 0$ (and, of course $\lambda \neq 1$). For $\lambda = 0$, the chain breaks down to a set of non-interacting dimers, which all change from a singlet to a triplet ground state at the same field. In other words, all critical fields of eq. (2.17) coincide in one single point, where the magnetization jumps from zero to its maximal value.

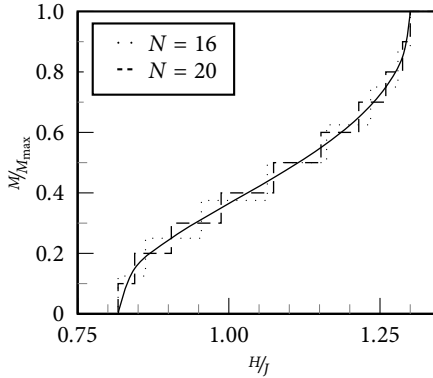


Figure 2.13: Magnetization curve of the bond alternating Heisenberg chain

For fields larger than the saturation field, the system behaves like a ferromagnet. Again, the energy spectrum is gapped, but this time the lowest excitation is a ferromagnon with

$$S_{\text{tot}}^z = NS - 1. \quad (2.18)$$

This ferromagnon has the spectrum

$$\omega(q) = H - J(1 + \lambda) \cos(q) \quad (2.19)$$

From the condition $\omega > 0$ we obtain the saturation field

$$H_{\text{sat}} = (1 + \lambda)J. \quad (2.20)$$

2.4.1 Specific Heat

The level spectrum in Fig. 2.14 features an interesting gap in the area between $H = J$ and H_{sat} and $E - E_0 < J$. This gap is an image of the gaps of the energy bands and occurs repeatedly with $\Delta E = J$. This is easy to understand, if one considers the non-interacting dimer limit, where at $H = 0$ the energy bands are highly degenerate with energy values $\frac{E}{J} = -\frac{3}{4}\frac{N}{2} + n$, $n = 0, \dots, \frac{N}{2}$. For higher values of H , they Zeeman

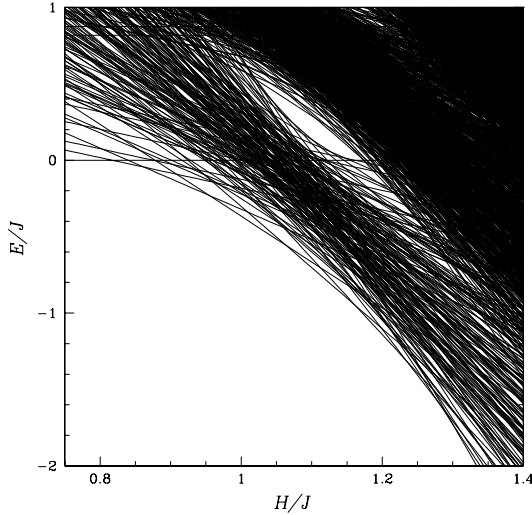


Figure 2.14: Dependence of the energy spectrum on the magnetic field in the vicinity of critical and saturation field for $N = 16$ and $\lambda = 0.3$.

split, but at $H = 1$, they cross at $\frac{E}{J} = -\frac{3}{4}\frac{N}{2} + n$, $n = 0, \dots, N$, and it is of no surprise that there are gaps in between. For $\lambda > 0$, the bands broaden, and the gaps get smaller but still remain clearly visible for $\lambda = 0.3$.

For the specific heat, only the lowest gap, depicted in Fig. 2.14 is of major interest, as it divides the low lying thermal excitations into two different regimes: low energetic excitations within the lower band, and high energetic excitations of the order of J , separated by the gap in the spectrum. This feature leads me to expect a double maximum of the specific heat.

The thermodynamic expressions determining the specific heat are (with $k_B \equiv 1$)

$$F = -\frac{1}{\beta} \ln(Z), \quad S = \beta^2 \frac{\partial F}{\partial \beta} \quad (2.21a)$$

$$C = -\beta \frac{\partial S}{\partial \beta} = \beta^2 \frac{\partial^2 \ln(Z)}{\partial \beta^2} \quad (2.21b)$$

Using this formula and the partition function of a set of $N/2$ non-interacting dimers (2.9), the specific heat of a set of non-interacting dimer turns out as

$$C = \frac{N}{2} \frac{\beta^2 e^{-\beta J}}{[1 + e^{-\beta(J-H)} + e^{-\beta(J+H)} + e^{-\beta J}]^2} \left[J^2 + 2(J^2 + H^2) \cosh(\beta H) + 2H^2 e^{-\beta J} (2 + \cosh(\beta H)) - 4JH(\sinh(\beta H)) \right] \quad (2.22)$$

which can be used for comparison.

Fig. 2.15 shows the specific heat of a $N = 20$ bond alternating Heisenberg chain at $\lambda = 0.3$ and three different magnetic fields. Figs. 2.16 to 2.19 present the specific heat at different values of the parameter λ , grouped by magnetic field. For comparison, the analytically calculated specific heat of a set of non-interacting dimers is drawn as lines in all of these plots.

These figures show two temperature scales, one at $T \approx 0.5J$ and the other one order of magnitude smaller. The second, low temperature peak is clearly visible at $H \approx J$ (only as shoulder for the largest λ value $\lambda = 0.5$) but vanishes for $T \ll H_{\text{crit}}$ and $T \gg H_{\text{sat}}$.

With increasing λ the double peak vanishes and becomes a broadened single peak, which can be explained by the dissolution of the band structure.

At very low temperatures, the specific heat is rather proportional to the temperature, which can be seen in *cf.* Fig. 2.20. The deviations, especially at $T \rightarrow 0$ are only caused by the discreteness of the finite system. This linearly increasing specific heat showing gapless excitations suggests that this one-dimensional system is a LUTTINGER liquid [15]. Other investigations confirm that the bond alternating Heisenberg chain indeed is a LUTTINGER liquid [16, 17, 18].

2.4.2 Qualitative Properties of the Dynamic Structure Factor

Before presenting and discussing the quantitative results of my calculations, I will give an overview of the qualitative properties of the dynamic structure factor in an

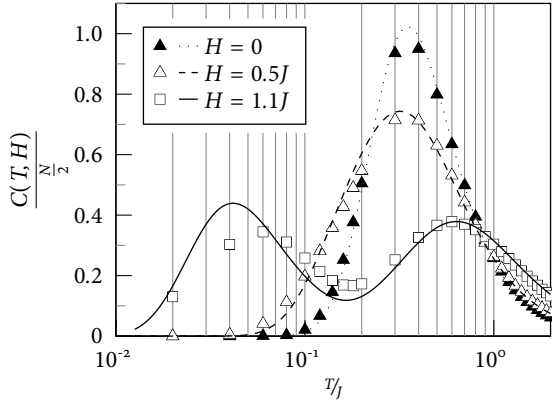


Figure 2.15: Specific heat of non-interacting dimers (lines) and for $N = 20$, $\lambda = 0.3J$ (data points) vs. T .

external field. This purely qualitative discussion is mainly based on the analytical results of the non-interacting dimers in Section 2.2 and the field dependent energy spectrum of a single dimer depicted in Fig. 2.21.

As already mentioned in the introduction of this section, the external magnetic field breaks the rotational symmetry, thus splitting the longitudinal structure factor $S^{zz}(q, \omega)$ and the transverse structure factors $S^{+-}(q, \omega)$ and $S^{-+}(q, \omega)$ into independent quantities.

From the experimental point of view, the first step is to observe the sum of both — longitudinal and transverse — structure factors. However, each of them is a separate contribution with its own characteristic and needs to be discussed separately. At a later stage, they will be distinguishable in experiments, too, *e. g.*, using polarized neutrons.

In the introduction I already pointed out that computational resources impose restrictions on the system size. In this specific context this means that $N = 12$ can be done for all choices of parameters and for a large number of parameters. $N = 16$

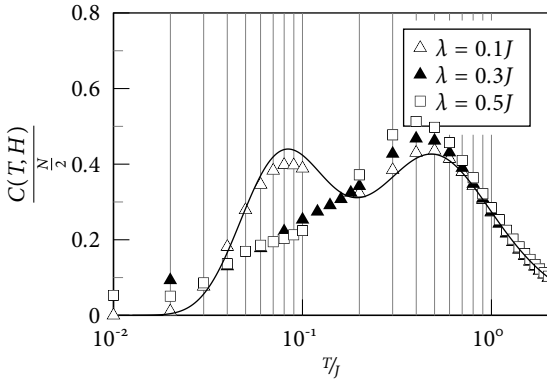


Figure 2.16: Specific heat vs. T for $N = 20$, $H = 0.8J$ and $\lambda = 0.1, 0.3$, and 0.5 .

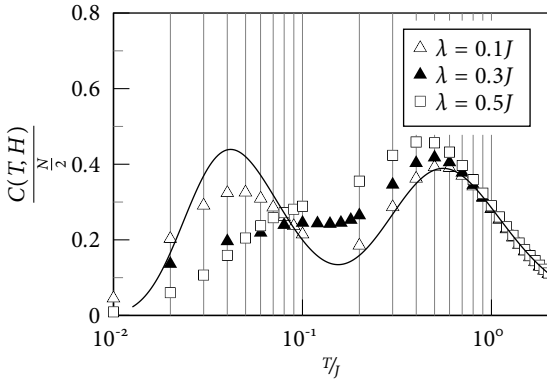


Figure 2.17: Specific heat vs. T for $N = 20$, $H = 0.9J$ and $\lambda = 0.1, 0.3$, and 0.5 .

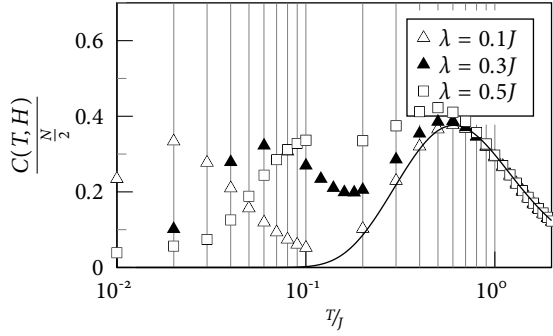


Figure 2.18: Specific heat vs. T for $N = 20$, $H = 1.0J$ and $\lambda = 0.1, 0.3$, and 0.5 .

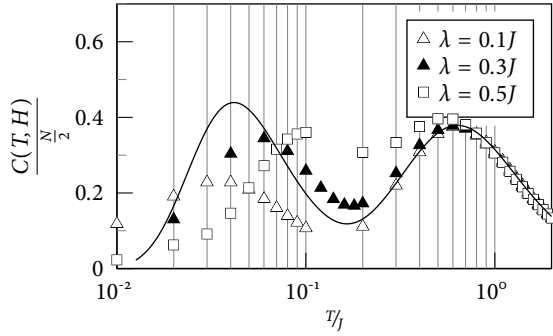


Figure 2.19: Specific heat vs. T for $N = 20$, $H = 1.1J$ and $\lambda = 0.1, 0.3$, and 0.5 .

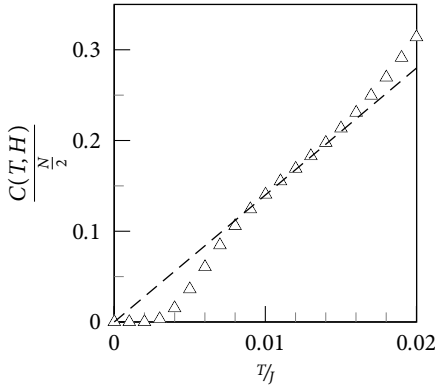


Figure 2.20: Specific heat vs. T in the low temperature regime for $\lambda = 0.3$, $N = 20$, and $H = 1.1J$.

can be done for the longitudinal structure factor for all choices of parameters, but only for low temperatures ($T \lesssim 0.1$) for the transverse structure factor. Finally, for large temperatures $N = 20$ can only be done for the longitudinal structure factor, whereas the transverse structure factor is limited to low temperatures ($T \lesssim 0.1J$) and a limited frequency range.

The next parameter to be discussed is the wave vector of a transition, *i. e.*, the difference of the wave vectors of the initial and final states. Due to the dimerized structure of the alternating Heisenberg chain the periodicity of the wave vector is 4π instead of 2π , which means that structure factors for $q = 0$ and $q = 2\pi$ are different. This is largely due to the ‘dimer structure factor’ which maps the geometrical structure of the array. This factor, however, varies with the excitation energy: the standard expression $1 - \cos(qd)$ is true only for the one-magnon excitation, whereas $1 + \cos(qd)$ holds for the central excitation, which can also be seen in the analytic solution of the non-interacting dimers in Section 2.2. Therefore, $q = 0$ emphasizes the central and suppresses the one-magnon peak, and $q = 2\pi$ suppresses the cen-

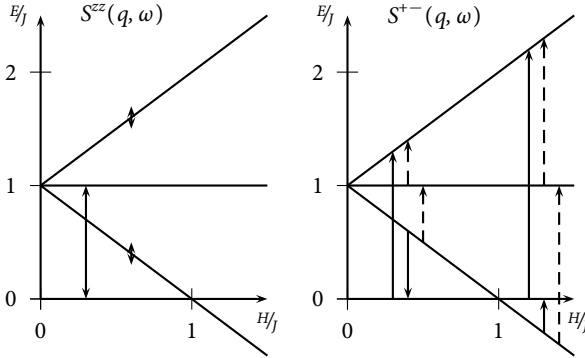


Figure 2.21: Magnetic field dependence of single dimer transitions contributing to (a) $S^{zz}(q, \omega)$ and (b) $S^{+-}(q, \omega)$. Solid lines denote dipole transitions between singlet and triplet states (called one-magnon peak in this work), dashed lines denote weak intra-band transitions within the triplet (central peak). S^{zz} is dominated by contributions in the frequency range $\omega \approx J$, S^{+-} in the frequency range $\omega \approx J \pm H$.

tral peak and emphasizes the one-magnon excitations. The intermediate case $q = \pi$ shows both contributions.

The central peak results for vanishing magnetic field from transitions connecting excited states of a dimer. For $H \neq 0$ it is therefore found at $\omega \approx 0$ for S^{zz} and at $\omega = +H$ for S^{+-} ($\omega = -H$ for S^{-+}). The one (two) quantum transition at zero field results from exciting one (two) dimers, correspondingly, the one (two) quantum transitions relate to $\omega \approx J$ ($\omega \approx 2J$) or $\omega \approx J \pm H$ ($\omega \approx 2J \pm H$) respectively. For the longitudinal structure factor, this gives the simple relations between $\omega \approx 0$ and the central peak, $\omega \approx J$ and the one-magnon peak, as well as $\omega \approx 2J$ and the two-magnon peak.

The transverse structure factor on the other hand has transitions with $\Delta S_{\text{tot}}^z = \pm 1$ and thus experiences a magnetic field dependence of the frequency originating from the Zeeman split. Albeit this frequency dependence is continuous, one can say as a rule of thumb that for small fields, $\omega \approx 0$ is related to the central peak, $\omega \approx J$ to the one-magnon, and $\omega \approx 2J$ to the two-magnon peak. Between the critical and saturation field, S^{+-} and S^{-+} must be accounted differently. For S^{+-} , $\omega \approx J$ is related to the central peak, $\omega \approx 2J$ to the one-magnon, and $\omega \approx 3J$ to

the two-magnon peak. For S^{--} on the other hand, $\omega \approx -J$ is related to the central peak, $\omega \approx 0$ to the one-magnon, and $\omega \approx J$ to the two-magnon peak.

Although this frequency shift might propose to plot the transverse structure factors vs. $\omega \mp H$ in order to follow the transition strength for any given level, this misses one important point which can only be guessed with difficulty from these plots: Increasing field changes the Boltzmann factors of the states, and new states arise while previous ones become suppressed, resulting in an essentially unchanged excitation energy. Therefore it makes more sense to look at the structure factor vs. ω behaviour.

The transverse structure factor is the relevant quantity for the intensity of low energetic transitions in the ground state band, whereas the longitudinal structure factor is the important quantity for one quantum excitations, *cf.* Section 2.4.3.

I will discuss the temperature dependence of the dynamic structure factor in detail in Section 2.4.3 for zero temperature and Section 2.4.4 for finite temperature. With the aim to discuss how temperature broadens the quantum singularities or, the other way round, how low temperatures make the quantum broadening visible.

Now I again discuss the decoupled dimer limit. Particularly, a new, long range order term is added to the central peak contribution of the longitudinal structure factor:

$$S_{\lambda=0}^{zz}(q, \omega) = B_0^{zz}(q, \beta, H)\delta(\omega) + B_1^{zz}(q, \beta, H)[\delta(\omega - J) + e^{-\beta J}\delta(\omega + J)] \quad (2.23a)$$

$$S_{\lambda=0}^{+-}(q, \omega) = 2 \left[B_0^{+-}(q, \beta, H)\delta(\omega - H) + B_1^{+-}(q, \beta, H)[\delta(\omega - H - J) + e^{-\beta(J-H)}\delta(\omega - H + J)] \right] \quad (2.23b)$$

$$S_{\lambda=0}^{-+}(q, \omega) = S_{\lambda=0}^{+-}(-q, -\omega) \quad (2.23c)$$

with

$$B_0^{zz}(q, \beta, H) = \frac{1 + \cos(qd)}{2} \left[\frac{\cosh(\beta H)}{1 + e^{\beta J} + 2 \cosh(\beta H)} + \frac{(\frac{N}{2}\delta_{q,0} - 1)(\cosh(2\beta H) - 1)}{(1 + e^{\beta J} + 2 \cosh(\beta H))^2} \right] \quad (2.24a)$$

$$B_1^{zz}(q, \beta, H) = \frac{1 - \cos(qd)}{4} \frac{e^{\beta J}}{1 + e^{\beta J} + 2 \cosh(\beta H)} \quad (2.24b)$$

$$B_0^{+-}(q, \beta, H) = \frac{1 + \cos(qd)}{4} \frac{1 + e^{\beta H}}{1 + e^{\beta J} + 2 \cosh(\beta H)} \quad (2.24c)$$

$$B_1^{+-}(q, \beta, H) = \frac{1 - \cos(qd)}{4} \frac{e^{\beta J}}{1 + e^{\beta J} + 2 \cosh(\beta H)} \quad (2.24d)$$

$$(2.24e)$$

and the limits

$$B_0^{zz}(q, T = 0, H) = B_0^{+-}(q, T = 0, H) = \frac{1 + \cos(qd)}{2} \begin{cases} 0, H < J \\ \frac{1}{2}, H = J \\ 1, H > J \end{cases} \quad (2.25a)$$

$$B_1^{zz}(q, T = 0, H) = B_1^{+-}(q, T = 0, H) = \frac{1 - \cos(qd)}{4} \begin{cases} 1, H < J \\ \frac{1}{2}, H = J \\ 0, H > J \end{cases} \quad (2.25b)$$

$$B_0^{zz}(q, T \rightarrow \infty, H) = B_0^{+-}(q, T \rightarrow \infty, H) = \frac{1 + \cos(qd)}{8} \quad (2.25c)$$

$$B_1^{zz}(q, T \rightarrow \infty, H) = B_1^{+-}(q, T \rightarrow \infty, H) = \frac{1 - \cos(qd)}{16} \quad (2.25d)$$

$$B_0^{zz}(q, \beta, H \rightarrow \infty) = B_0^{+-}(q, \beta, H \rightarrow \infty) = \frac{N}{4} \delta_{q,0} \quad (2.25e)$$

$$B_1^{zz}(q, \beta, H \rightarrow \infty) = B_1^{+-}(q, \beta, H \rightarrow \infty) = 0 \quad (2.25f)$$

The magnetic field dependence of the structure factors of the non-interacting dimers for temperatures $T = 0.1J, 0.5J,$ and $2J$ (solid lines), along with the numerically computed exclusive structure factors of the bond alternating Heisenberg chain for $\lambda = 0.3$ (data points) is presented in Figs. 2.22 (also $T = 0.02J$) and 2.23. For higher temperatures ($T \gtrsim 0.5J$), the analytic solution for the dimers/non-interacting non-interacting dimers conforms to the actual data for $\lambda = 0.3$ quite well, reinforcing the validity of the expansion of the above discussion to the bond alternating Heisenberg chain. For lower temperatures however, the thermal smearing decreases and the quantum effects of the finitely coupled spins become visible as the difference between the analytic and the numeric solution in Fig. 2.22 (a). In the limit $T = 0$ and $\lambda = 0$, both thermal and quantum smearing vanish, and the shape of the structure factor is a perfect step.

2.4.3 The Dynamic Structure Factor at Zero Temperature

Following the qualitative presentation of the previous section, I will now discuss the properties of the dynamic structure factor at zero temperature. In this limit thermal effects vanish leaving room for quantum effects.

At zero temperature thermal excitations simply do not exist, which means on the other hand that all transitions contributing to the dynamic structure factor must involve the ground state, which in this model has got momentum $q = 0$. From the discussion in the previous section, it is known that transitions in the ground state band are visible in the transverse structure factor and lie in the central peak, and that the central peak is most prominent when $\Delta q = 0$. Hence, the regime of major interest involves $q = 0$ and $\Delta q = 0$. Furthermore, the absence of thermally excited states restricts the transition frequency to positive values $\omega > 0$.

As long as the magnetic field stays below the critical field, no qualitative change in the structure factors can be observed. For S^{+-} and S^{-+} the structure factors are shifted in energy by $+H$ resp. $-H$ (corresponding to the Zeeman levels), but they keep their shape, because the states involved remain the same.

At the critical magnetic field H_{crit} a drastic change of the dynamic structure factors sets in, which is caused by a change of the ground state from a singlet ($|0, 0\rangle$) to the $S^z = 1$ branch of a triplet ($|1, +1\rangle$). With increasing magnetic field the ground state changes through all magnetizations $|S, +S\rangle$ until saturation is reached where $|S_{\text{max}}, +S_{\text{max}}\rangle$ for $H \geq H_{\text{sat}}$.

Since the magnetization is conserved under the investigated Hamilton operator, only transitions of the form $|S, +S\rangle \rightarrow |S', +S\rangle$ with $S' \geq S$ contribute to S^{zz} . The dominant contribution however comes from the transitions with the lowest $S' = S + 1$ state, *i. e.*, the state whose sibling state with $S^z = S + 1$ is bound to be the next ground state as the magnetic field increases.

The frequency of this dominant transition depends on the magnetic field. For small values of the magnetic field $H < H_{\text{crit}}$ it is frozen, but above the critical field it increases with $\omega \approx J + H$ (or moreover in steps of the magnetic field corresponding to the different magnetization values) until it reaches saturation, where it remains constant again. For an infinite system, the curve $\omega(H)$ is indeed smooth because $M(H)$ is smooth, but in the finite systems investigated here it features clearly visible steps originating from the discrete steps of the magnetization.

The dominant transition however is not the only one contributing to the dynamic structure factor. Additional strength is gained from one-magnon transitions with $\omega \approx J$ whose number depends on the number of states in the S' band. Further small corrections are supplied from two-magnon transitions ($\omega \approx 2J$).

The discussion for S^{+-} (S^{-+}) follows the same scheme. Conservation of magnetization restricts the transitions to $|S, +S\rangle \rightarrow |S', S - 1\rangle$ with $S' \geq S - 1$ ($|S, +S\rangle \rightarrow$

$|S', S + 1\rangle$ with $S' \geq S + 1$). The dominant contribution comes from the transition to the lowest state with $S' = S'_{\min}$, *i. e.*, $S' = S - 1$ ($S' = S + 1$), which is the state set to be the next ground state with decreasing (increasing) field.

In order to determine the characteristics of the dynamic structure factor in the zero temperature limit I have used the following procedure. First, I numerically calculate the transition strengths for the very low temperature $T = 0.01J$ — which is possible even for $N = 20$ — ignoring contributions less than 10^{-8} . From these results, I extract all transitions involving the respective ground state with $\omega \geq 0$. The calculated values still need correction for the deviation of the partition function from 1 at the finite temperature $T = 0.01J$. This results in a relatively short list of transitions with the following characteristics (for a given wave vector transfer and magnetic field):

Typically, one strong transition attracts attention, which also marks the threshold energy, and is accompanied by many transitions with notably smaller intensities at higher energies. Qualitatively, this corresponds to the picture developed in the field theoretic approach resulting in an infra-red divergence [19], *i. e.*,

$$S(q, \omega) = \frac{1}{(\omega - \omega_0)^\alpha} \quad (2.26)$$

with a characteristic exponent α , which of course depends on the underlying system, *i. e.*, the value of λ . The principal aim of this type of analysis is the verification of this result and, if possible, the determination of this exponent α . Unfortunately, the uncertainty in the frequency ω_0 and, for the transverse part, the variation of ω with the magnetic field render the usual log/log plot useless, so in order to avoid specification of ω_0 but include large and small scattering strengths at the same time, Fig. 2.28 shows $\ln S$ vs. ω for $N = 20$ spins and $H = 0.94J$. The decrease with frequency as well as the scattering of the data are clearly visible, but a determination of the exponent α does not appear possible.

However, two aspects of the zero temperature data, which only involve the dominant transition, lead to an interesting analysis.

1. The dependence of the strength of the dominant peak on the magnetization is shown in Figs. 2.24 and 2.25.
2. The variation of the strength of the dominant transition with the number of sites, corresponding to the analysis for the Haldane chain in [19]. The motivation of this analysis is the idea that the particle number dependence on the lowest, *i. e.*, dominant frequency

$$\omega \propto \frac{1}{N} \quad (2.27)$$

translates into a particle number variation of the leading peak

$$S(q, \omega) \propto N^{\alpha-1} \quad (2.28)$$

cf. eq. (2.26). Following this procedure I have analysed the $T = 0$ data by plotting $\ln(S)$ vs. $\ln(N)$. The results are presented in Fig. 2.26 for S^{zz} with $\alpha \approx 0.6$ and in Fig. 2.27 for S^{+-} with $\alpha \approx 1.33$ and clearly show manifestations of the proposed infra-red singularity despite the low values of the particle number N .

2.4.4 The dynamic structure factor at finite temperature

The various important aspects of the temperature, magnetic field, and wave vector dependence of both longitudinal and structure factor!transversetransverse dynamical structure factors are shown in Figs. 2.29 to 2.61. In order to better compare the diagrams, all of them have been made with $\lambda = 0.3$.

For the longitudinal structure factor, Figs. 2.29 and 2.30 present a temperature scan at fixed magnetization $M = \frac{1}{2}M_{\text{sat}} - 1 = N/4 - 1$ for both wave vectors $q = \pi$ and 2π . Figs. 2.31 and 2.32 compare the particle numbers $N = 20$ and $N = 16$ in a magnetic field scan at $T = 0.01J$ for $q = \pi$, and Figs. 2.36 and 2.37 do likewise for $q = 2\pi$. Figs. 2.33 to 2.35 show magnetic field scans at three different temperatures for $q = \pi$, and Figs. 2.38 to 2.40 for $q = 2\pi$. Finally, Figs. 2.41 to 2.44 depict the two-magnon peak at different temperatures and magnetic fields.

The relevant variable is actually not the magnetic field H , but the magnetization M . In a discrete system, however, there is no one-to-one correspondence between magnetic field and magnetization. Rather the magnetization changes in discrete steps, on which the magnetic field can be varied without changing the magnetization. This however changes the Boltzmann factors which enter $S(q, \omega)$ and, due to Zeeman splitting, the frequency ω of $S^{+-}(q, \omega)$ and $S^{-+}(q, \omega)$. Therefore, I state the magnetic field at which I performed the calculations.

For the transverse structure factor, Figs. 2.45 and 2.46 present a temperature scan at fixed magnetization $M = N/4 - 1$ for both wave vectors $q = \pi$ and 2π . Figs. 2.47 and 2.48 compare the particle numbers $N = 20$ and $N = 16$ in a magnetic field scan at $T = 0.01J$ for $q = \pi$, and Figs. 2.53 and 2.54 do likewise for $q = 2\pi$. Similarly, Figs. 2.50 and 2.51 as well as Figs. 2.56 and 2.57 compare $N = 16$ and $N = 12$ at $T = 0.10J$ and demonstrate that at $T \geq 0.10J$, it is sufficient to take $N = 12$ into account. Figs. 2.49 to 2.52 show magnetic field scans at three different temperatures for $q = \pi$, and Figs. 2.55 to 2.58 for $q = 2\pi$. Finally, Figs. 2.59 to 2.61 depict the two-magnon peak at different temperatures and magnetic fields.

$\omega = 0$ contributions can only be found in the longitudinal structure factor S^{zz} , but not in the transverse structure factor S^{+-} .

Larger particle numbers like $N = 20$ exhibit a richer spectrum, but all essential features are present and clear for $N = 16$ or even $N = 12$. The latter is necessary for the transverse structure factor at higher temperatures $T > 0.1J$.

$T = 0.03J$ still shows quantum effects, but at higher temperatures quantum effects cannot be identified any more.

The longitudinal structure factor

Being diagonal, the longitudinal dynamic structure factor $S^{zz}(q, \omega)$ only depends on transitions within the subspace of constant magnetization S_{tot}^z . For each of these transitions, the momentum and energy transfer (q, ω) are independent of the applied magnetic field, but the magnitude of the transition strength changes in an external magnetic field due to the dependence of the Boltzmann factor

$$\frac{1}{Z} \exp\left(-\beta(E(H, S_{\text{tot}}^z) - E_0(H))\right) \quad (2.29)$$

on the magnetic field H and the total spin projection S_{tot}^z .

Figs. 2.29 ($q = \pi$) and 2.30 ($q = 2\pi$) show temperature scans of the longitudinal structure factor $S^{zz}(q, \omega)$ of a $N = 16$ bond alternating Heisenberg chain at magnetization $M = N/4 - 1$. For the very low temperature $T = 0.01J$, it was also possible to calculate the structure factors for $N = 20$, which are also displayed. The longitudinal structure factor has a strong one-magnon peak, which can be observed at all temperatures and all momenta. One-magnon peak means transition between $S_{\text{tot}}^z = 0$ states of the singlet and triplet of one dimer where the other dimers are thermally excited according to the temperature T and a number of dimers corresponding to the magnetization excited to the triplet state. For $q \neq 2\pi$ there is also a central peak close to $\omega = 0$ (the exact value depends on the dispersion), which gains intensity with increasing temperature.

The quantum features of this system can be easily identified only for temperatures $T \lesssim 0.03J$, whereas for $T \gtrsim 0.07J$ thermal excitations cover the underlying quantum structure. For $T \gtrsim J$, single discrete excitations have vanished in favour of a smooth curve.

Figs. 2.31 ($N = 20, q = \pi$) and 2.32 ($N = 16, q = \pi$) as well as 2.36 ($N = 20, q = 2\pi$) and 2.37 ($N = 16, q = 2\pi$) compare the longitudinal structure factors $S^{zz}(q, \omega)$ of a bond alternating chain of $N = 20$ and $N = 16$ spins at temperature $T = 0.01J$ and various magnetizations. While the different system sizes cause a change in the details of the structure factors, the overall line shape as well as all important features do not depend on the system size.

Figs. 2.33 ($T = 0.03J$), 2.34 ($T = 0.10J$), and 2.35 ($T = 1.00J$) show magnetization (magnetic field) scans of the longitudinal structure factor $S^{zz}(q = \pi, \omega)$ of a $N = 16$ bond alternating chain. Below $T \leq 0.10J$, non-zero magnetization causes the central peak to appear, which can be understood with the help of the discussion of the non-interacting dimers (Section 2.4.2). At zero magnetization and low temperatures, all transitions must involve the singlet ground state, but any one of these transitions has got a frequency $\omega \gtrsim J$. At higher magnetizations, on the other hand, the ground state is the lowest state of a band of triplets, quintets, *etc.*, hence low frequency transitions within these multiplets are possible.

Apart from this, the intensity of the central peak is rather insensitive to changes of the magnetization, while the one-magnon peak loses intensity with increasing magnetization. The temperature $T = 1.00J$ is already so large that thermal excitations cover all underlying level changes, resulting in a rather constant (with respect to magnetization) dynamic structure factor.

Analogously, Figs. 2.38 ($T = 0.03J$), 2.39 ($T = 0.10J$), and 2.40 ($T = 1.00J$) show magnetization (magnetic field) scans of the longitudinal structure factor $S^{zz}(q = 2\pi, \omega)$ of a $N = 16$ bond alternating chain. As already seen in the temperature scans (Fig. 2.30), the longitudinal structure factor at $q = 2\pi$ does not exhibit a central peak. At $T = 0.03J$ and $T = 0.10J$, the one-magnon peak changes its shape with changing magnetization, from a peak maximum at the low energetic end at low magnetizations to a peak maximum at the high energetic end at high magnetizations.

As in the $q = \pi$ case, the temperature $T = 1.00J$ is already so large that thermal excitation cover all underlying level changes, resulting in a more or less constant (with respect to magnetization) dynamic structure factor with a maximum peak at the low energetic end, although this peak is slightly emphasized at low magnetizations.

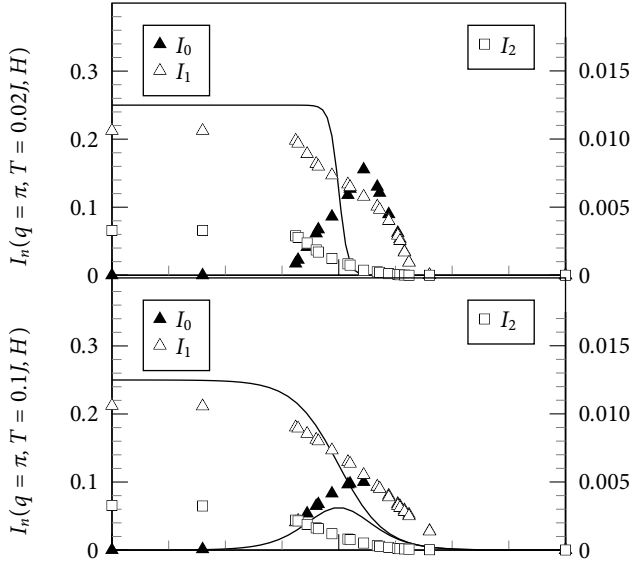


Figure 2.22: Exclusive structure factors $I^{zz}(q, H, \pi, \omega)$ vs. H for $N = 12$, $\lambda = 0.3$, and temperatures $T = 0.02$, $T = 0.1$, $T = 0.5$, and $T = 2$. The solid lines correspond to the analytic solution for $\lambda = 0$. (continued)

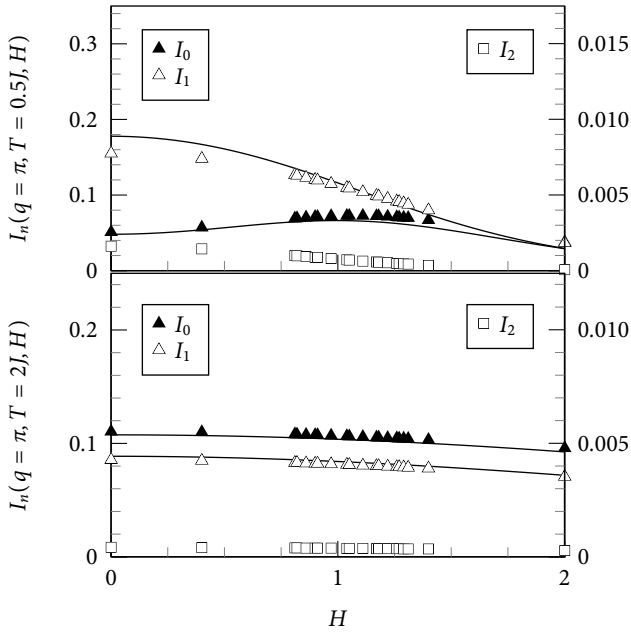


Figure 2.22: (continued) Exclusive structure factors $I^{zz}(q = \pi, \omega)$ vs. H for $N = 12$, $\lambda = 0.3$, and temperatures $T = 0.02$, $T = 0.1$, $T = 0.5$, and $T = 2$. The solid lines correspond to the analytic solution for $\lambda = 0$.

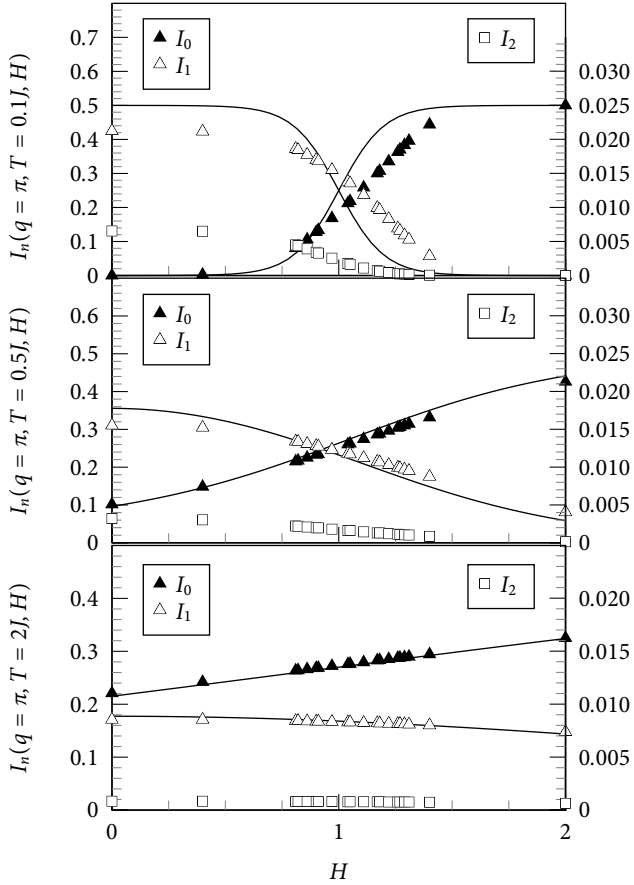


Figure 2.23: Exclusive structure factors $I^{+-}(q = \pi, \omega)$ vs. H for $N = 12$, $\lambda = 0.3$, and temperatures $T = 0.1$, $T = 0.5$, and $T = 2$. The solid lines correspond to the analytic solution for $\lambda = 0$.

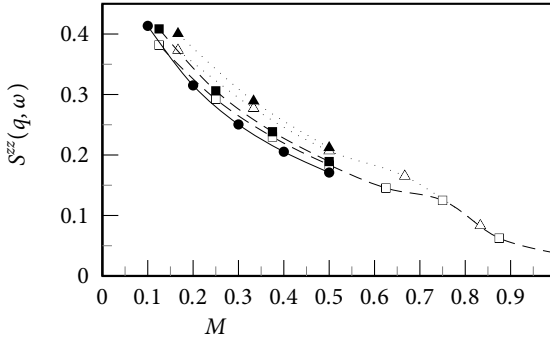


Figure 2.24: $S^{zz}(q, \omega)$ vs. M . Open symbols denote $\lambda = 0.05$, filled symbols $\lambda = 0.30$. Triangles (▲) represent $N = 12$, squares (■) $N = 16$, and circles (●) $N = 20$.

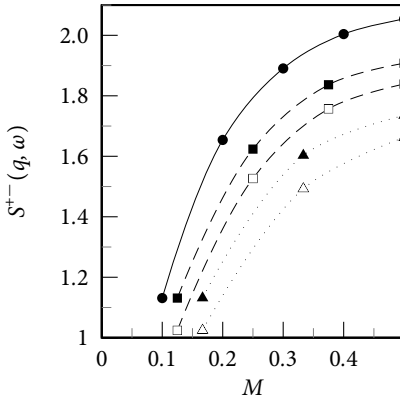


Figure 2.25: $S^{+-}(q, \omega)$ vs. M . Open symbols denote $\lambda = 0.05$, filled symbols $\lambda = 0.30$. Triangles (▲) represent $N = 12$, squares (■) $N = 16$, and circles (●) $N = 20$.

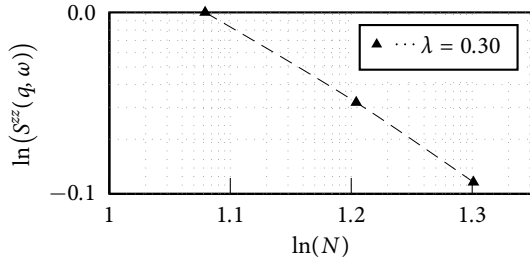


Figure 2.26: $\ln(S^{zz}(q, \omega))$ vs. $\ln(N)$

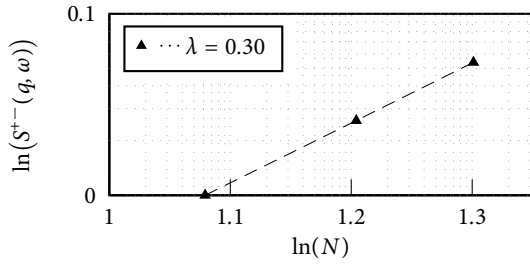


Figure 2.27: $\ln(S^{+-}(q, \omega))$ vs. $\ln(N)$

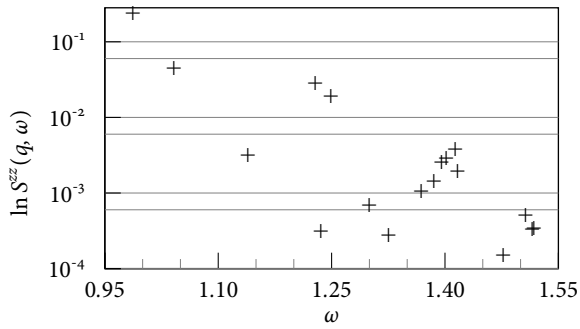


Figure 2.28: All one-magnon contributions to $\ln S^{zz}(q, \omega)$ vs. ω for $N = 20$ at $H = 0.94J$.

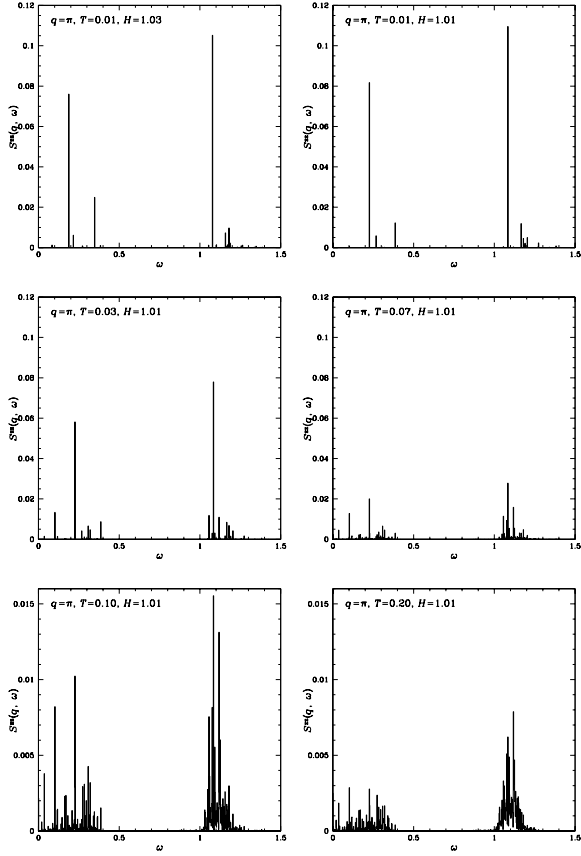


Figure 2.29: Longitudinal dynamic structure factor $S^{zz}(q = \pi, \omega)$ at $M = N/4 - 1$ for $N = 20$, $H = 1.03$, $T = 0.01$ and $N = 16$, $H = 1.01$, and $T = 0.01, 0.03, 0.07, 0.10, 0.20$, and $0.30J$ as well as ... (continued)

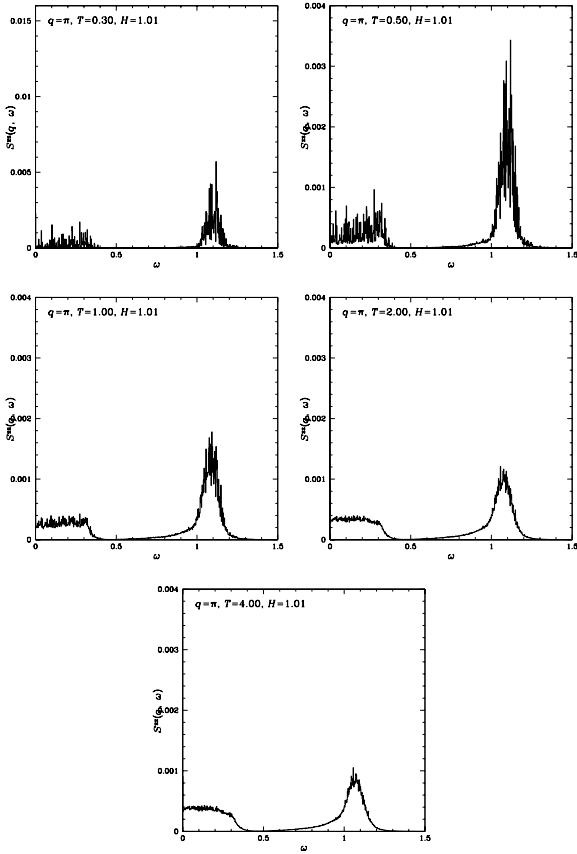


Figure 2.29: (continued) ... $T = 0.50, 1.00, 2.00,$ and $4.00J$. The resolution $\Delta\omega$ is 0.002 .

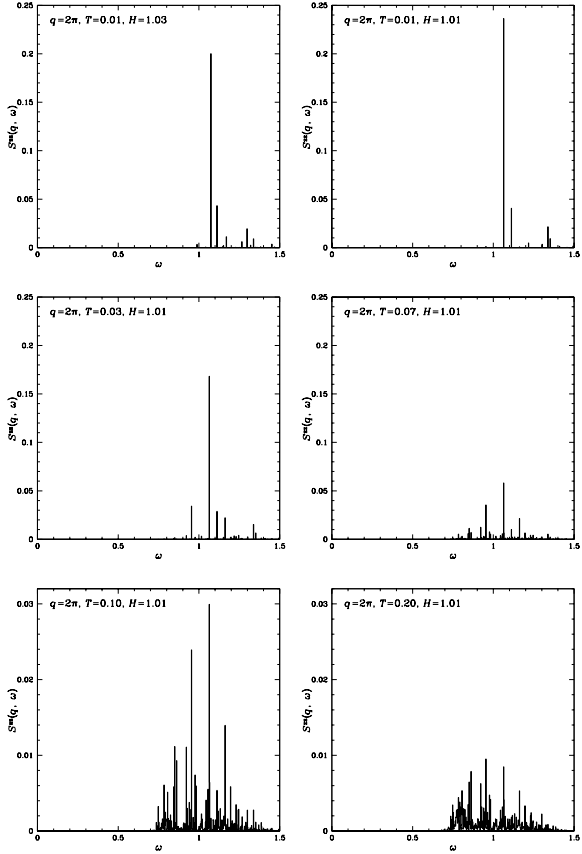


Figure 2.30: Longitudinal dynamic structure factor $S^{zz}(q = 2\pi, \omega)$ at $M = N/4 - 1$ for $N = 20$, $H = 1.03J$, $T = 0.01$ and $N = 16$, $H = 1.01J$, and $T = 0.01, 0.03, 0.07, 0.10, 0.20$, and $0.30J$ as well as ... (continued)

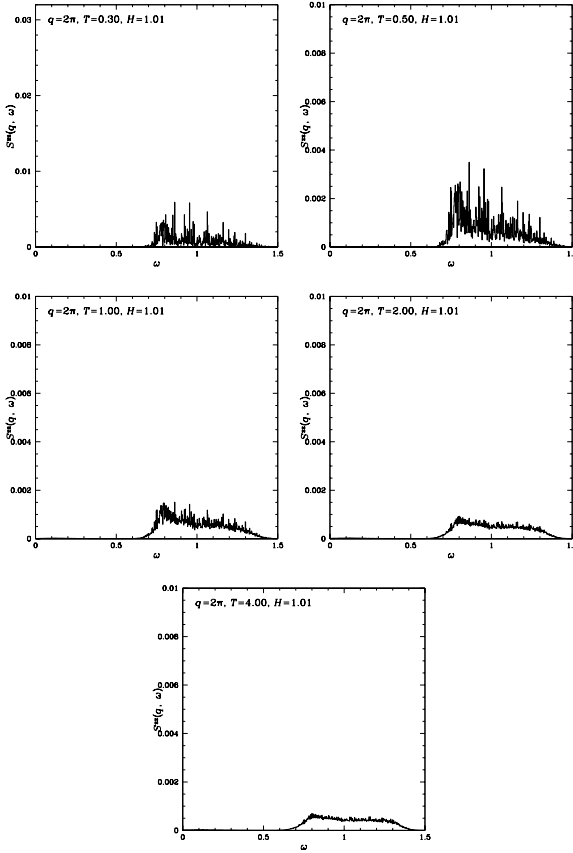


Figure 2.30: (continued) ... $T = 0.50, 1.00, 2.00,$ and $4.00J$. The resolution $\Delta\omega$ is 0.002.

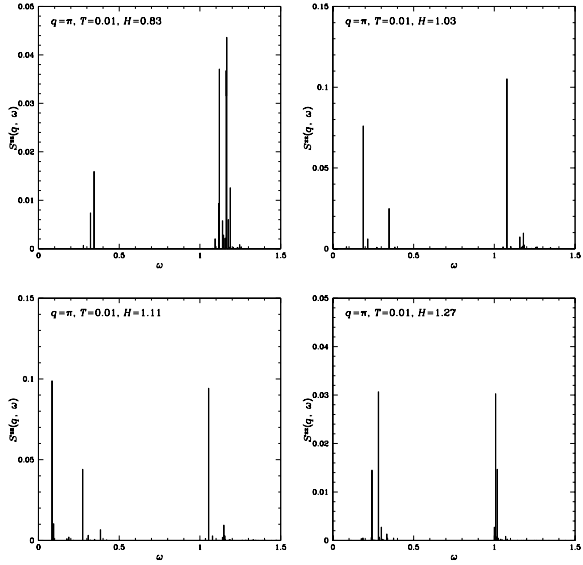


Figure 2.31: Longitudinal dynamic structure factor $S^{zz}(q = \pi, \omega)$ for $N = 20$, $T = 0.01J$, and $H = 0.83, 1.03, 1.11$, and $1.27J$. The first critical field is at $H \approx 0.81684J$, the saturation field at $H = 1.3J$. The resolution $\Delta\omega$ is 0.002 .

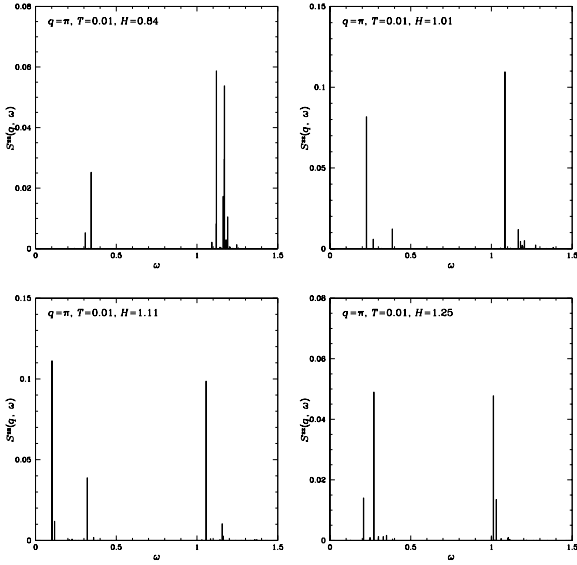


Figure 2.32: Longitudinal dynamic structure factor $S^{zz}(q = \pi, \omega)$ for $N = 16$, $T = 0.01J$, and $H = 0.84, 1.01, 1.11$, and $1.25J$. The first critical field is at $H \approx 0.81685J$, the saturation field at $H = 1.3J$. The resolution $\Delta\omega$ is 0.002.

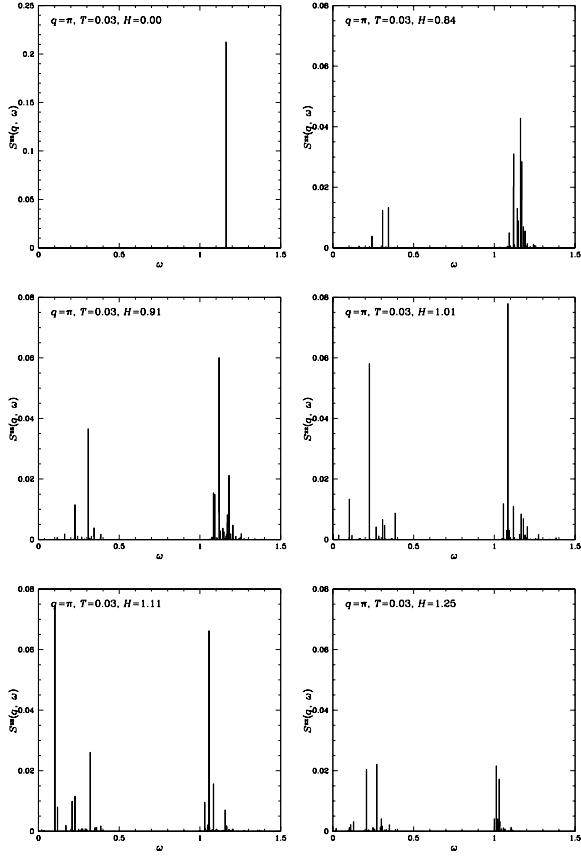


Figure 2.33: Longitudinal dynamic structure factor $S^{zz}(q = \pi, \omega)$ for $N = 16$, $T = 0.03J$, and $H = 0.00, 0.84, 0.91, 1.01, 1.11$, and $1.25J$. The first critical field is at $H \approx 0.81685J$, the saturation field at $H = 1.3J$. The resolution $\Delta\omega$ is 0.002.

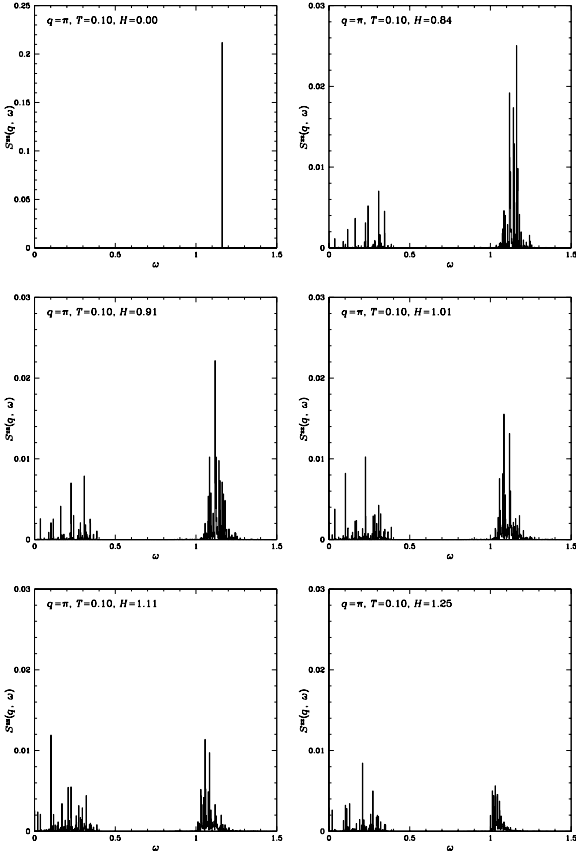


Figure 2.34: Longitudinal dynamic structure factor $S^{zz}(q = \pi, \omega)$ for $N = 16$, $T = 0.10J$, and $H = 0.00, 0.84, 0.91, 1.01, 1.11$, and $1.25J$. The first critical field is at $H \approx 0.81685J$, the saturation field at $H = 1.3J$. The resolution $\Delta\omega$ is 0.002.

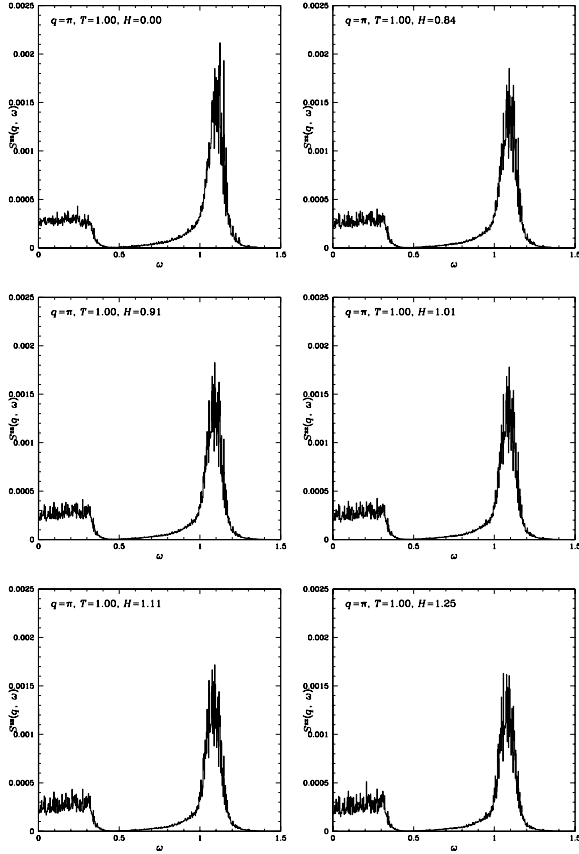


Figure 2.35: Longitudinal dynamic structure factor $S^{zz}(q = \pi, \omega)$ for $N = 16$, $T = 1.00J$, and $H = 0.00, 0.84, 0.91, 1.01, 1.11$, and $1.25J$. The first critical field is at $H \approx 0.81685J$, the saturation field at $H = 1.3J$. The resolution $\Delta\omega$ is 0.002 .

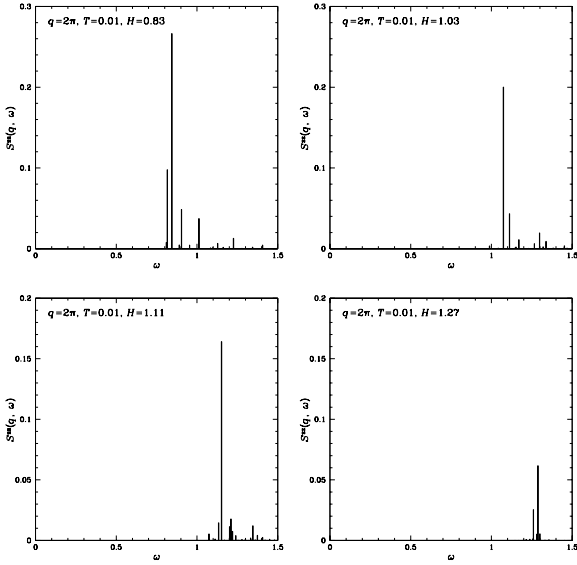


Figure 2.36: Longitudinal dynamic structure factor $S^{zz}(q = 2\pi, \omega)$ for $N = 20$, $T = 0.01J$, and $H = 0.83, 1.03, 1.11$, and $1.27J$. The first critical field is at $H \approx 0.81684J$, the saturation field at $H = 1.3J$. The resolution $\Delta\omega$ is 0.002.

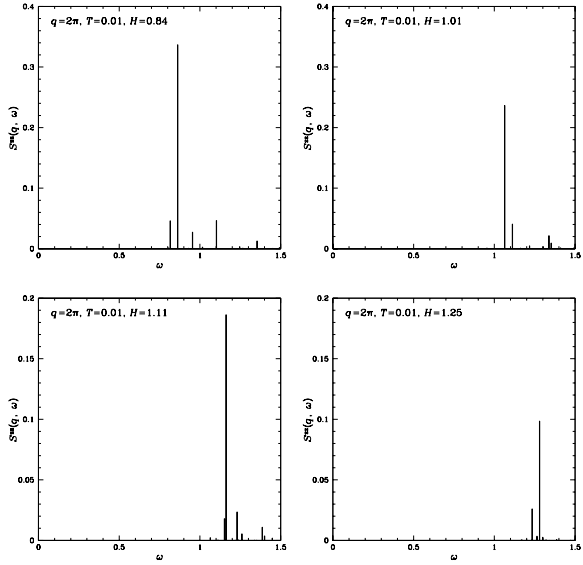


Figure 2.37: Longitudinal dynamic structure factor $S^{ZZ}(q = 2\pi, \omega)$ for $N = 16$, $T = 0.01J$, and $H = 0.84, 1.01, 1.11$, and $1.25J$. The first critical field is at $H \approx 0.81685J$, the saturation field at $H = 1.3J$. The resolution $\Delta\omega$ is 0.002 .

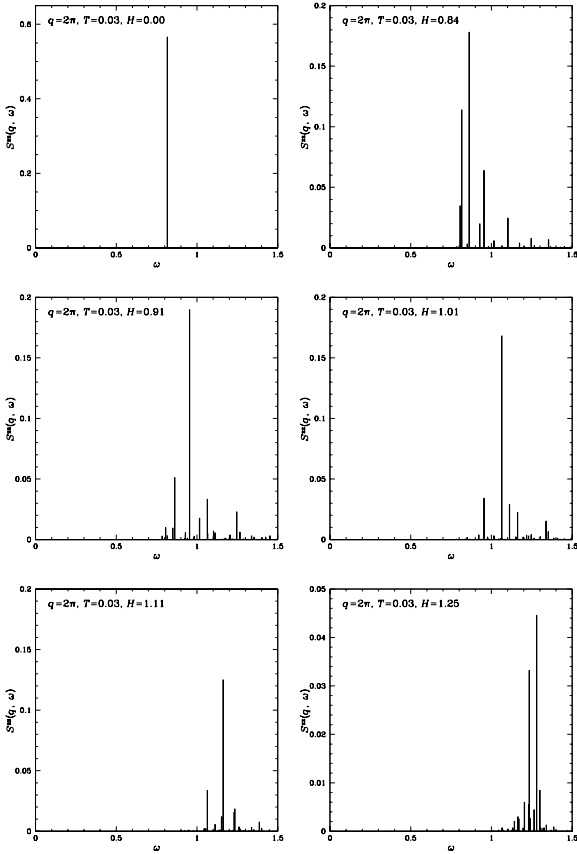


Figure 2.38: Longitudinal dynamic structure factor $S^{zz}(q = 2\pi, \omega)$ for $N = 16$, $T = 0.03J$, and $H = 0.00, 0.84, 0.91, 1.01, 1.11$, and $1.25J$. The first critical field is at $H \approx 0.81685J$, the saturation field at $H = 1.3J$. The resolution $\Delta\omega$ is 0.002 .

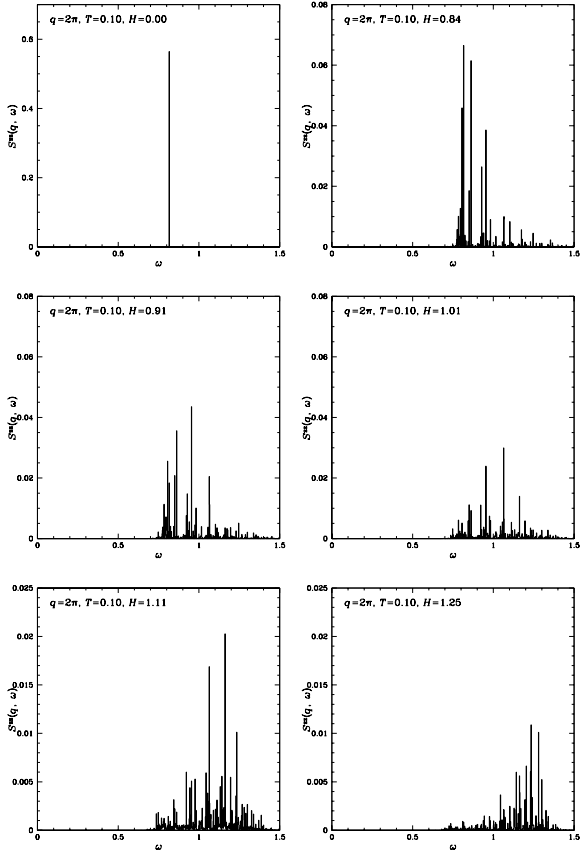


Figure 2.39: Longitudinal dynamic structure factor $S^{zz}(q = 2\pi, \omega)$ for $N = 16$, $T = 0.10J$, and $H = 0.00, 0.84, 0.91, 1.01, 1.11$, and $1.25J$. The first critical field is at $H \approx 0.81685J$, the saturation field at $H = 1.3J$. The resolution $\Delta\omega$ is 0.002.

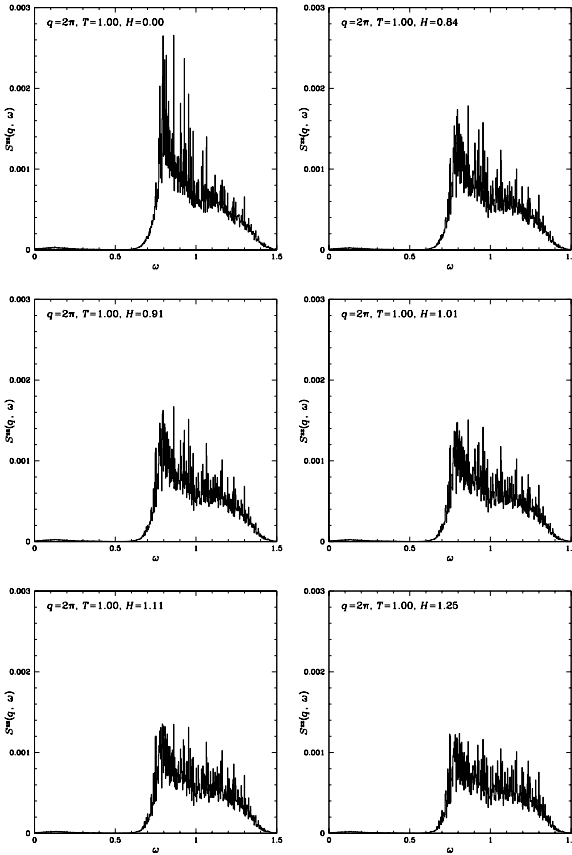


Figure 2.40: Longitudinal dynamic structure factor $S^{zz}(q = 2\pi, \omega)$ for $N = 16$, $T = 1.00J$, and $H = 0.00, 0.84, 0.91, 1.01, 1.11$, and $1.25J$. The first critical field is at $H \approx 0.81685J$, the saturation field at $H = 1.3J$. The resolution $\Delta\omega$ is 0.002.

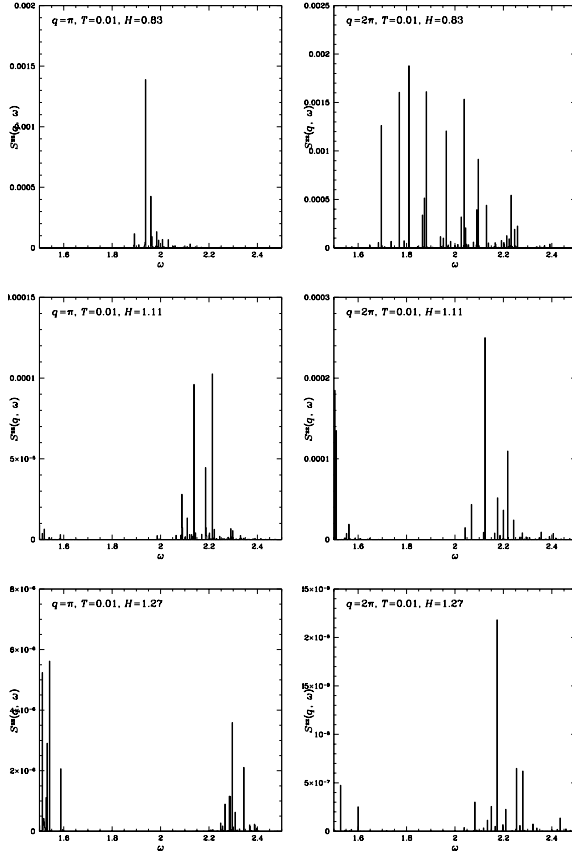


Figure 2.41: Two-magnon peak of the longitudinal dynamic structure factor $S^{\text{zz}}(q, \omega)$ for $N = 20$, $T = 0.01J$, and $H = 0.83, 1.11$, and $1.27J$. The first critical field is at $H \approx 0.81684J$, the saturation field at $H = 1.3J$. The resolution $\Delta\omega$ is 0.002.

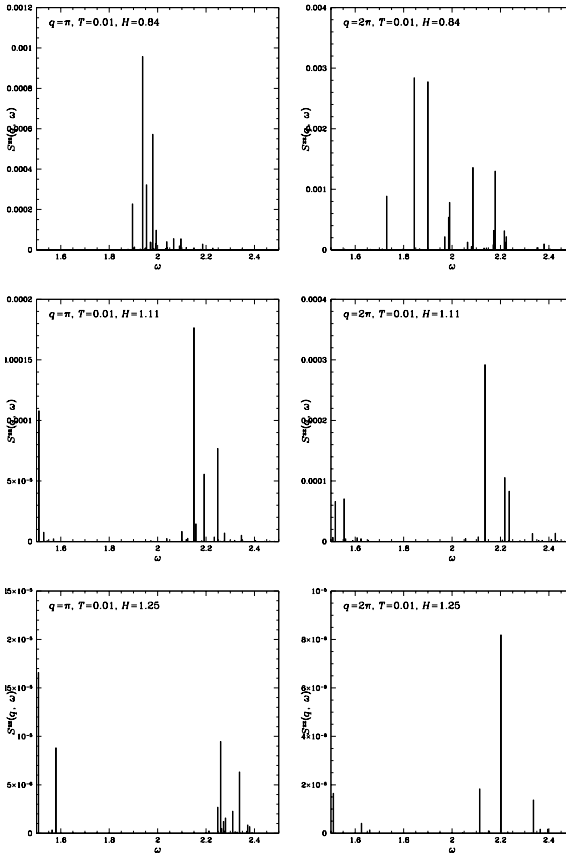


Figure 2.42: Two-magnon peak of the longitudinal dynamic structure factor $S^{zz}(q, \omega)$ for $N = 16$, $T = 0.01J$, and $H = 0.84, 1.11$, and $1.25J$. The first critical field is at $H \approx 0.81685J$, the saturation field at $H = 1.3J$. The resolution $\Delta\omega$ is 0.002.

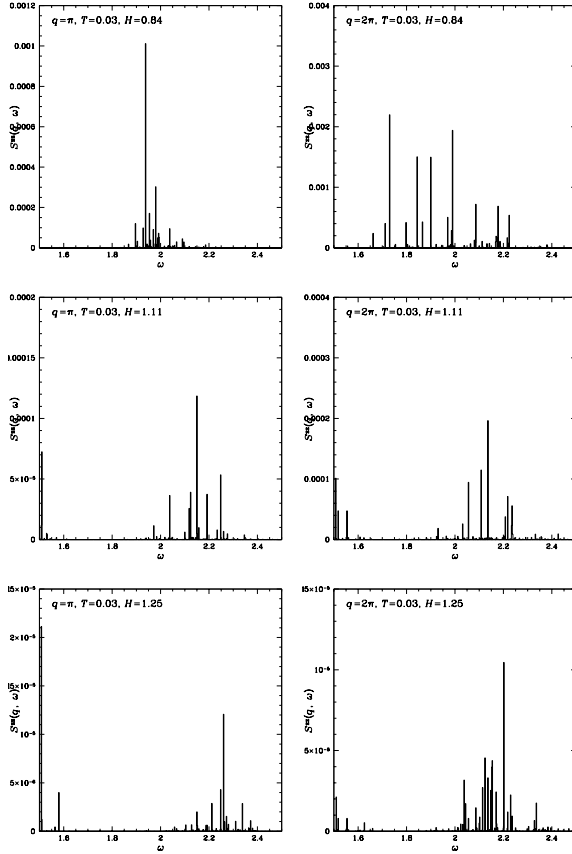


Figure 2.43: Two-magnon peak of the longitudinal dynamic structure factor $S^{zz}(q, \omega)$ for $N = 16$, $T = 0.03J$, and $H = 0.84, 1.11$, and $1.25J$. The first critical field is at $H \approx 0.81685J$, the saturation field at $H = 1.3J$. The resolution $\Delta\omega$ is 0.002.

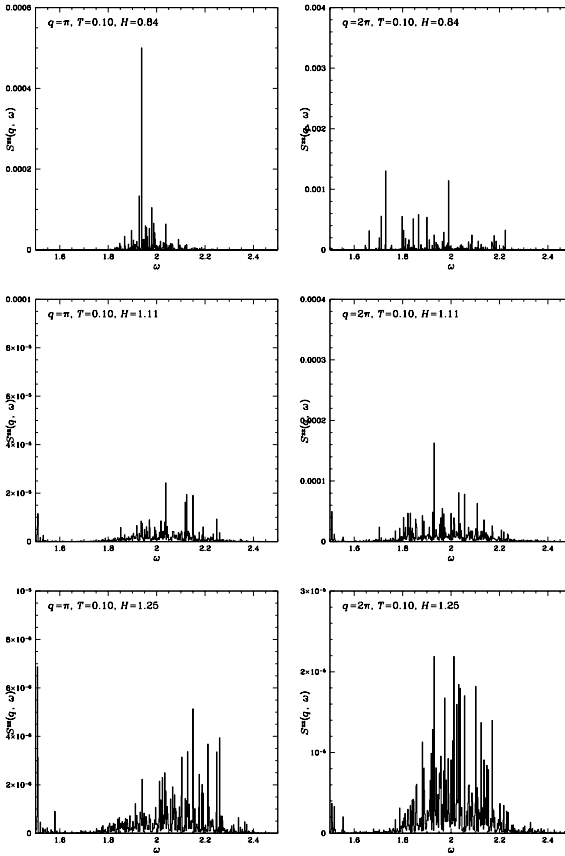


Figure 2.44: Two-magnon peak of the longitudinal dynamic structure factor $S^{zz}(q, \omega)$ for $N = 16$, $T = 0.10J$, and $H = 0.84, 1.11$, and $1.25J$. The first critical field is at $H \approx 0.81685J$, the saturation field at $H = 1.3J$. The resolution $\Delta\omega$ is 0.002.

The transverse structure factor

The transverse dynamic structure factor $S^{+-}(q, \omega)$ resp. $S^{-+}(q, \omega)$ involves transitions with $\Delta S_{\text{tot}}^z = \pm 1$, and therefore the Zeeman splitting causes a change in the energy transfer ω

$$\Delta\omega = -H\Delta S_{\text{tot}}^z = \begin{cases} H & \text{for } S^{+-}(q, \omega) \\ -H & \text{for } S^{-+}(q, \omega). \end{cases} \quad (2.30)$$

Figs. 2.45 ($q = \pi$) and 2.46 ($q = 2\pi$) show temperature scans of the transverse structure factor $S^{+-}(q, \omega)$ of a $N = 16$ and $N = 12$ bond alternating Heisenberg chain at magnetization $M = N/4 - 1$. For the very low temperature $T = 0.01J$, it was also possible to calculate the structure factors for $N = 20$, which are also displayed. The quantum features of this system can be easily identified only for temperatures $T \lesssim 0.03J$, whereas for $T \gtrsim 0.07J$ thermal excitations cover the underlying quantum structure.

The transverse structure factor has a strong one-magnon peak (at $\omega \approx 2J$ due to Zeeman splitting), which can be observed at all temperatures and all momenta. At higher temperatures, an asymmetry with emphasis on the high frequency side for $q = \pi$ and emphasis on the low frequency side for $q = 2\pi$ develops.

$q \neq 2\pi$ features also a strong central peak at $\omega \approx J$. For $q = 2\pi$, however, it is heavily suppressed, which can be understood with the help of the non-interacting dimer limit, cf. eqs. (2.23) and (2.24), which already show a vanishing central peak for $S^{+-}(q = 2\pi, \omega)$ (with $d = 1/2$ for equally spaced spins).

In addition, the figures show the inverse transitions of the one-magnon transitions close to $\omega = 0$. For the longitudinal structure factor, these transition have not been of interest, because they were proportional to the one-magnon peak with a proportionality factor corresponding to the Boltzmann factor. Here on the other hand, they are of interest, because they are truly independent of the one-magnon peak (for $H \neq 0$). In fact, they are the one-magnon peak of $S^{-+}(-q, -\omega)$ decorated with a Boltzmann-like factor, which is — after distributing the single transitions into the frequency bins — no longer reproducible.

For $q = 2\pi$, this inverse one-magnon transition remains strong even at low temperatures, which can be seen as a very strong peak at $\omega \approx 0$ in Figs. 2.46, whereas for $q = \pi$, it only sets in with thermal excitation of higher states or at high magnetizations. The corresponding transition is a strong dipole transition between the ground states of magnetization M and $M - 1$, which both have momentum $q = 0$,² hence the transition with $q = 2\pi$.

2. Depending on the number of spins N , the ground states may all be at $q = \pi$ instead of $q = 0$.

Figs. 2.47 ($N = 20, q = \pi$) and 2.48 ($N = 16, q = \pi$) as well as 2.53 ($N = 20, q = 2\pi$) and 2.54 ($N = 16, q = 2\pi$) compare the transverse structure factors $S^{+-}(q, \omega)$ of a bond alternating chain of $N = 20$ and $N = 16$ spins at temperature $T = 0.01J$ and various magnetizations. Like for the longitudinal structure factor, the overall line shape as well as all important features do not depend on the system size, only the details change.

Figs. 2.49 ($T = 0.03J, N = 16$), 2.50 ($T = 0.10J, N = 16$), 2.51 ($T = 0.10J, N = 12$), and 2.52 ($T = 1.00J, N = 12$) show magnetization (magnetic field) scans of the transverse structure factor $S^{+-}(q = \pi, \omega)$ of a bond alternating chain. Results for $N = 16$ sites and $T \geq 0.1J$ are not available due to the computational complexity of the transverse structure factor, but the comparison plots between $N = 16$ and $N = 12$ spins at $T = 0.1J$ show that they only differ in the details, whereas the essential features are nearly quantitatively identical.

First of all, the frequency of the transverse structure factor involves a magnetic field dependent Zeeman term. Therefore, a shift of the frequency (upwards for S^{+-} , downwards for S^{-+}) occurs with varying magnetic field and can indeed be observed at higher temperatures $T \gtrsim J$ (Fig. 2.52) and, to a lesser extent, also at $T \gtrsim 0.1J$ (Figs. 2.50 and 2.51). At the quantum level (Fig. 2.49), however, it cannot be observed at all: the observed shift is caused by the discreteness of the finite system and by the remaining thermal occupation. In the thermodynamic limit on the other hand, the main contribution is always at the threshold.

The $\omega = J$ transitions play an essential role at any magnetization. The $\omega = 0$ transitions grow considerably with increasing magnetization, while the $\omega = 2J$ transitions decrease with increasing magnetization.

Analogously, Figs. 2.55 ($T = 0.03J, N = 16$), 2.56 ($T = 0.10J, N = 16$), 2.56 ($T = 0.10J, N = 12$), and 2.58 ($T = 1.00J, N = 12$) show magnetization (magnetic field) scans of the transverse structure factor $S^{+-}(q = 2\pi, \omega)$ of a bond alternating chain. Again, results for $N = 16$ are only available for $T \leq 0.1J$ due to computational limits, but the comparison between $N = 16$ (Fig. 2.56) and $N = 12$ (Fig. 2.56) shows that the essential features are the identical.

As with $q = \pi$, the frequency of the transverse structure factor varies with the magnetic field due to Zeeman splitting, but in contrast to $q = \pi$, this is barely noticeable for non-zero magnetization and $q = 2\pi$ even at higher temperatures, and mostly for the $\omega \approx 2J$ peak (*cf.* Figs. 2.52 and 2.58).

As already seen in the temperature scan (Fig. 2.46), the transverse structure factor at $q = 2\pi$ does not feature a peak structure from intra band transitions, which would be roughly located at $\omega = H$.

The $\omega \approx 2J$ peak decreases considerably with increasing field.

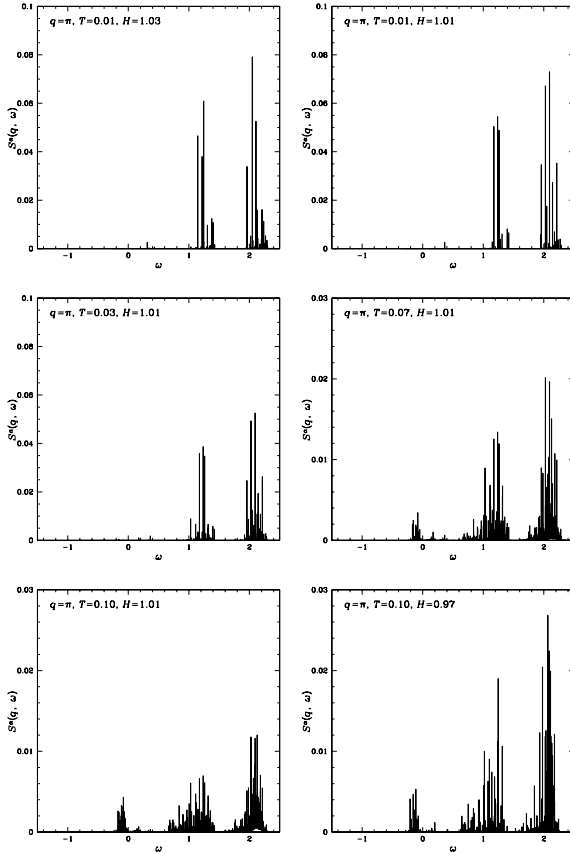


Figure 2.45: Transverse dynamic structure factor $S^{+-}(q = \pi, \omega)$ at magnetization $M = N/4 - 1$ ($H = 1.03J$ for $N = 20$, $H = 1.01J$ for $N = 16$, $H = 0.97J$ for $N = 12$), and $T = 0.01, 0.03, 0.07, 0.10, 0.50, 1.00, 2.00$, and $4.00J$. For comparison $T = 0.01J$ is presented for $N = 20$ and $N = 16$, and $T = 0.10J$ for $N = 16$ and $N = 12$. The first critical field is at $H \approx 0.81684$ ($N = 16$), $H \approx 0.81685J$ ($N = 16$) resp. $H \approx 0.81670J$ ($N = 12$), the saturation field at $H = 1.3J$. (continued)

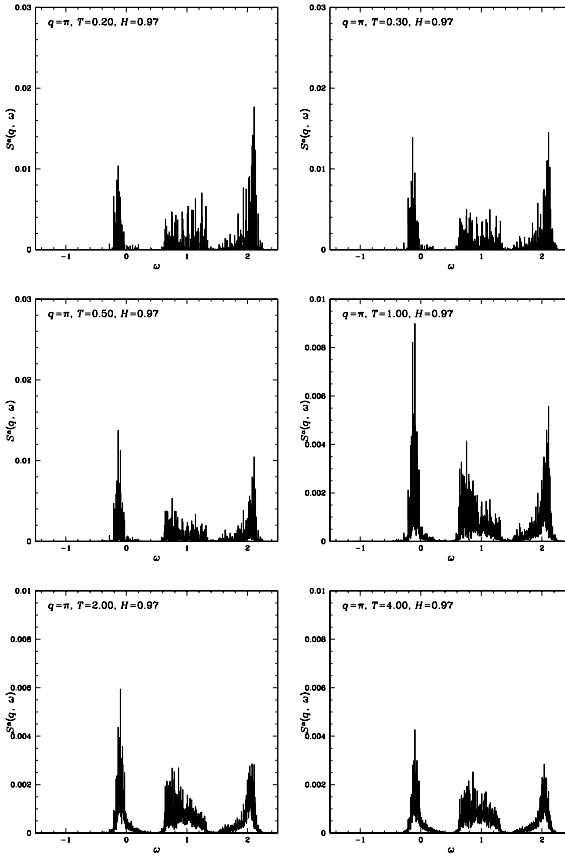


Figure 2.45: (continued) Transverse dynamic structure factor $S^{+-}(q = \pi, \omega)$ for magnetization $M = N/4 - 1$ ($H = 0.97J$), $N = 12$, and $T = 0.20, 0.30, 0.50, 1.00, 2.00$, and $4.00J$. The first critical field is at $H \approx 0.81670J$, the saturation field at $H = 1.3J$. The resolution $\Delta\omega$ is 0.002 .

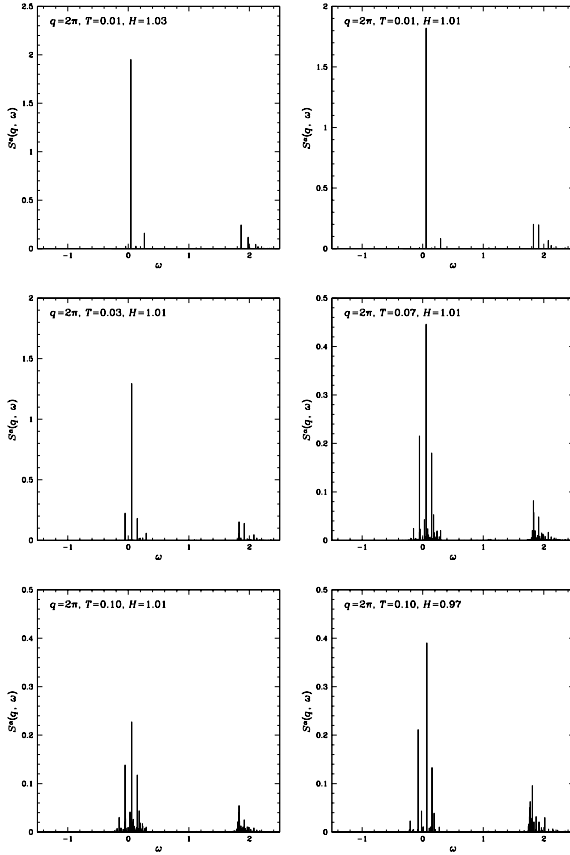


Figure 2.46: Transverse dynamic structure factor $S^{+-}(q = 2\pi, \omega)$ at magnetization $M = N/4 - 1$ ($H = 1.03J$ for $N = 20$, $H = 1.01J$ for $N = 16$, $H = 0.97J$ for $N = 12$), and $T = 0.01, 0.03, 0.07, 0.10$. For comparison, $T = 0.01J$ is presented for $N = 20$ and $N = 16$, and $T = 0.10J$ for $N = 16$ and $N = 12$. The first critical field is at $H \approx 0.81684$ ($N = 20$), $H \approx 0.81685J$ ($N = 16$) resp. $H \approx 0.81670J$ ($N = 12$), the saturation field at $H = 1.3J$. (continued)

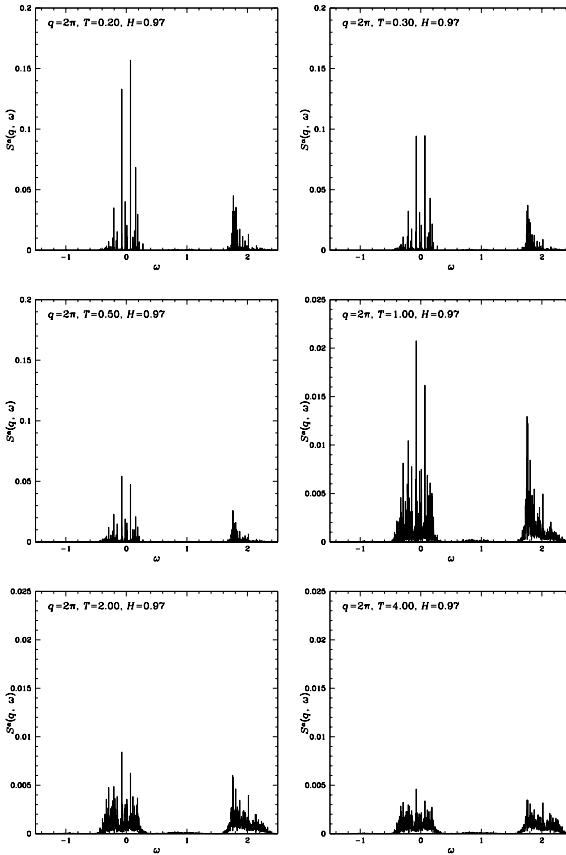


Figure 2.46: (continued) Transverse dynamic structure factor $S^{+-}(q = 2\pi, \omega)$ for magnetization $M = N/4 - 1$ ($H = 0.97J$), $N = 12$, and $T = 0.20, 0.30, 0.50, 1.00, 2.00$, and $4.00J$. The first critical field is at $H \approx 0.81670J$, the saturation field at $H = 1.3J$. The resolution $\Delta\omega$ is 0.002 .

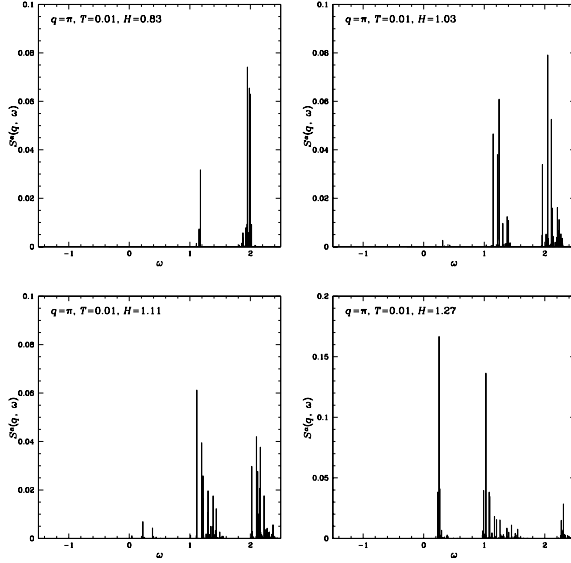


Figure 2.47: Transverse dynamic structure factor $S^{+-}(q = 2\pi, \omega)$ for $N = 20$, $T = 0.01J$, and $H = 0.83, 1.03, 1.11,$ and $1.27J$. The first critical field is at $H \approx 0.81684J$, the saturation field at $H = 1.3J$. The resolution $\Delta\omega$ is 0.002.

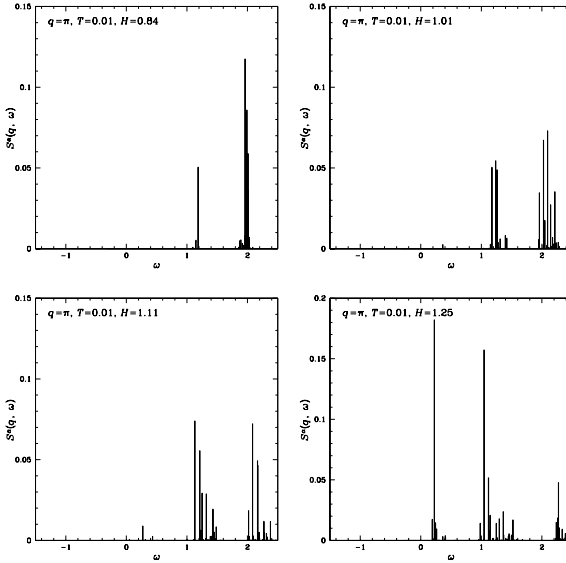


Figure 2.48: Transverse dynamic structure factor $S^{+-}(q = \pi, \omega)$ for $N = 16$, $T = 0.01J$, and $H = 0.84, 1.01, 1.11$, and $1.25J$. The first critical field is at $H \approx 0.81685J$, the saturation field at $H = 1.3J$. The resolution $\Delta\omega$ is 0.002.

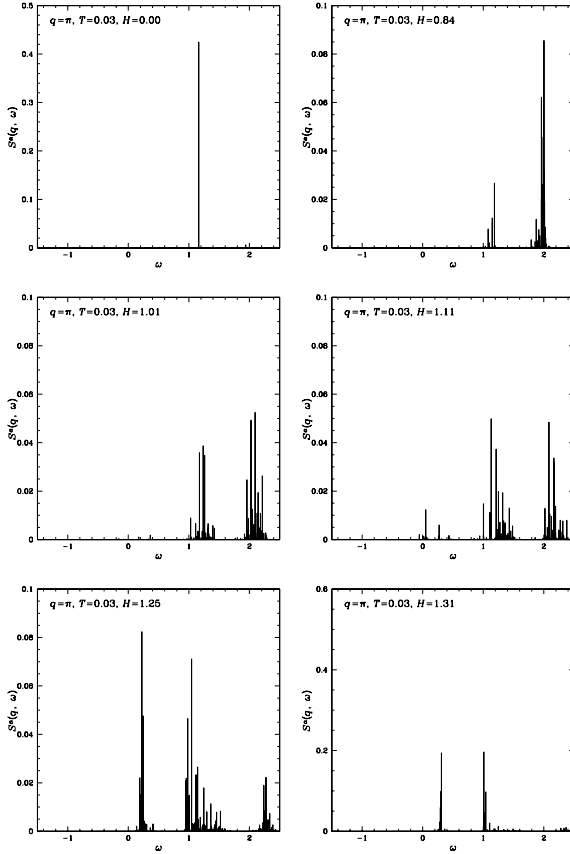


Figure 2.49: Transverse dynamic structure factor $S^{+-}(q = \pi, \omega)$ for $N = 16$, $T = 0.03J$, and $H = 0.00, 0.84, 1.01, 1.11, 1.25$, and $1.31J$. The first critical field is at $H \approx 0.81685J$, the saturation field at $H = 1.3J$. The resolution $\Delta\omega$ is 0.002.

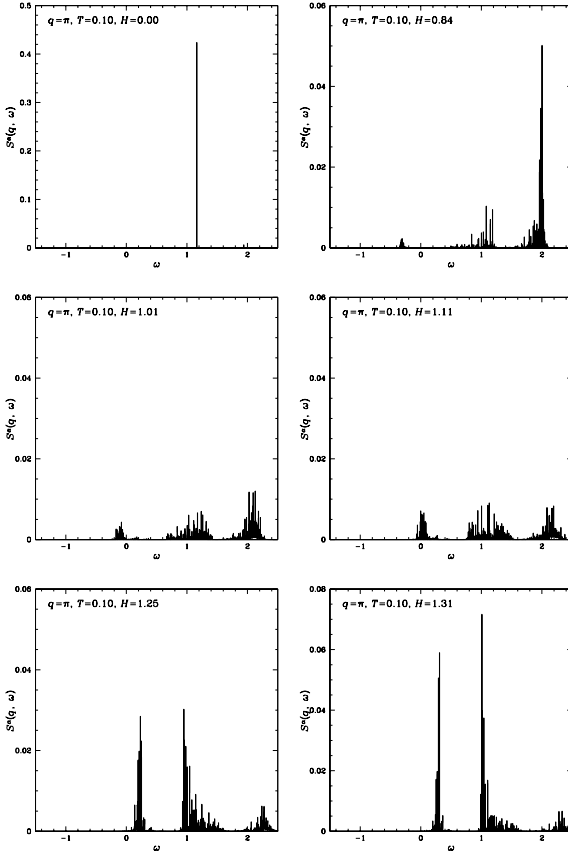


Figure 2.50: Transverse dynamic structure factor $S^-(q = \pi, \omega)$ for $N = 16$, $T = 0.1J$, and $H = 0.00, 0.84, 1.01, 1.11, 1.25$, and $1.31J$. The first critical field is at $H \approx 0.81685J$, the saturation field at $H = 1.3J$. The resolution $\Delta\omega$ is 0.002.

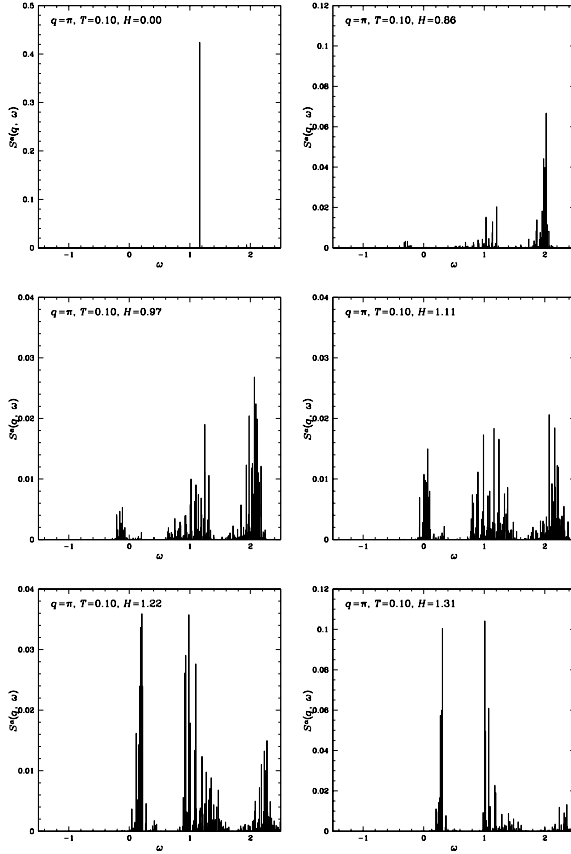


Figure 2.51: Transverse dynamic structure factor $S^{+-}(q = 2\pi, \omega)$ for $N = 12$, $T = 0.1J$, and $H = 0.00, 0.86, 0.97, 1.11, 1.22$, and $1.31J$. The first critical field is at $H \approx 0.81670J$, the saturation field at $H = 1.3J$. The resolution $\Delta\omega$ is 0.002 .

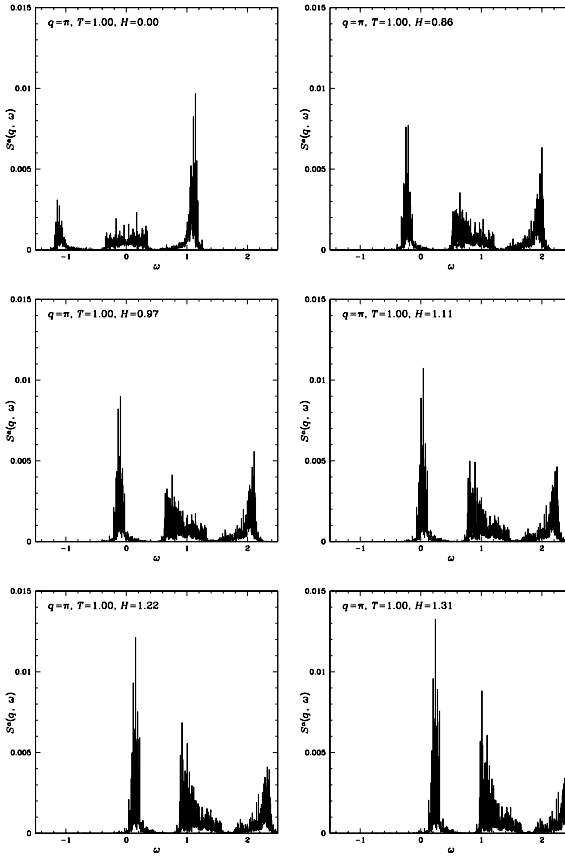


Figure 2.52: Transverse dynamic structure factor $S^{+-}(q = \pi, \omega)$ for $N = 12$, $T = 1.0J$, and $H = 0.00, 0.86, 0.97, 1.11, 1.22$, and $1.31J$. The first critical field is at $H \approx 0.81670J$, the saturation field at $H = 1.3J$. The resolution $\Delta\omega$ is 0.002 .

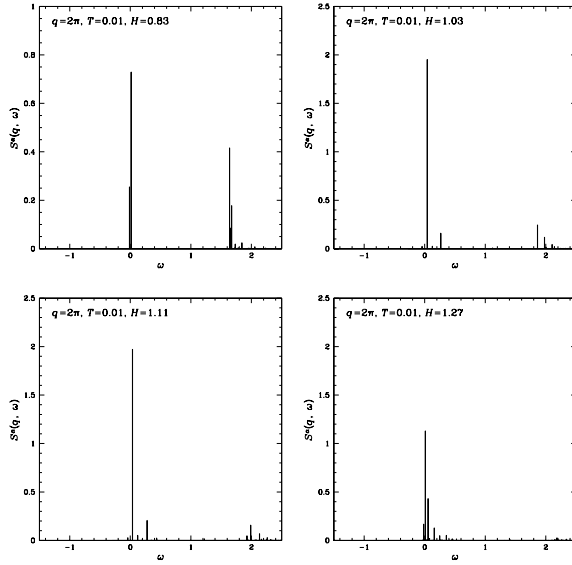


Figure 2.53: Transverse dynamic structure factor $S^{+-}(q = 2\pi, \omega)$ for $N = 20$, $T = 0.01J$, and $H = 0.83, 1.03, 1.11$, and $1.27J$. The first critical field is at $H \approx 0.81684J$, the saturation field at $H = 1.3J$. The resolution $\Delta\omega$ is 0.002.

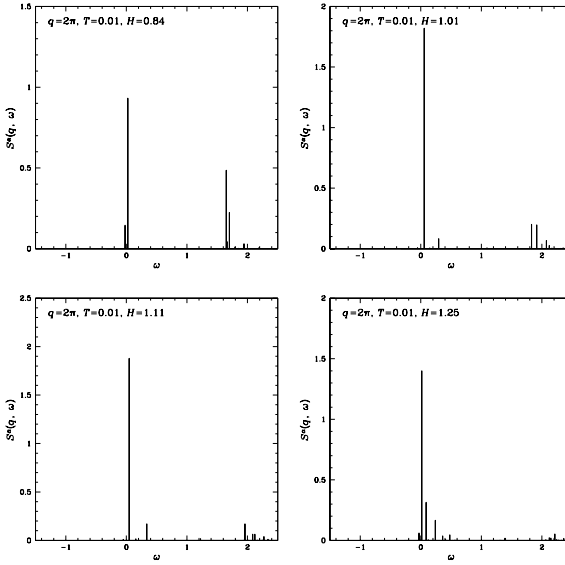


Figure 2.54: Transverse dynamic structure factor $S^{+-}(q = 2\pi, \omega)$ for $N = 16$, $T = 0.01J$, and $H = 0.84, 1.01, 1.11$, and $1.25J$. The first critical field is at $H \approx 0.81685J$, the saturation field at $H = 1.3J$. The resolution $\Delta\omega$ is 0.002.

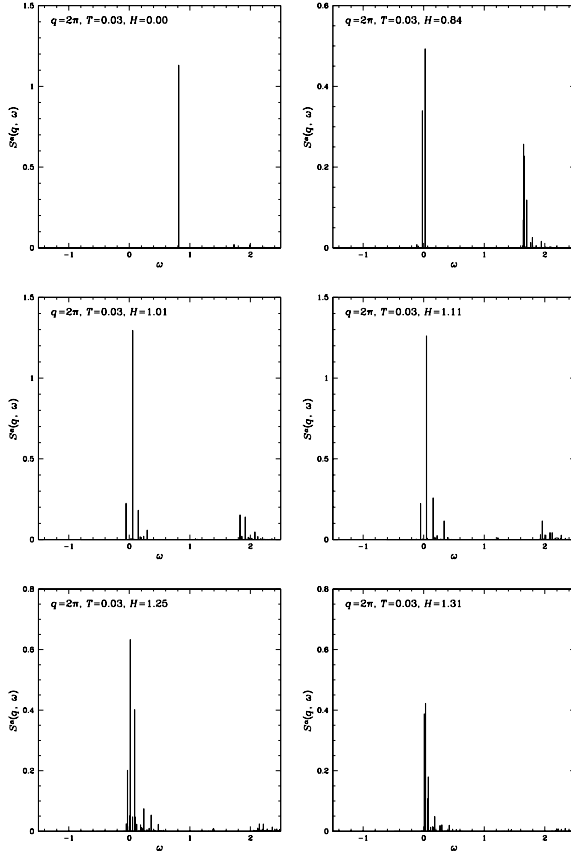


Figure 2.55: Transverse dynamic structure factor $S^{+-}(q = 2\pi, \omega)$ for $N = 16$, $T = 0.03J$, and $H = 0.00, 0.84, 1.01, 1.11, 1.25$, and $1.31J$. The first critical field is at $H \approx 0.81685J$, the saturation field at $H = 1.3J$. The resolution $\Delta\omega$ is 0.002.

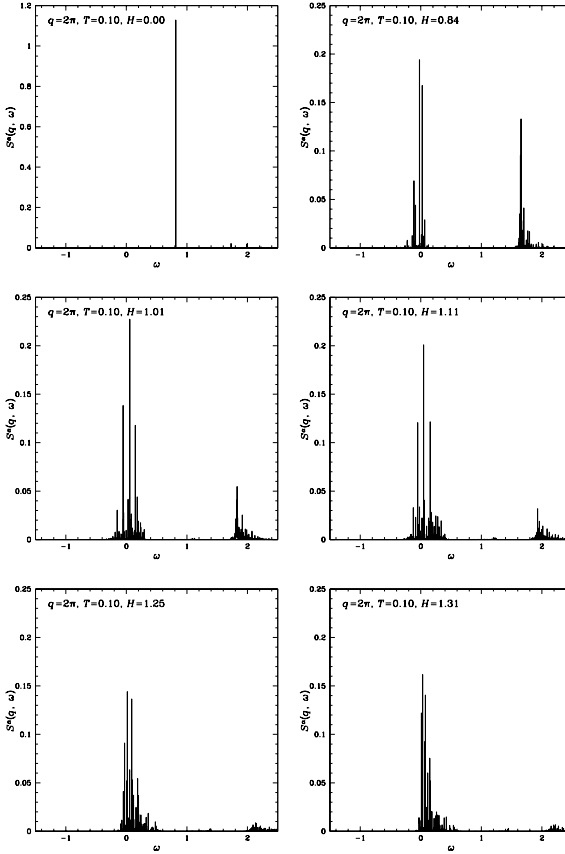


Figure 2.56: Transverse dynamic structure factor $S^{+-}(q = 2\pi, \omega)$ for $N = 16$, $T = 0.1J$, and $H = 0.00, 0.84, 1.01, 1.11, 1.25$, and $1.31J$. The first critical field is at $H \approx 0.81685J$, the saturation field at $H = 1.3J$. The resolution $\Delta\omega$ is 0.002 .

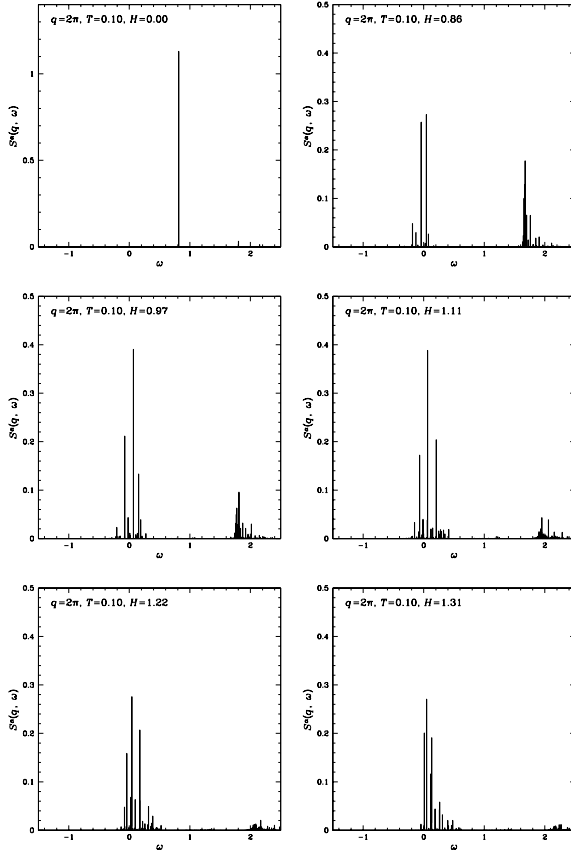


Figure 2.57: Transverse dynamic structure factor $S^{+-}(q = 2\pi, \omega)$ for $N = 12$, $T = 0.1J$, and $H = 0.00, 0.86, 0.97, 1.11, 1.22$, and $1.31J$. The first critical field is at $H \approx 0.81670J$, the saturation field at $H = 1.3J$. The resolution $\Delta\omega$ is 0.002 .

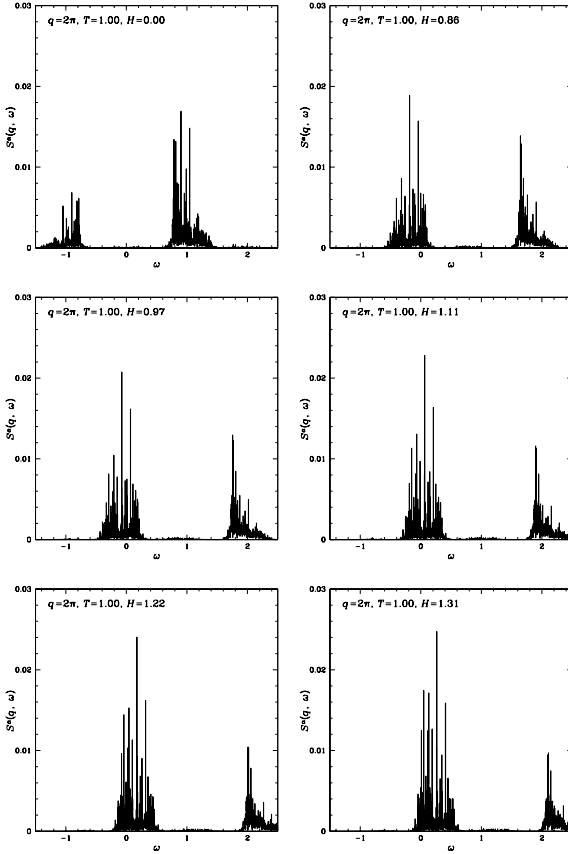


Figure 2.58: Transverse dynamic structure factor $S^-(q = 2\pi, \omega)$ for $N = 12$, $T = 1.0J$, and $H = 0.00, 0.86, 0.97, 1.11, 1.22$, and $1.31J$. The first critical field is at $H \approx 0.81670J$, the saturation field at $H = 1.3J$. The resolution $\Delta\omega$ is 0.002 .

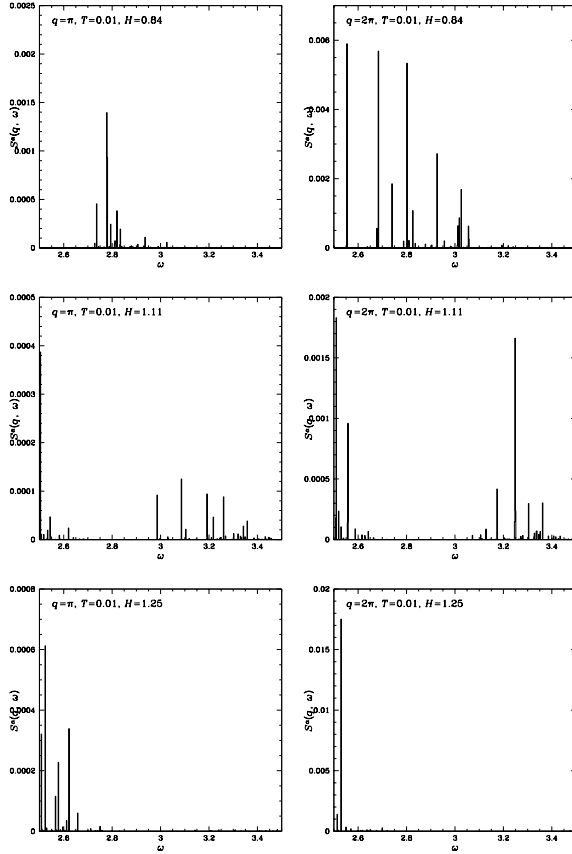


Figure 2.59: Two-magnon peak of the transverse dynamic structure factor $S^{+-}(q, \omega)$ for $N = 16$, $T = 0.01J$, and $H = 0.84, 1.11$, and $1.29J$. The first critical field is at $H \approx 0.81685J$, the saturation field at $H = 1.3J$. The resolution $\Delta\omega$ is 0.002.

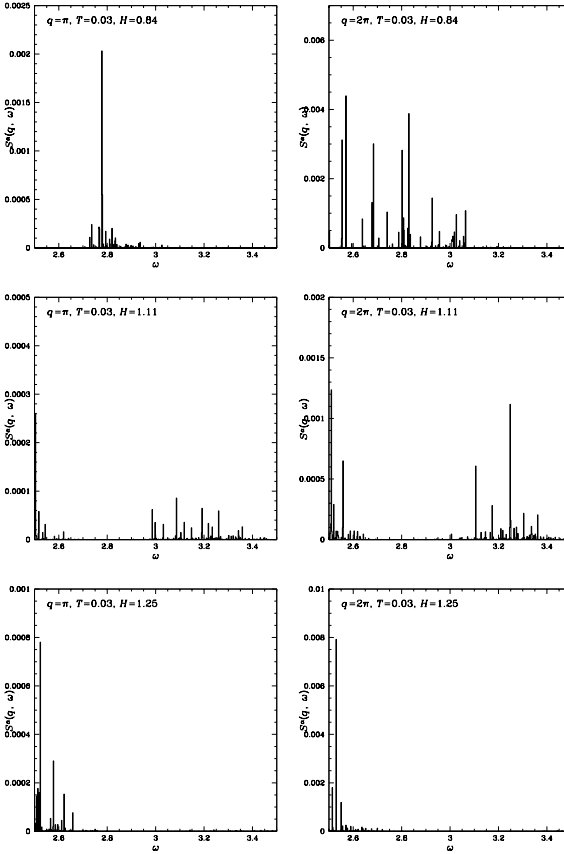


Figure 2.60: Two-magnon peak of the transverse dynamic structure factor $S^{+-}(q, \omega)$ for $N = 16$, $T = 0.03J$, and $H = 0.84, 1.11$, and $1.29J$. The first critical field is at $H \approx 0.81685J$, the saturation field at $H = 1.3J$. The resolution $\Delta\omega$ is 0.002.

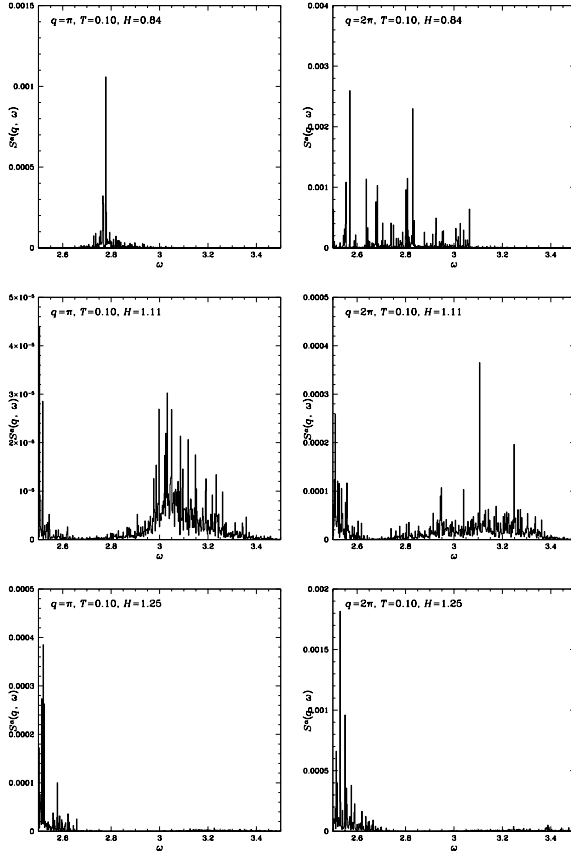


Figure 2.61: Two-magnon peak of the transverse dynamic structure factor $S^{+-}(q, \omega)$ for $N = 16$, $T = 0.10J$, and $H = 0.84, 1.11$, and $1.29J$. The first critical field is at $H \approx 0.81685J$, the saturation field at $H = 1.3J$. The resolution $\Delta\omega$ is 0.002.

CHAPTER 3

The Diamond Type Chain

3.1 Introduction

The diamond type chain can be considered as a variant of the Heisenberg chain with next nearest neighbour interaction. Its structure and interactions are shown in two alternative but equivalent ways in Fig. 3.1. Compared to the former, the elementary cell is increased to three lattice sites, allowing for spatial variation of both nearest and next nearest neighbour interactions. Due to the triangular structure, the diamond chain is an example for frustrated systems.

3.1.1 Hamiltonian of the diamond chain

The Hamilton operator of the diamond chain is

$$\mathcal{H} = \sum_{j=1}^{\frac{N}{3}} \left[\begin{aligned} & J_1 (\vec{S}_{3j} \cdot \vec{S}_{3j+1} + \vec{S}_{3j+2} \cdot \vec{S}_{3j+3}) \\ & + J_2 (\vec{S}_{3j+1} \cdot \vec{S}_{3j+2}) \\ & + J_3 (\vec{S}_{3j} \cdot \vec{S}_{3j+2} + \vec{S}_{3j+1} \cdot \vec{S}_{3j+3}) \end{aligned} \right] \quad (3.1)$$

Detailed work on the diamond type chain has been performed about a decade ago [20], the first brief study was even earlier by SHASTRY AND SUTHERLAND [21].

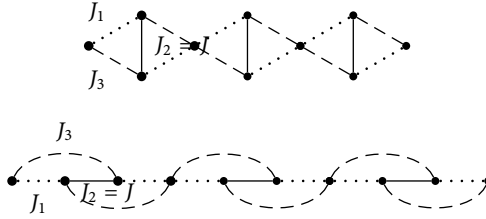


Figure 3.1: Schematic diagram of the diamond type chain. Both representations are equivalent. (a) illustrates the name ‘diamond chain’, (b) shows the diamond chain as generalization of the Heisenberg antiferromagnetic chain with next nearest neighbour interaction.

Since then, a number of detailed theoretical and numerical studies have been published [22, 23, 24]. On the material side, it appears that $\text{Cu}_3(\text{CO}_3)_2(\text{OH})_2$ (azurite) is an approximate realization of the diamond type chain with coupling constants $J_1 = 19$ K, $J_2 = 24$ K, and $J_3 = 8.6$ K [25].

Of particular interest is the symmetric diamond chain with $J_1 = J_3 = \frac{\gamma}{2}J_2$ with the Hamilton operator

$$\mathcal{H} = \mathcal{H}_{\text{sym}} = \sum_{j=1}^{\frac{N}{3}} \left[J_1 (\vec{S}_{3j} + \vec{S}_{3j+3}) \cdot (\vec{S}_{3j+1} + \vec{S}_{3j+2}) + J_2 (\vec{S}_{3j+1} \cdot \vec{S}_{3j+2}) \right] \quad (3.2a)$$

$$= \sum_{j=1}^{\frac{N}{3}} J_2 \left[(\vec{S}_{3j+1} \cdot \vec{S}_{3j+2}) + \frac{\gamma}{2} (\vec{S}_{3j} + \vec{S}_{3j+3}) \cdot (\vec{S}_{3j+1} + \vec{S}_{3j+2}) \right] \quad (3.2b)$$

$$= \sum_{j=1}^{\frac{N}{3}} \frac{J_2}{2} \left[(\vec{S}_{3j+1} + \vec{S}_{3j+2})^2 - \frac{3}{2} + \gamma (\vec{S}_{3j} + \vec{S}_{3j+3}) \cdot (\vec{S}_{3j+1} + \vec{S}_{3j+2}) \right] \quad (3.2c)$$

This special case has the property that the total spin on each J_2 bond $\vec{S}_{2,\text{tot}} = \vec{S}_{3j+1} + \vec{S}_{3j+2}$ is conserved, and $S_{2,\text{tot}}$ takes the values 0 (singlet) or 1 (triplet). The

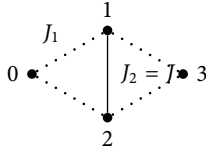


Figure 3.2: The symmetric tetramer

general state of the symmetric diamond chain can thus be classified by specifying the spins $\vec{S}_{j,\text{tot}}$ and the remaining $N/3$ spins at positions $3j$ ($j = 1, 2, \dots, N/3$).

In this work I have set the units by $J_2 = J = 1$, the number of spins is N , which in combination with three spin unit cells gives $N/3$ unit cells and $N/6 + 1$ wave vectors in the range from $0 < k < \pi$. Computational resources limited the available system sizes to $N = 12$ and $N = 18$ spins for full diagonalization and $N = 24$ for the Lanczos method, when only the four lowest states are available for each wave vector and magnetization.

One also has got to take finite size effects into account: For $N = 12$ and 24 the ground state is at $q = 0$ whereas it is at $q = \pi$ for $N = 18$. Hence the order of wave vectors must be inverted for $N = 18$, as I am interested in wave vectors relative to the ground state: $q = 0$ for $N = 18$ should be compared to $q = \pi$ for $N = 12$ and 24 and vice versa. The remaining wave vectors do not match with the only exception of $q = \pi/2$ for $N = 12$ and 24 .

For the discussion of the properties of the diamond chain, it is instructive to consider first a single tetramer, which is the fundamental building block of the diamond chain. The simpler symmetric tetramer ($J_1 = J_3$) will be discussed in Section 3.1.2, the distorted tetramer ($J_1 \neq J_3$) in Section 3.1.3.

3.1.2 The symmetric tetramer

The structure of the symmetric tetramer is shown in Fig. 3.2, and the Hamilton operator for this system is

$$\mathcal{H} = \mathcal{H}_{\text{sym}} = J_1 [\vec{S}_0 \cdot \vec{S}_1 + \vec{S}_0 \cdot \vec{S}_2 + \vec{S}_3 \cdot \vec{S}_1 + \vec{S}_3 \cdot \vec{S}_2] + J_2 \vec{S}_1 \cdot \vec{S}_2 \quad (3.3a)$$

$$= J_1 (\vec{S}_0 + \vec{S}_3) \cdot (\vec{S}_1 + \vec{S}_2) + \frac{J_2}{2} ((\vec{S}_1 + \vec{S}_2)^2 - \frac{3}{2}) \quad (3.3b)$$

$$= J_2 \left[\frac{J_1}{2} (\vec{S}_0 + \vec{S}_3) \cdot (\vec{S}_1 + \vec{S}_2) + \frac{1}{2} ((\vec{S}_1 + \vec{S}_2)^2 - \frac{3}{2}) \right] \quad (3.3c)$$

where $\gamma = \frac{2J_1}{J_2}$ is introduced.

It is obvious from this representation of the Hamilton operator that the total spin of both spin pairs (03) and (12) is a good quantum number, hence the eigenstates can be classified accordingly and the energies are obtained as given in Table 3.1. The states 1 and 2 are straightforward with singlets on the strong J_2 coupling (12) and single spins on sites 0 and 3. In this case, the single spins on 0 and 3 are even free spins, because the states 1 and 2 are (fourfold) degenerate.

From Table 3.1 I also find the ground states of the symmetric tetramer. For $\gamma < 1$ ($J_1 < \frac{J_2}{2}$), states 1 and 2 form a fourfold degenerate ground state, whereas for $\gamma > 1$ ($J_1 > \frac{J_2}{2}$) state 4a is the only ground state. At $\gamma = 1$ ($J_1 = \frac{J_2}{2}$) they meet in energy, resulting in a fivefold degenerate ground state.

Since these building blocks also appear in the low lying excited states of the diamond chain, I shall introduce a shorthand notation used in the following discussion of the diamond chain: $\times S \times$ denotes the singlet along J_2 with one free spin on each side, T denotes the four spin (tetramer) singlet of state 4a.

3.1.3 The distorted tetramer

The structure of the distorted tetramer is shown in Fig. 3.3, and the Hamilton operator for this system is

$$\mathcal{H} = J_1 (\vec{S}_0 \cdot \vec{S}_1 + \vec{S}_3 \cdot \vec{S}_2) + J_3 (\vec{S}_0 \cdot \vec{S}_2 + \vec{S}_3 \cdot \vec{S}_1) + J_2 \vec{S}_1 \cdot \vec{S}_2 \quad (3.4a)$$

$$= \frac{J_1 + J_3}{2} (\vec{S}_0 + \vec{S}_3) \cdot (\vec{S}_1 + \vec{S}_2) + \frac{J_1 - J_3}{2} (\vec{S}_0 - \vec{S}_3) \cdot (\vec{S}_1 - \vec{S}_2) + \frac{J_2}{2} ((\vec{S}_1 + \vec{S}_2)^2 - \frac{3}{2}) \quad (3.4b)$$

$$= \mathcal{H}_{\text{sym}} + \frac{J_1 - J_3}{2} (\vec{S}_0 - \vec{S}_3) \cdot (\vec{S}_1 - \vec{S}_2). \quad (3.4c)$$

In contrast to the symmetric tetramer, there are no simple combinations of spins which are conserved. The total spin however is still conserved.

It is straightforward to calculate the spectrum of the distorted tetramer by diagonalizing the term proportional to $J_1 - J_3$ in eq. (3.4) in the basis of the symmetric tetramer states Table 3.1. The resulting eigenstates of the distorted tetramer are displayed in Table 3.2.

3.1.4 The quantum phase diagram of the diamond chain

The quantum phase diagram of the diamond type chain has been discussed in detail in [23] and is shown in Fig. 3.4 in the variables J_3 over J_1 , choosing the coupling J_2 as energy unit with $J_2 = J = 1$. The symmetry upon interchange of J_1 and J_3 is evident from the Hamilton operator eq. (3.1).

Table 3.1: Eigenstates of the symmetric tetramer

\mathcal{N}^a	S_{12}	S_{03}	S_{tot}	ϵ	degeneracy
1	0	0	0	$-\frac{3}{4}J_2 = -\frac{3}{4}J_2$	1
2	0	1	1	$-\frac{3}{4}J_2 = -\frac{3}{4}J_2$	3
3	1	0	1	$-\frac{1}{4}J_2 = -\frac{1}{4}J_2$	3
4a	1	1	0	$-2J_1 + \frac{1}{4}J_2 = \left(-\gamma + \frac{1}{4}\right)J_2$	1
4b	1	1	1	$-J_1 + \frac{1}{4}J_2 = \left(-\frac{\gamma}{2} + \frac{1}{4}\right)J_2$	3
4c	1	1	2	$J_1 + \frac{1}{4}J_2 = \left(\frac{\gamma}{2} + \frac{1}{4}\right)J_2$	5

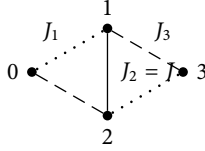


Figure 3.3: The distorted tetramer

Qualitatively, three regimes can be distinguished:

Spin fluid regime

The typical ground state in this regime consists of singlet dimers along the J_2 bonds. On the symmetry line $J_1 = J_3$, the spins in between are free spins $\frac{1}{2}$ and account for a $2^{\frac{N}{3}}$ -fold degeneracy. It is proven below that this is the exact ground state for $\gamma < 1$. Deviating from the symmetry ($J_1 \neq J_3$), the formerly free spins at positions $3j$ become weakly coupled and form a low energetic subsystem close to a Heisenberg antiferromagnetic chain, which will be investigated in detail in Section 3.2.1. This low energetic subsystem is responsible for the plateau at $\frac{1}{3}$ magnetization, where the weakly coupled spins are already fully polarized but the dimers are still in their respective ground state.

In order to find the exact ground state of the symmetric diamond chain, it is useful to rewrite the Hamilton operator eq. (3.2) once more

$$\mathcal{H}_{\text{sym}} = \sum_{j=1}^{\frac{N}{3}} \frac{J}{4} \left[(\gamma \vec{S}_{3j} + \vec{S}_{3j+1} + \vec{S}_{3j+2})^2 + (\vec{S}_{3j+1} + \vec{S}_{3j+2} + \gamma \vec{S}_{3j+3})^2 \right] - \frac{2 + \gamma^2}{8} NJ \quad (3.5)$$

Due to the quadratic form it is possible to give a lower bound of the energy, and if it is possible to find eigenstates with exactly this energy they have to be ground states.

Obviously, the minimal energy is obtained when both

$$(\gamma \vec{S}_{3j} + \vec{S}_{3j+1} + \vec{S}_{3j+2})^2 \quad \text{and} \quad (3.6a)$$

$$(\vec{S}_{3j+1} + \vec{S}_{3j+2} + \gamma \vec{S}_{3j+3})^2 \quad (3.6b)$$

Table 3.2: Eigenstates of the distorted tetramer

\mathcal{N}^o	S_{tot}	ϵ	degeneracy
1	0	$-\frac{1}{4}J_2 - \frac{1}{2}(J_1 + J_3) - \sqrt{(J_1 - J_3)^2 + (J_1 - \frac{1}{2})(J_3 - \frac{1}{2})}$	1
2	1	$-\frac{1}{4}J_2 - \frac{1}{2}\sqrt{(J_1 - J_3)^2 + 1}$	3
3	1	$-\frac{1}{4}J_2 + \frac{1}{2}\sqrt{(J_1 - J_3)^2 + 1}$	3
4a	0	$-\frac{1}{4}J_2 - \frac{1}{2}(J_1 + J_3) + \sqrt{(J_1 - J_3)^2 + (J_1 - \frac{1}{2})(J_3 - \frac{1}{2})}$	1
4b	1	$\frac{1}{4}J_2 - \frac{1}{2}(J_1 + J_3)$	3
4c	2	$\frac{1}{4}J_2 + \frac{1}{2}(J_1 + J_3)$	5

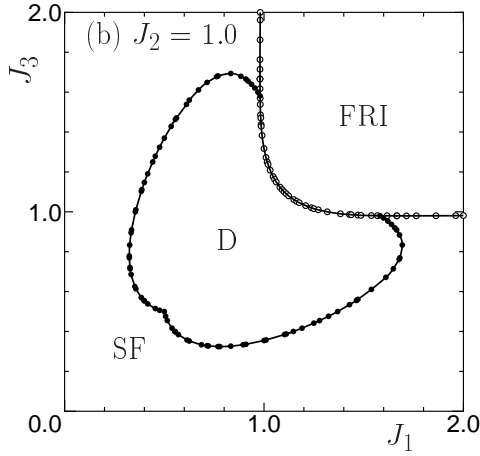


Figure 3.4: (from [23]) Phase diagram of the diamond chain in J_3 over J_1 with $J_2 = J = 1$. The symmetry upon interchange of J_1 and J_3 is evident from the Hamiltonian eq. (3.1).

are minimal for all j . This gives a lower boundary of

$$\begin{aligned}
 & (\gamma \vec{S}_{3j} + \vec{S}_{3j+1} + \vec{S}_{3j+2})^2 \\
 &= (\gamma \vec{S}_{3j})^2 + (\vec{S}_{3j+1} + \vec{S}_{3j+2})^2 \\
 & \quad + \gamma \left[(\vec{S}_{3j} + \vec{S}_{3j+1} + \vec{S}_{3j+2})^2 - \vec{S}_{3j}^2 - (\vec{S}_{3j+1} + \vec{S}_{3j+2})^2 \right] \quad (3.7a)
 \end{aligned}$$

$$\geq \frac{3}{4} \gamma^2 - (\gamma - 1) (\vec{S}_{3j+1} + \vec{S}_{3j+2})^2 \quad (3.7b)$$

$$\geq \frac{3}{4} \gamma^2 - \begin{cases} 0 & , \gamma < 1 \\ 2(\gamma - 1) & , \gamma > 1 \end{cases} \quad (3.7c)$$

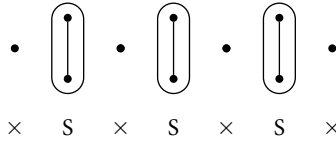


Figure 3.5: Ground states of the symmetric diamond chain for $\gamma < 1$

and an energy constraint of

$$E \geq E_{\min} \geq \min_j - \left(\frac{3}{4} + \frac{\gamma-1}{2} (\vec{S}_{3j+1} + \vec{S}_{3j+2})^2 \right) \frac{N}{3} J \quad (3.8a)$$

$$= \frac{N}{3} J \begin{cases} -\frac{3}{4} & , \gamma < 1 \\ -\gamma + \frac{1}{4} & , \gamma > 1 \end{cases} \quad (3.8b)$$

Apparently, the conditions necessary to minimize these terms are different for $\gamma < 1$ and $\gamma > 1$. The discussion of $\gamma < 1$ follows below whereas $\gamma > 1$ is postponed to the following section.

For $\gamma < 1$, the spin operators \vec{S}_{3j+1} and \vec{S}_{3j+2} have a higher weight than $\gamma \vec{S}_{3j}$ (and $\gamma \vec{S}_{3j+3}$), leading to the ansatz of minimizing their sum $\vec{S}_{3j+1} + \vec{S}_{3j+2}$ as singlet. The energy of this system can be easily calculated by using the results from the symmetric tetramer (Table 3.1) as

$$E_{\text{singlets}} = -\frac{3}{4} J \frac{N}{3} = E_{\min}. \quad (3.9)$$

Thus, the configuration with singlets on the strongly coupled bonds and free spins in between (Fig. 3.5) has minimal energy and must be a $2^{\frac{N}{3}}$ -fold degenerate ground state.

Tetramer-dimerized regime

The dimerized phase of the diamond chain, which sometimes is called tetramer-dimerized phase, has fundamentally different properties than the spin fluid regime, which — for the symmetric chain with arbitrary $J_1 = J_3 > J_2$ — can be already seen from the different ground states. From eq. (3.7) the lower bound of energy for $\gamma > 1$ is obtained as

$$E \geq E_{\min} = -\frac{N}{3} J \left(\gamma - \frac{1}{4} \right) \quad (3.10)$$

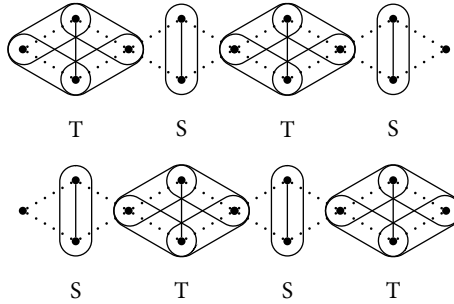


Figure 3.6: Ground states of the symmetric diamond chain in the tetramer-dimerized phase ($\gamma > 1$) and $\frac{N}{3}$ even

implying triplets on J_2 bonds.

The results for the symmetric tetramer (Table 3.1) show that this minimum energy corresponds to a configuration with triplets on both $\vec{S}_{3j+1} + \vec{S}_{3j+2}$ and $\vec{S}_{3j+0} + \vec{S}_{3j+3}$ and a total spin of 0 per tetramer. However, a diamond chain state consisting solely of such triplet/triplet tetramers does not exist because a triplet/triplet tetramer must be neighbored by a singlet dimer, because otherwise the two neighbouring triplet/triplet tetramers would have to share one common spin which must not happen. Therefore, it is necessary that a singlet tetramer — the second lowest configuration in terms of energy for $1 < \gamma < 2$ — lies between two triplet/triplet tetramers. If $\frac{N}{3}$ is even, this leads to a ground state energy of

$$E_0 = -\frac{N}{3}J\left(\frac{\gamma}{2} + \frac{1}{4}\right) \quad (3.11)$$

and two degenerate ground states depicted in Fig. 3.6. These two degenerate ground states are exact for arbitrary γ within the range $1 < \gamma < 2$, *i. e.*, $\frac{1}{2} < J_1 = J_3 < J$ and any finite N with N_3 even. They were shown to be the exact ground states in [20] using the classification of states in terms of the conserved spin of J_2 bonds.

Ferrimagnetic regime

For completeness, I mention the existence of a ferrimagnetic phase at higher values of J_1, J_3 . However, I will not delve into more detail here, because I will not consider this phase in the following discussion. A thorough description of this phase can be found in [20].

3.2 Excitations in the spin fluid regime

In this section I want to discuss the properties of the diamond type chain in the spin fluid regime (*cf.* Fig. 3.4). Since the Hamilton operator eq. (3.1) is symmetric in J_1 and J_3 it is possible to restrict the discussion to $J_1 \geq J_3$ without loss of generality.

The general structure for $J_1, J_3 \ll J_2 = J = 1$ is a sequence of dimers (intra-dimer coupling J_2) with weakly interacting spins in between. The limiting cases on the $J_3 = 0$ axis are already known as

- (a) $J_1 = 0$: free dimers
- (b) $0 < J_1 < 1$: trimer chain
- (c) $J_1 = 1$: Heisenberg antiferromagnetic chain

For $J_1, J_3 \ll J$ this system has two different energy scales: excitations of the nearly free spins can be obtained with much less energy cost than excitations of the singlet dimers to triplets. Hence, the diamond type chain features a low energetic subsystem, which is very similar to a Heisenberg antiferromagnetic chain with $N/3$ spins and an effective coupling $J_{\text{eff}} \sim O(J_1, J_3)$.

The highest state of the Heisenberg antiferromagnetic subsystem has got a total spin of $S_{\text{tot}} = \frac{1}{2} \frac{N}{3} =: M_{\text{plateau}}$ and corresponds to full magnetization of the Heisenberg antiferromagnetic subsystem. This state also forms a magnetization plateau because the next higher energy level involves the excitation of a dimer which is very costly (of the order $O(J_2)$) in the spin-fluid phase.

3.2.1 Effective Heisenberg model

As long as the Hamilton operator is exactly symmetric, *i. e.*, $J_1 = J_3$, the spins between the singlet dimers are absolutely free. For small deviations from the symmetry line, these single spins are weakly coupled and one can expect that these spins, and thus the low lying excitations, can effectively be described by a Heisenberg antiferromagnetic chain. The effective coupling of the corresponding Heisenberg chain

Table 3.3: Comparison between an 18 spin diamond chain with $J_1 = 0.46J$ and $J_3 = 0.44J$ and a six spin Heisenberg antiferromagnetic chain with $J = J_2$

q	S_{tot}	E_6	E_{18}	$\frac{E_{18}}{E_6}$
0	1	0.684742	0.001885	$2.753 \cdot 10^{-3}$
	0	1.302776	0.003502	$2.688 \cdot 10^{-3}$
	1	2.920810	0.007980	$2.732 \cdot 10^{-3}$
	3	4.302776	0.011875	$2.760 \cdot 10^{-3}$
$\frac{\pi}{3}$	1	1.802776	0.004933	$2.736 \cdot 10^{-3}$
	0	2.302776	0.006264	$2.720 \cdot 10^{-3}$
	2	3.802776	0.010447	$2.747 \cdot 10^{-3}$
$\frac{2\pi}{3}$	1	1.521999	0.004144	$2.723 \cdot 10^{-3}$
	2	2.802776	0.007692	$2.744 \cdot 10^{-3}$
	1	3.583552	0.009807	$2.737 \cdot 10^{-3}$
π	0	0.000000	0.000000	—
	2	2.302776	0.006360	$2.762 \cdot 10^{-3}$
	1	3.302776	0.009018	$2.731 \cdot 10^{-3}$
	0	3.605551	0.009860	$2.735 \cdot 10^{-3}$

can be calculated in perturbation theory. Singlet-triplet splitting in the spin-fluid phase yields [26]

$$2J_{\text{eff}} = \sqrt{(J_1 + J_3 - 1)^2 + 3(J_1 - J_3)^2} - \left(1 - (J_1 + J_3)\right) + 1 - \sqrt{1 + (J_1 - J_3)^2}. \quad (3.12)$$

The comparison between an eighteen spin diamond chain with $J_1 = 0.46J$ and $J_3 = 0.44J$ and a six spin Heisenberg antiferromagnetic chain in Table 3.3 shows that the coupling of the single spins is very weak, about $\frac{1}{365}$ of the ordinary Heisenberg chain, but the spectrum fits a Heisenberg antiferromagnet. This behaviour can also be seen for $J_1 = 0.60J$, $J_3 = 0.05J$ (Table 3.4) as well as $J_1 = 0.60J$, $J_3 = 0.32J$ (Table 3.5), although the latter is a far less perfect Heisenberg antiferromagnet, which is manifest in other states (coming from excitation of the dimers) intermixing with the states corresponding to the Heisenberg antiferromagnet. The beginning of the plateau is $H_{c1} = 2J_{\text{eff}}$, and with increasing J_1 , J_{eff} approaches $(\gamma - 1)J_1 = 2J_1 - J_2$,

Table 3.4: Comparison between an 18 spin diamond chain with $J_1 = 0.60J$ and $J_3 = 0.05J$ and a six spin Heisenberg antiferromagnetic chain with $J = J_2$

q	S_{tot}	E_6	E_{18}	$\frac{E_{18}}{E_6}$
0	1	0.684742	0.136688	0.199620
	0	1.302776	0.225476	0.173074
	1	2.920810	0.615239	0.210640
	3	4.302776	0.952216	0.221303
$\frac{\pi}{3}$	1	1.802776	0.379594	0.210561
	0	2.302776	0.465613	0.202196
	2	3.802776	0.818614	0.215267
$\frac{2\pi}{3}$	1	1.521999	0.300416	0.197382
	2	2.802776	0.599532	0.213906
	1	3.583552	0.742337	0.207151
π	0	0.000000	0.000000	—
	2	2.302776	0.492288	0.213870
	1	3.302776	0.667391	0.202070
	0	3.605551	0.734454	0.203701

the plateau field on the line $J_1 = J_3$.

For the quality of the approximation and the effective coupling strength of the Heisenberg model, two rules of thumb can be put up:

- (1) Approaching the phase boundary reduces the quality of the approximation; and
- (2) approaching the diagonal $J_1 = J_3$ increases the quality of the approximation and reduces the effective coupling strength.

On the other side of the phase transition, a connection between diamond chain and Heisenberg chain cannot be drawn, neither by energy levels nor by quantum numbers.

Table 3.5: Comparison between an 18 spin diamond chain with $J_1 = 0.60J$ and $J_3 = 0.32J$ and a six spin Heisenberg antiferromagnetic chain with $J = J_2$. Other low lying excitations are mixed with the listed ones.

q	S_{tot}	E_6	E_{18}	$\frac{E_{18}}{E_6}$
0	1	0.684742	0.097656	0.142617
	0	1.302776	0.115000	0.088273
	1	2.920810	0.399308	0.136712
	3	4.302776	0.668133	0.155280
$\frac{\pi}{3}$	1	1.802776	0.250341	0.138864
	0	2.302776	0.285469	0.123967
	2	3.802776	0.546597	0.143736
$\frac{2\pi}{3}$	1	1.521999	0.192341	0.126374
	2	2.802776	0.408072	0.145596
	1	3.583552	0.457526	0.127674
π	0	0.000000	0.000000	—
	2	2.302776	0.351742	0.152747
	1	3.302776	0.401453	0.121550
	0	3.605551	0.424617	0.117768

Table 3.6: Effective Heisenberg coupling: comparison of the numerical results of the $N = 18$ diamond chain and the analytical result of non-interacting tetramers. The effective coupling has been obtained by averaging over the individual states. Daggers † denote cases where the effective Heisenberg model is not the lowest subset but intermixed with other states.

J_1	J_3	diamond chain	non-interacting tetramers
0.46	0.44	$2.736 \cdot 10^{-3}$	$2.815 \cdot 10^{-3}$
0.48	0.46	$4.230 \cdot 10^{-3}$	$4.541 \cdot 10^{-3}$
0.50	0.48	$7.713 \cdot 10^{-3}$	$9.900 \cdot 10^{-3}$
0.60	0.05	0.205	0.262
0.60	0.25	0.154	0.208
0.60	0.32	†0.132	0.187
0.10	0.05	$1.573 \cdot 10^{-3}$	$1.576 \cdot 10^{-3}$

3.3 Excitations in the tetramer-dimerized regime

In order to access the low lying excitations of the diamond chain in the tetramer-dimerized phase, it is instructive to review the results of the single, symmetric tetramer (Table 3.1). The excitation of a singlet tetramer to a singlet dimer and two nearly free spins requires an energy of $\Delta E = 2J_1 - J_2 = (\gamma - 1)J_2$, whereas all other excitations cost at least $\Delta E = \frac{\gamma}{2}J_2$ and therefore are less favourable.

Transferring this result to the diamond chain, this lowest excitation can occur at any of the $N/3$ cells and produces a pair of neighbouring domain walls, which can propagate freely (apart from interactions between themselves) as solitons along the chain and lead to a band of two soliton excitations. However, they are not the only low lying excitations. Since the energy of the state does not depend on the position of any of the two domain walls, they may well be separated and are still degenerate with the paired domain walls excitations. This degeneracy can be lifted by breaking the symmetry and going to the distorted diamond chain.

Since these two solitons cannot move freely along a diamond chain of 18 spins, *i. e.*, six cells, because they constantly interact with one another, and computational resources prevent me from exact diagonalization of larger diamond chains, I will investigate the soliton propagation in a 15 spin diamond chain. On the first glance it might seem contradictory to choose a smaller system when the larger system is not large enough, but the ground states of a diamond chain with an odd number of cells involve exactly one soliton, and thus, it is possible to examine free propagation of a single soliton.

In the vicinity of the symmetry line $J_1 = J_3$, the interaction along the chain axis, *i. e.*, between the tetramer and dimer cells, is small (of the order $J_1 - J_3$). Since this is the responsible coupling for domain wall hopping, it is possible to employ a tight

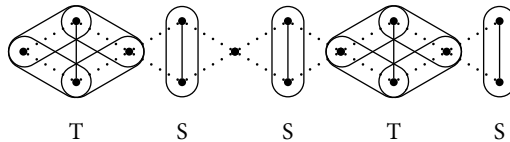


Figure 3.7: Ground states of the symmetric diamond chain in the tetramer-dimerized phase ($\gamma > 1$) and $\frac{N}{3}$ odd

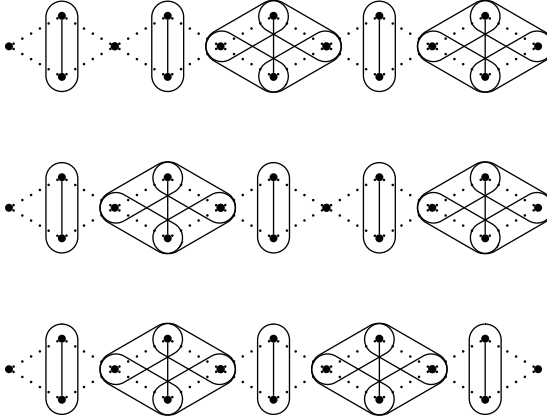


Figure 3.8: Domain wall movement in the diamond chain. The domain wall always moves by two cells. For $N = 15$ spins, the depicted states are three out of five states.

binding calculation with the tight binding Hamiltonian

$$\mathcal{H} = \sum_{j=0}^{\frac{N}{3}-1} E_0 |j\rangle \langle j| + t (|j\rangle \langle j+2| + |j\rangle \langle j-2|) \quad (3.13)$$

The energy E_0 is the energy of a localized soliton, *i. e.*, the energy difference between $S \times S \times$ and ST , and is constant for all degenerate states $|j\rangle$, t is the amplitude for a $\times ST \leftrightarrow TS \times$ transition, *i. e.*, for domain wall hopping, and the state $|j\rangle$ denotes the state where the domain wall (two neighbouring dimers) sits around the free spin at $3j$, *i. e.*, the dimers are at spins $(3j - 2, 3j - 1)$ and $(3j + 1, 3j + 2)$. As can be seen from Fig. 3.8 the domain walls always move by two cells, which is accounted for in this Hamiltonian.

In order to implement the translational symmetry of the diamond chain, it is

meaningful to use the Fourier transform of $|j\rangle$

$$|k\rangle = \sum_{\ell=0}^{\frac{N}{3}-1} e^{ik\ell} |\ell\rangle \quad (3.14)$$

A standard calculation then leads to the momentum dependent energy eigenvalues

$$\mathcal{H}|k\rangle = (E_0 + 2t \cos(2k))|k\rangle \quad (3.15)$$

Up to here, it is only a projection of the expected behaviour of the low lying excitations, so now it is time to compare the numerical results to this projection. In order to find the values of E_0 and t for a given set of data, it is necessary to fit the data against the above cosine by minimizing the sum of the error squares

$$\chi^2(E_0, t) = \sum_j (E_0 + 2t \cos(2k_j) - E_j)^2 \quad (3.16)$$

where the summation runs over the supporting points, *i. e.*, the numerical data points. This minimum can be found analytically by solving the condition

$$0 = \left(\frac{\partial}{\partial E_0} \right) \chi^2(E_0, t) \quad (3.17a)$$

$$= \sum_j \left(\frac{1}{2 \cos(2k_j)} \right) (E_0 + 2t \cos(2k_j) - E_j) \quad (3.17b)$$

and yields the parameters

$$E_0 = \frac{\sum_j E_j - 2t \sum_j \cos(2k_j)}{\sum_j 1} \quad (3.18a)$$

$$t = \frac{\sum_j 1 \sum_j E_j \cos(2k_j) - \sum_j E_j \sum_j \cos(2k_j)}{\sum_j 1 \sum_j \cos^2(2k_j) - (\sum_j \cos(2k_j))^2} \quad (3.18b)$$

Table 3.3 shows the fit parameters E_0 and t for various values of J_1 and J_3 . The last column $\sqrt{\chi^2}$, *cf.* eq. (3.16), gives a rough idea of the accuracy of the soliton description.

Table 3.7: Fit of the numerical results of an $N = 15$ distorted diamond chain in the tetramer-dimer phase to the tight binding model. All data are measured in units of $J_2 = J$.

J_1	J_3	E_0	t	$\sqrt{\chi^2}$
0.52	0.50	0.016507	$3.88319 \cdot 10^{-3}$	0.002671
0.54	0.52	0.032211	$2.45365 \cdot 10^{-3}$	0.000322
0.60	0.38	0.151488	$51.01065 \cdot 10^{-3}$	0.111193
0.60	0.44	0.114076	$38.03195 \cdot 10^{-3}$	0.062962
0.60	0.55	0.078095	$7.55368 \cdot 10^{-3}$	0.000905

The next meaningful step would be to look at the addition of two independent solitons with momenta k_1 and k_2

$$E(k_1, k_2) = (E_0 + 2t \cos(2k_1)) + (E_0 + 2t \cos(2k_2)) \quad (3.19a)$$

$$= 2E_0 + 4t \cos(k_1 + k_2) \cos(k_1 - k_2) \quad (3.19b)$$

In a diamond chain of 18 spins, however, the domain walls are bound and cannot move freely. Therefore, the discussion of two soliton movement has to be postponed to later computations with diamond chains of length 24.

3.4 Specific heat

In this section I will consider a regime covering both spin-fluid and tetramer-dimerized phases, including the phase transition between them, but ignoring the ferrimagnetic phase at larger J_1, J_3 . Currently, I will examine the phase transition only by means of the specific heat, detailed dynamics involving the dynamic structure factors have to be postponed to a later work.

This phase transition is conveniently considered along a line with constant J_1 and varying J_3 and is of KOSTERLITZ-THOULESS/sine-GORDON type, because what occurs is of the same symmetry as in the Heisenberg antiferromagnetic chain with next nearest neighbour interaction J_{NNN} , which changes from the spin fluid to the dimerized phase at $J_{\text{NNN}} = 0.2411J_{\text{NN}}$. OKAMOTO and NOMURA have presented an approach to determine the transition strength when only finite systems are available.[27] In the spin fluid phase, the triplet state has got a lower energy, whereas in the tetramer-dimerized phase, the singlet has got a lower energy. At the phase transition, the ground states of both phases unite to a ground state with higher degeneracy. With this behaviour in mind, OKAMOTO and NOMURA plot the energies of both the lowest excited triplet and the lowest excited singlet vs. J_3 and localize the intersection point, which marks the phase transition.

In fact the lowest excited singlet state is the singlet which becomes the other degenerate ground state in the tetramer-dimerized phase, *i. e.*, in an infinite system it should reach zero energy immediately at the phase transition. For finite systems, however, this transition to zero energy is gradual, but the intersection with the triplet energy can localize the phase transition.

Employing this algorithm, the phase transition for $N = 24$ and $J_1 = 0.6J$ is found at $J_3 = 0.364J$ [26]. In this place I will discuss how the phase transition is reflected in the specific heat. Figs. 3.9 to ?? demonstrate the following behaviour.

Fig. 3.9 depicts the dependence of the specific heat on the variation of J_3 through the phase transition at $J_1 = 0.60J$ and zero magnetic field. In the vicinity of the phase transition ($\approx \pm 0.10J$) the curves look very similar to each other with a “plateau-like” structure around $T \approx 0.07J$. Far away from the phase transition, the specific heat curves look distinct, with a slower slope in the spin-fluid phase and a second peak at $T \approx 0.05J$ in the tetramer-dimerized phase.

The low temperature behaviour can be better observed from Fig. 3.10, which clearly shows a gap in the excitation spectrum far away from the phase transition ($J_3 = 0.05$ and $J_3 = 0.55$). Closer to the phase transition, it becomes more difficult to tell apart whether the gap is an intrinsic property of the system or simply attributed to the discreteness of a finite system, but it is likely that at least the two sets in the tetramer-dimerized phase ($J_3 = 0.38$ and $J_3 = 0.44$) are gapless as is known from the effective Heisenberg antiferromagnet.

Figs. 3.11 to 3.17 show the variation of the specific heat with the magnetic field at $J_1 = 0.60J$ for several J_3 in both phases. The most striking feature is a double peak or almost double peak structure at magnetic field below or above the magnetization plateau whereas only a single peak can be observed within the magnetization plateau. With respect to temperature, this single peak is located between the double peaks.

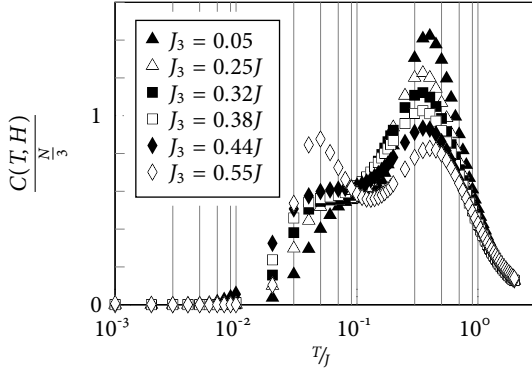


Figure 3.9: Specific heat of the $N = 18$ diamond chain with $J_1 = 0.60J$ and $H = 0$ vs. T

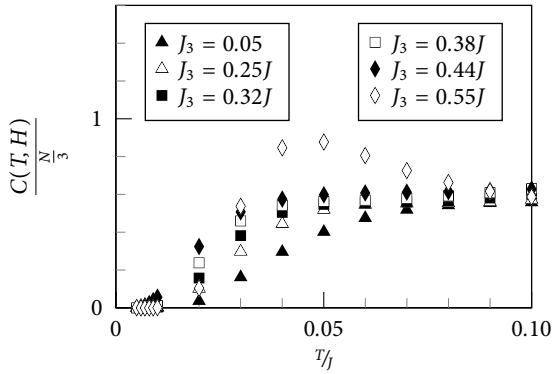


Figure 3.10: Specific heat of the $N = 18$ diamond chain with $J_1 = 0.60J$ and $H = 0$ vs. T

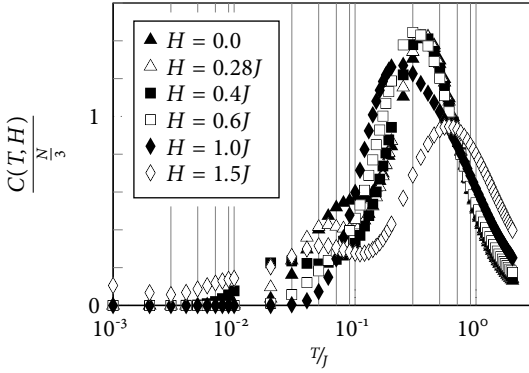


Figure 3.11: Specific heat of the $N = 18$ diamond chain with $J_1 = 0.60J$ and $J_3 = 0.05J$ vs. T . The magnetization plateau ranges from $H_{c,1} = 0.460J$ to $H_{c,2} = 1.267J$.

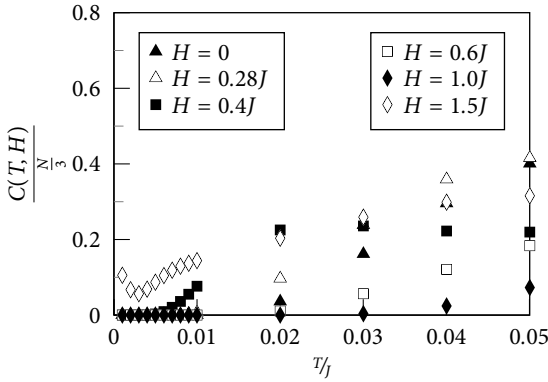


Figure 3.12: Specific heat of the $N = 18$ diamond chain with $J_1 = 0.60J$ and $J_3 = 0.05J$ vs. T

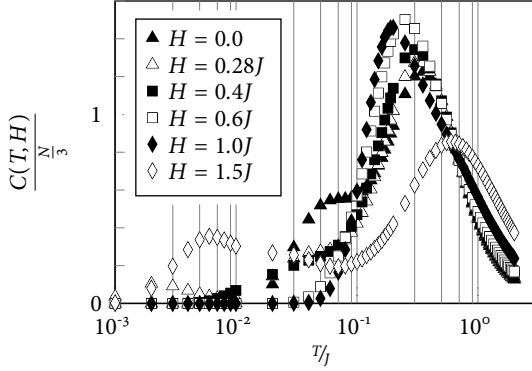


Figure 3.13: Specific heat of the $N = 18$ diamond chain with $J_1 = 0.60J$ and $J_3 = 0.25J$ vs. T

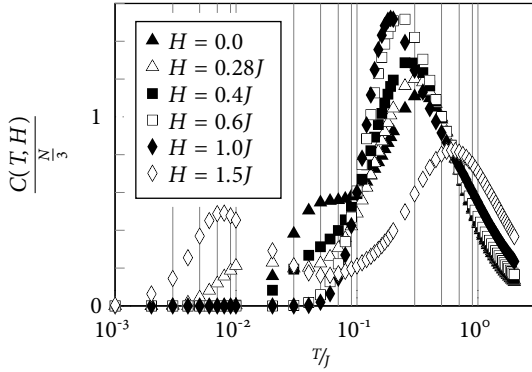


Figure 3.14: Specific heat of the $N = 18$ diamond chain with $J_1 = 0.60J$ and $J_3 = 0.32J$ vs. T . The magnetization plateau ranges from $H_{c,1} = 0.316J$ to $H_{c,2} = 1.412J$.

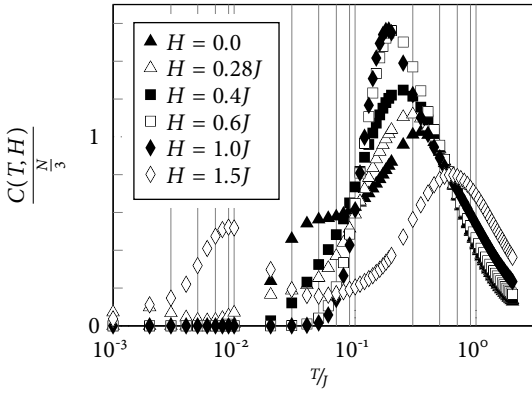


Figure 3.15: Specific heat of the $N = 18$ diamond chain with $J_1 = 0.60J$ and $J_3 = 0.38J$ vs. T . The magnetization plateau ranges from $H_{c,1} = 0.276J$ to $H_{c,2} = 1.448J$.

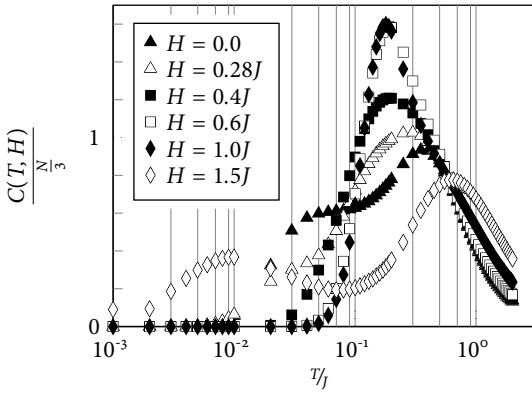


Figure 3.16: Specific heat of the $N = 18$ diamond chain with $J_1 = 0.60J$ and $J_3 = 0.44J$ vs. T .

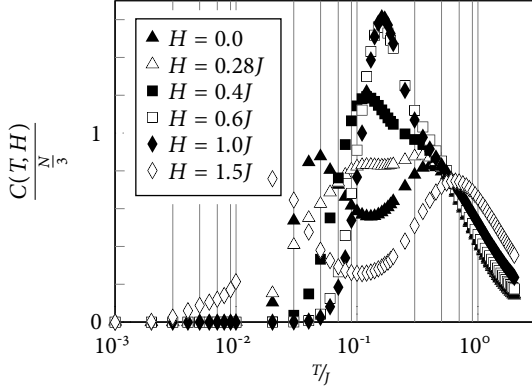


Figure 3.17: Specific heat of the $N = 18$ diamond chain with $J_1 = 0.60J$ and $J_3 = 0.55J$ vs. T

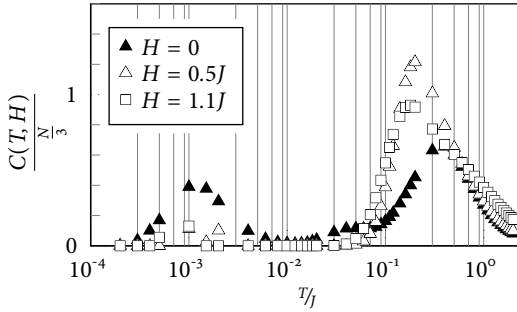


Figure 3.18: Specific heat of the $N = 18$ diamond chain with $J_1 = 0.46$ and $J_3 = 0.44$ vs. T

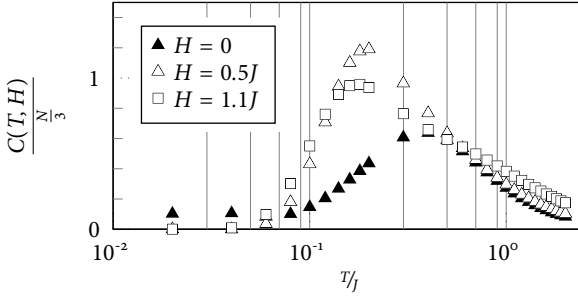


Figure 3.19: Specific heat of the $N = 18$ diamond chain with $J_1 = 0.48$ and $J_3 = 0.46$ vs. T

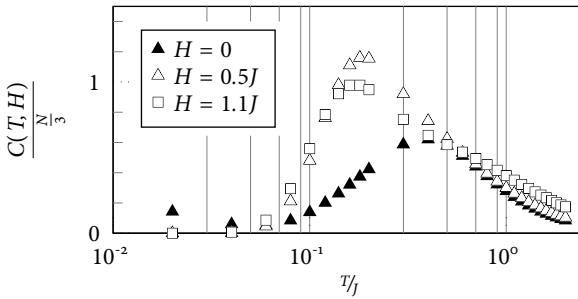


Figure 3.20: Specific heat of the $N = 18$ diamond chain with $J_1 = 0.50$ and $J_3 = 0.48$ vs. T

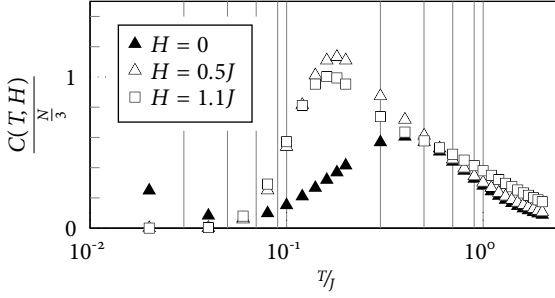


Figure 3.21: Specific heat of the $N = 18$ diamond chain with $J_1 = 0.52$ and $J_3 = 0.50$ vs. T

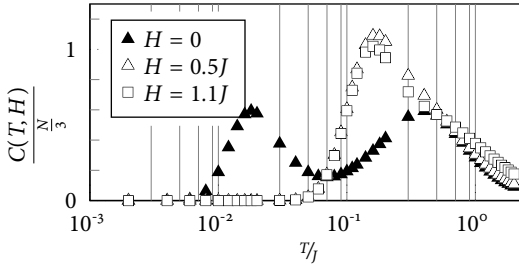


Figure 3.22: Specific heat of the $N = 18$ diamond chain with $J_1 = 0.54$ and $J_3 = 0.52$ vs. T

CHAPTER 4

Conclusion

In this work I have presented finite temperature dynamics of two different quantum spin systems based on full exact diagonalization. With this approach I was able to obtain results for the complete temperature range from $T \rightarrow 0$ up to $T \gg J$.

The first system I discussed was the bond alternating Heisenberg chain (Chapter 2) where I presented finite temperature results of the dynamic structure factor for up to 20 spins $\frac{1}{2}$. This small system size, however, limited the strength of the inter-dimer coupling $\lambda \lesssim 0.3$. At such small values of the inter-dimer coupling, the characteristics of the bond alternating chain is qualitatively similar to non-interacting dimers, and becomes evident in the existence of the central (zero frequency) peak and in the temperature and wave vector dependence of the exclusive structure factor, *i. e.*, the integrated intensities, for both the central and the one-magnon peak. In addition to the dynamic structure factor, I discussed the specific heat for several values of the coupling constant and magnetic fields.

Experimental and theoretical interest in the dynamics of the bond alternating Heisenberg chain results from the possibility that this theoretical model and its realizations in a number of materials, *e. g.*, Copper nitrate $\text{Cu}(\text{NO}_3)_2$, might serve as a simple model system to discuss the interplay between temperature and quantum fluctuations. The results reveal that this interplay becomes apparent in a number of points which are accessible to experimental, in particular neutron scattering, observations:

- (i) The shape of the central peak of the longitudinal structure factor, which is a prominent feature of the bond alternating chain, displays the crossover with

temperature from the non-interacting particle like behaviour at low temperatures to the shape at high temperatures which appears similar to diffusive behaviour. Changes of the magnetization have only little influence on the shape of the central peak.

- (ii) The one magnon peak develops an asymmetric line width (with appreciable strength on the high frequency side) with temperature. This is particularly evident for wave vector $q = 2\pi$ at temperatures $T \geq J$ and appears to describe in more detail the upward shift in gap energy with temperature noted in approximate theoretical approaches. This asymmetry as well as the strength of the one-magnon peak depends on the magnetization of the system.
- (iii) The two magnon peak (around $q = \pi$) is dominated by the bound triplet state on top of a small continuum which is smooth at all temperatures and wave vectors.

The introduction of an external magnetic field breaks isotropy and offers another quantity to be examined: at finite field, the transverse structure factor is subject to Zeeman splitting and involves different transitions than the longitudinal structure factor.

- (i) The transverse structure factor shows a strong one-magnon peak at all momenta, all temperatures, and all magnetizations. At higher temperatures, an asymmetry with emphasis on the high frequency side for $q = \pi$ and emphasis on the low frequency side for $q = 2\pi$ develops.
- (ii) The central peak of the transverse structure factor is heavily suppressed for $q = 2\pi$, which can be understood with the momentum dependence in the non-interacting dimer limit.
- (iii) At $q = 2\pi$ the transverse structure factor features a very strong peak at $\omega \approx 0$, which can be regarded as inverse one-magnon transitions. It sets in close to the critical field and is present even at low temperatures, where its main contribution comes from a strong dipole transition between the ground states of magnetization M and $M - 1$.

The other system I investigated was the distorted diamond chain (Chapter 3). Here I was able to give results for the specific heat for up to 18 spins $\frac{1}{2}$. I was able to qualitatively understand the behaviour of the diamond chain with the help of the fundamental building block, the generic and the distorted tetramer. Detailed quantitative behaviour, however, had to be postponed to a later work.

In the spin-fluid phase, I compared the low energetic spectrum of the diamond chain with the spectrum of a Heisenberg antiferromagnetic chain of $\frac{N}{3}$ spins. In

the same manner, I compared the low energetic spectrum in the tetramer-dimerized phase with the spin $\frac{1}{2}$ magnon of the Heisenberg antiferromagnetic chain of $\frac{N}{3}$ (N odd, $N = 15$) spins.

Since the behaviour at the phase transition between the spin-fluid and the tetramer-dimerized phases is of most interest, I concentrated on two paths in the phase diagram, the first having constant $J_1 = 0.6J$ (more or less close to azurite), and the other one parallel to the diagonal with $J_1 - J_3 = 0.2J$.

In the spin-fluid phase, the distorted diamond chain shows two energy scales:

- (a) Excitations of the single spins at a low energy scale behave like an effective Heisenberg model with $J_{\text{eff}} \ll J$. Especially at low values of J_1 and J_3 , *i. e.* far away from the phase boundary, and close to the symmetry line $J_1 = J_3$, the quality of the effective Heisenberg was very good. The effective coupling constant grows with increasing distance from the symmetry line.
- (b) Excitations of the dimers are at a much larger energy scale ($E \gtrsim J$). However, approaching the phase boundary reduces the difference between the two energy scales until they intermix.

In the tetramer-dimerized phase, the soliton propagation of domain walls is the most interesting feature. Unfortunately, the limited system size confined my investigation to single solitons; two freely moving solitons will only be observed with larger system sizes than I could investigate within the scope of this work.

The examination of the two-soliton excitations surely is an interesting but not the only task for a future work. Of great importance is also the determination of the detailed dynamics of the distorted diamond chain by investigating the dynamic structure factor.

On behalf of the bond alternating Heisenberg chain, the future expansion to larger system sizes will allow for larger values of the coupling ratio λ like they are expected in $(\text{VO})_2\text{P}_2\text{O}_7$.

Appendix

APPENDIX A

The Numerical Approach

There are a vast number of different numerical methods available to investigate the properties of spin systems, ranging from purely statistical approximations for largest systems and DMRG for considerably large systems down to exact diagonalization being the most accurate method. Nevertheless, it is also most demanding and heavily restricts the system size. In a run for new physics in more and more complex systems modelled after real-life complex compounds, people tend to prefer inexact over exact methods.

In this work, I will restrict myself to full exact diagonalization of spin- $\frac{1}{2}$ systems — and thus limiting the system size to 20 spins at most. In order to be able to handle systems of such size¹, I took several symmetries into account.

First, I limit myself to systems with fixed total spin projection S_z^{tot} , reducing the matrix dimension from 2^N to $\binom{N}{\frac{N}{2} + S_z^{\text{tot}}}$ for an N -spin system, but increasing the number of diagonalizations by a factor N . While this saving in memory is mandatory to calculate reasonable system sizes, I will not be able to describe all physical processes with this model, *e. g.*, single-spin-umklapp processes change the total spin projection.

Second, the investigated Hamilton operators are translationally invariant — with respect to the intrinsic periodicity P , $J_{a,i} = J_{a,i+P}$. Technically speaking, the Hamilton and translation operator commute $[\mathcal{H}, T] = 0$, which enables me to find a set

1. Remember that $2^{20} \approx 10^6$, *i. e.*, the matrix size of the Hamiltonian is $10^6 \cdot 10^6 = 10^{12}$. Using double precision complex numbers, this yields 16 Bytes per matrix element or about 16 PB for the whole matrix

of simultaneous eigenstates

$$|i, q\rangle = \sqrt{\frac{p}{N}} \sum_{n=0}^{\frac{N}{p}-1} e^{iqn} T^n |a\rangle \quad (\text{A.1})$$

where i labels the set of translationally invariant spin configurations, a is one representing spin configuration of that class, and $q = n 2\pi \frac{N}{p}$, $n = 0, \dots, \frac{N}{p} - 1$ is the wave ‘vector’. Incorporating the wave vector as conserved quantity or ‘quantum number’, I can reduce the matrix size by a factor of $\frac{N}{p}$. Strictly speaking, the reduction is slightly less because certain spin configurations already show a higher symmetry.

Generally speaking, I could increase the size of the elementary cell to an arbitrary value in order to model a system with arbitrary, or even no symmetry, but I will consider only systems with an elementary cell of size three or smaller, because otherwise the matrix grows too large for reasonable system sizes.

An external magnetic field only enters the Hamiltonian by means of a Zeeman shift. Since I require the magnetic field to be constant in time and space, the Zeeman term is constant and diagonal and, thus, does not influence the wave functions but only the energies of the eigenstates. This is important to note, because it reduces the diagonalization computations to zero field diagonalization and heavily reduces the amount of computations for the dynamical structure factors.

After evaluating all symmetries for a given system, and taking all spin interactions into account, I arrive at a matrix corresponding to the Hamiltonian, whose reduction to eigenvalues and -states is the topic of the next section A.1. Section A.2 covers the computation of the dynamic structure factors, and Section A.3 gives a very short overview of the calculation of the specific heat.

A.1 Diagonalization

After having made the decision of employing full exact diagonalization, the algorithm to be used had to be chosen. One particularly efficient algorithm for full exact diagonalization is the concatenation of the HOUSEHOLDER and the QR algorithms, which I will present here in a short overview.[28]

The HOUSEHOLDER algorithm reduces a hermitean matrix $H = H_i$ to a hermitean tridiagonal matrix H_{n-1} by $n - 2$ orthogonal transformations, where n is the dimension of the matrix. These transformations follow

$$H_{i+1} = M_i H_i M_i, \quad i = 1, 2, \dots, n - 2 \quad (\text{A.2})$$

where

$$M_i = 1 - \frac{a_i a_i^\dagger}{t_i} \quad (\text{A.3a})$$

$$t_i = \frac{1}{2} a_i^\dagger a_i \quad (\text{A.3b})$$

$$a_i = (h_{\ell,1}^{(i)}, \dots, h_{\ell,\ell-2}^{(i)}, h_{\ell,\ell-1}^{(i)} \pm \sigma_i^{\frac{1}{2}}, 0, \dots, 0)^\dagger \quad (\text{A.3c})$$

$$\ell = n - i + 1 \quad (\text{A.3d})$$

$$\sigma_i = (h_{\ell,1}^{(i)})^2 + \dots + (h_{\ell,\ell-1}^{(i)})^2 \quad (\text{A.3e})$$

$$p_i = \frac{H_i a_i}{t_i} \quad (\text{A.3f})$$

$$k_i = \frac{a_i^\dagger p_i}{2t_i} \quad (\text{A.3g})$$

$$q_i = p_i - k_i a_i \quad (\text{A.3h})$$

resulting in

$$H_{i+1} = \left(1 - \frac{a_i a_i^\dagger}{t_i}\right) A_i \left(1 - \frac{a_i a_i^\dagger}{H_i}\right) \quad (\text{A.4a})$$

$$= H_i - a_i q_i^\dagger - q_i a_i^\dagger \quad (\text{A.4b})$$

The matrix H_i is tridiagonal in its last $i - 1$ rows and columns, hence H_{n-1} is a tridiagonal matrix. Furthermore, if \vec{v} is an eigenvector of the tridiagonal matrix H_{n-1} then $M_1 \dots M_{n-2}$ is an eigenvector of H .

Finally, the obtained tridiagonal matrix can be transformed to upper triangular form by a standard QR decomposition, which is particularly efficient on tridiagonal matrices. Albeit the resulting matrix is not strictly speaking diagonal, the eigenvalues can be read off and the eigenstates can be obtained by a small calculation.

On the JUMP supercomputer (an IBM Regatta), however, it turned out that IBM's highly optimized, threaded ESSL library was more efficient so that I opted for it for the production runs on that computer.

A.2 Dynamic structure factor

After having completed the diagonalization, the obtained eigenstates are used to compute the dynamic structure factor $S(q, \omega)$ from the single matrix elements of

the spin operators.

$$S^{\sigma\sigma}(q, \omega) = \frac{1}{N} \sum_{i,f} e^{-\frac{\beta E_i}{k_B T}} \left| \langle f | S^\sigma(q) | i \rangle \right|^2 \delta(E_f - E_i - \omega) \quad (\text{A.5a})$$

$$S^\sigma(q) = \sum_n e^{iqn} S_n^\sigma \quad (\text{A.5b})$$

where i, f loop over all eigenstates, n over all spins, and $\sigma = z, \pm$. Remembering translational invariance

$$|i\rangle = \sum_a c_a \left(\sqrt{\frac{P_a}{N}} \sum_{j=0}^{\frac{N}{P_a}-1} e^{ikj} T^j |a\rangle \right), \quad (\text{A.6})$$

I find

$$\langle f | S_n^\sigma | i \rangle = \sum_{a,b} c_b^* c_a \frac{\sqrt{P_a P_b}}{N} \sum_{j=0}^{\frac{N}{P_a}-1} \sum_{j'=0}^{\frac{N}{P_b}-1} e^{i(kj-k'j')} \langle b | T^{-j'} S_n^\sigma T^j | a \rangle \quad (\text{A.7a})$$

$$= \sum_{a,b} c_b^* c_a \frac{\sqrt{P_a P_b}}{N} \sum_{j=0}^{\frac{N}{P_a}-1} \sum_{j'=0}^{\frac{N}{P_b}-1} e^{i(kj-k'j')} \langle b | T^{j-j'} S_{n-j}^\sigma | a \rangle \quad (\text{A.7b})$$

It is noteworthy, that this matrix element does not depend on the energies of the participating states but only on their wave functions and is therefore independent of an applied magnetic field and temperature.

As S^z (opposed to S^\pm) is diagonal, this can be further simplified for S^z :

$$\langle f | S_n^z | i \rangle = \sum_a c_a^{f*} c_a^i \sum_{j=0}^{\frac{N}{P_a}-1} e^{i(k-k')j} \langle a | S_{n-j}^z | a \rangle \quad (\text{A.8a})$$

$$= e^{i(k-k')n} \sum_a |c_a^i|^2 \sum_{j=0}^{\frac{N}{P_a}-1} e^{-i(k-k')j} \langle a | S_j^z | a \rangle \quad (\text{A.8b})$$

leading to

$$\langle f|S^z(q)|i\rangle = \sum_{n=0}^{N-1} e^{i(q-k+k')n} \sum_a |c_a^i|^2 \sum_{j=0}^{\frac{N}{P_a}-1} e^{-i(k-k')j} \langle a|S_j^z|a\rangle \quad (\text{A.9a})$$

$$= \delta(q-k+k') \sum_a |c_a^i|^2 \sum_{j=0}^{\frac{N}{P_a}-1} e^{-iaj} \langle a|S_j^z|a\rangle \quad (\text{A.9b})$$

As expected, the matrix element of S^z is diagonal, which saves a lot of computational effort. Unfortunately, S^\pm are not diagonal, meaning that S^{+-} and S^{-+} cannot be simplified in this way. This leads to the general, but more complex form

$$\langle f|S^+(q)|i\rangle = \sum_{a,b} c_b^{f*} c_a^i \sum_{n=0}^{N-1} \sum_{j=0}^{\frac{N}{P_a}-1} \sum_{j'=0}^{\frac{N}{P_b}-1} e^{i(qn+kj+k'j')} \langle b|T^{j-j'} S_{n-j}^-|a\rangle \quad (\text{A.10a})$$

$$= \delta(k+q-k') \sum_{a,b} c_b^{f*} c_a^i \sqrt{\frac{P_b}{P_a}} \sum_{n=0}^{N-1} \delta_n^a e^{i(qn-k'm(n,a))} \sum_{r=0}^{P_b-1} e^{i\frac{r}{P_b}(2\pi-k'N)} \quad (\text{A.10b})$$

However, it is sufficient to calculate the values for S^{zz} and S^{+-} , because S^{-+} can be obtained from S^{+-} by means of detailed balance. The structure factor is

$$S^{+-}(q, \omega) = \int dt e^{-i\omega t} \langle S^+(q, t) S^-(q, 0) \rangle \quad (\text{A.11a})$$

$$= \sum_{m,n} e^{-\beta E_m} \delta(-\omega + E_m - E_n) \langle m|S^+(q, 0)|n\rangle \langle n|S^-(q, 0)|m\rangle \quad (\text{A.11b})$$

with

$$\langle S^+(q, t) S^-(q, 0) \rangle = \sum_n \langle S^+(q, t)|n\rangle \langle n|S^-(q, 0)\rangle \quad (\text{A.12a})$$

$$= \sum_n \langle e^{i\mathcal{H}t} S^+(q, 0) e^{-i\mathcal{H}t}|n\rangle \langle n|S^-(q, 0)\rangle \quad (\text{A.12b})$$

$$= \sum_{m,n} e^{-\beta E_m} e^{i(E_m - E_n)t} \langle m|S^+(q, 0)|n\rangle \langle n|S^-(q, 0)|m\rangle \quad (\text{A.12c})$$

Analogous

$$\langle S^-(q, t)S^+(q, 0) \rangle = \sum_{m,n} e^{-\beta E_m} e^{i(E_m - E_n)t} \langle m|S^-(q, 0)|n \rangle \langle n|S^+(-q, 0)|m \rangle \quad (\text{A.13a})$$

$$= \sum_{m,n} e^{-\beta E_n} e^{-i(E_m - E_n)t} \langle m|S^+(-q, 0)|n \rangle \langle n|S^-(q, 0)|m \rangle \quad (\text{A.13b})$$

$$= \sum_{m,n} e^{-\beta E_m} e^{-\beta(E_n - E_m)} e^{-i(E_m - E_n)t} \langle m|S^+(-q, 0)|n \rangle \langle n|S^-(q, 0)|m \rangle \quad (\text{A.13c})$$

Combining these equations yields the correspondence between S^{+-} and S^{-+}

$$S^{-+}(q, \omega) = \sum_{m,n} e^{-\beta E_m} e^{-\beta(E_n - E_m)} \delta(\omega + E_m - E_n) \langle m|S^+(-q, 0)|n \rangle \langle n|S^-(q, 0)|m \rangle \quad (\text{A.14a})$$

$$= e^{-\beta\omega} \sum_{m,n} e^{-\beta E_m} \delta(\omega + E_m - E_n) \langle m|S^+(-q, 0)|n \rangle \langle n|S^-(q, 0)|m \rangle \quad (\text{A.14b})$$

$$= e^{-\beta\omega} S^{+-}(-q, -\omega) \quad (\text{A.14c})$$

In the end, the computation of the transverse dynamic structure factor involves a large number of vector-matrix-vector multiplications, which still allow for some optimization.

First, a very small Boltzmann factor will yield a very small matrix element. In this case the matrix multiplication of this matrix element may safely be skipped completely. However, this only helps at low temperatures ($T \lesssim 0.1J$).

Second, the matrix elements share a common subexpression, namely the sum over j and j' in eq. (A.7), which is independent of the wave functions and energies and can be evaluated before the matrix multiplications, reducing the computational effort.

A.3 Specific heat

In contrast to the previous computations, which required both the energy spectrum and the wave functions, the calculation of the specific heat is much less demanding

as it only depends on the energy spectrum. Starting from the thermodynamic expressions (with $k_B \equiv 1$)

$$F = -\frac{1}{\beta} \ln(Z), \quad S = \beta^2 \frac{\partial F}{\partial \beta} \quad (\text{A.15a})$$

$$C = -\beta \frac{\partial S}{\partial \beta} = \beta^2 \frac{\partial^2 \ln(Z)}{\partial \beta^2} \quad (\text{A.15b})$$

I obtain the formula

$$C = \beta^2 \frac{d}{d\beta} \left(\frac{1}{Z} \sum_n e^{-\beta E_n} E_n \right) \quad (\text{A.16a})$$

$$= \frac{1}{\beta^2} \left[\frac{1}{Z} \sum_n E_n^2 e^{-\beta E_n} - \frac{1}{Z^2} \left(\sum_n E_n e^{-\beta E_n} \right)^2 \right] \quad (\text{A.16b})$$

$$= \frac{1}{\beta^2} \langle (E - \langle E \rangle)^2 \rangle \quad (\text{A.16c})$$

which allows for a fast computation of the specific heat for a larger number of temperatures and magnetic fields.

Bibliography

- [1] S. GLOCKE, A. KLÜMPER, AND J. SIRKER : The density-matrix renormalization group applied to transfer matrices: Static and dynamical properties of one-dimensional quantum systems at finite temperature. *Lecture notes WE-Heraeus summerschool 'Computational Many-Particle Physics'*. Greifswald, 2006. cond-mat/0610689.
- [2] G. S. UHRIG AND H. J. SCHULZ : Magnetic excitation spectrum of dimerized antiferromagnetic chains. *Phys. Rev. B* 54 (14) R9624 (1996). cond-mat/9606001.
- [3] T. BARNES, J. RIERA, AND D. A. TENNANT : $S = \frac{1}{2}$ alternating chain using multiprecision methods. *Phys. Rev. B* 59 (17) 11384 (1999). cond-mat/9801224.
- [4] S. TREBST, H. MONIEN, C. J. HAMER, Z. WEIHONG, AND R. R. P. SINGH : Strong-Coupling Expansions for Multiparticle Excitations: Continuum and Bound States. *Phys. Rev. Lett.* 85 (20) 4373 (2000).
- [5] C. J. HAMER, W. ZHENG, AND R. R. P. SINGH : Dynamical Structure Factor for the Alternating Heisenberg Chain : A Linked Cluster Calculation. *Phys. Rev. B* 68, 214408 (2003). cond-mat/0307517.
- [6] M. MÜLLER, H.-J. MIKESKA, AND N. CAVADINI : Dynamical structure factors for dimerized spin systems. *J. Phys.: Condens. Matter.* 15, 8513 (2003). cond-mat/0312042.
- [7] S. NOTBOHM, D. A. TENNANT, B. LAKE, P. C. CANFIELD, J. FIELDEN, P. KÖGERLER, H.-J. MIKESKA, C. LUCKMANN, AND M. T. F. TELLING :

- Temperature effects on multi-particle scattering in a gapped quantum magnet. *Journal of Magnetism and Magnetic Materials* 310, 1236 (2007).
- [8] C. RÜEGG, B. NORMAND, M. MATSUMOTO, C. NIEDERMAYER, A. FURRER, K. W. KRÄMER, H.-U. G. ARY PH. BOURGES, Y. SIDIS, AND H. MUTKA : Quantum Statistics of Interacting Dimer Spin Systems. *Phys. Rev. Lett.* 95, 267201 (2005).
- [9] T. JOLICOEUR AND O. GOLINELLI : σ -model study of Haldane-gap antiferromagnets. *Phys. Rev. B* 50 (13) 9265 (1994).
- [10] J. P. RENARD, M. VERDAGUER, L. P. REGNAULT, W. A. C. ERKELENS, J. ROSSAT-MIGNOD, AND W. G. STIRLING : Presumption for a quantum energy gap in the quasi-one-dimensional $S = 1$ Heisenberg antiferromagnet $\text{Ni}(\text{C}_2\text{H}_8\text{N}_2)_2\text{NO}_2(\text{ClO}_4)$. *Europhys. Lett.* 3 (8) 945 (1987).
- [11] J. P. RENARD, M. VERDAGUER, L. P. REGNAULT, W. A. C. ERKELENS, J. ROSSAT-MIGNOD, J. RIBAS, W. G. STIRLING, AND C. VETTER : Quantum energy gap in two quasi-one-dimensional $S = 1$ Heisenberg antiferromagnets. *Journal of Applied Physics* 63 (8) 3538 (1988).
- [12] K. DAMLE AND S. SACHDEV : Spin dynamics and transport in gapped one-dimensional Heisenberg antiferromagnets at nonzero temperatures. *Phys. Rev. B* 57 (14) 8307 (1998).
- [13] J. VILLAIN : Propagative spin relaxation in the Ising-like antiferromagnetic linear chain. *Physica B* 79 (1) 1 (1975).
- [14] T. VEKUA, A. HONECKER, H.-J. MIKESKA, AND F. HEIDRICH-MEISNER : Correlation functions and excitation spectrum of the frustrated ferromagnetic spin-1/2 chain in an external magnetic field. cond-mat/0704.0764.
- [15] J. VOIT : A brief introduction to Luttinger liquids. *American Institute of Physics Conference Series*, vol. 544 of *American Institute of Physics Conference Series*, pp. 309–318. 2000.
- [16] F. D. M. HALDANE : General Relation of Correlation Exponents and Spectral Properties of One-Dimensional Fermi Systems: Application to the Anisotropic $S = \frac{1}{2}$ Heisenberg Chain. *Phys. Rev. Lett.* 45 (16) 1358 (1980).
- [17] F. D. M. HALDANE : ‘Luttinger liquid theory’ of one-dimensional quantum fluids. I. Properties of the Luttinger model and their extension to the general 1D interacting spinless Fermi gas. *J. Phys. C* 14 (19) 2585 (1981).

BIBLIOGRAPHY

- [18] T. SAKAI : Phase Transition of $S = \frac{1}{2}$ Bond-Alternating Chain in a Magnetic Field. *J. Phys. Soc. Jpn.* 64 (1) 251 (1995).
- [19] A. FRIEDRICH, A. K. KOLEZHUK, I. P. MCCULLOCH, AND U. SCHOLLWÖCK : Edge singularities in high-energy spectra of gapped one-dimensional magnets in strong magnetic fields. *Phys. Rev. B* 75, 094414 (2007). cond-mat/0611772.
- [20] K. TAKANO, K. KUBO, AND H. SAKAMOTO : Ground states with cluster structures in a frustrated Heisenberg chain. *J. Phys.: Condens. Matter.* 8 (35) 6405 (1996).
- [21] B. SUTHERLAND AND B. S. SHASTRY : Exact Solution of a Large Class of Interacting Quantum Systems Exhibiting Ground State Singularities. *J. Stat. Phys.* 33, 477 (1983).
- [22] K. OKAMOTO, T. TONEGAWA, Y. TAKAHASHI, AND M. KABURAGI : The ground state of an $S = \frac{1}{2}$ distorted diamond chain—a model of $\text{Cu}_3\text{Cl}_6(\text{H}_2\text{O})_2 \cdot 2\text{H}_8\text{C}_4\text{SO}_2$. *J. Phys.: Condens. Matter.* 11, 10485 (1999).
- [23] T. TONEGAWA, K. OKAMOTO, T. HIKIHARA, Y. TAKAHASHI, AND M. KABURAGI : Ground State Properties of an $S = \frac{1}{2}$ Distorted Diamond Chain. *J. Phys. Soc. Jpn.* 69 (A) 332 (2000). cond-mat/9912482.
- [24] K. SANO AND K. TAKANO : Spin Gap of $S = \frac{1}{2}$ Heisenberg Model on Distorted Diamond Chain. *J. Phys. Soc. Jpn.* 69 (8) 2710 (2000).
- [25] H. KIKUCHI, Y. FUJII, M. CHIBA, S. MITSUDO, T. IDEHARA, T. TONEGAWA, K. OKAMOTO, T. SAKAI, T. KUWAI, AND H. OHTA : Experimental Observation of the $\frac{1}{3}$ Magnetization Plateau in the Diamond-Chain Compound $\text{Cu}_3(\text{CO}_3)_2(\text{OH})_2$. *Phys. Rev. Lett.* 94, 227201 (2005).
- [26] H.-J. MIKESKA : Private communication.
- [27] K. OKAMOTO AND K. NOMURA : Fluid-dimer critical point in $S = \frac{1}{2}$ antiferromagnetic Heisenberg chain with next nearest neighbor interactions. *Phys. Lett. A* 169 (6) 433 (1992).
- [28] J. H. WILKINSON AND C. REINSCH : *Linear Algebra*. No. 186 in Die Grundlehren der mathematischen Wissenschaften in Einzeldarstellungen. Berlin : Springer-Verlag, 1971. ISBN 3-540-05414-6.

- [29] T. BARNES AND J. RIERA : Susceptibility and excitation spectrum of $(\text{VO})_2\text{P}_2\text{O}_7$ in ladder and dimer-chain models. *Phys. Rev. B* 50 (10) 6817 (1994).
- [30] S. BREHMER, A. K. KOLEZHUK, H.-J. MIKESKA, AND U. NEUGEBAUER : Elementary excitations in the gapped phase of a frustrated $S = \frac{1}{2}$ spin ladder: from spinons to the Haldane triplet. *J. Phys.: Condens. Matter.* 10, 1103 (1997). cond-mat/9710114.
- [31] J. DES CLOIZEAUX AND J. J. PEARSON : Spin-Wave Spectrum of the Antiferromagnetic Linear Chain. *Phys. Rev.* 128 (5) 2131 (1962).
- [32] K. DAMLE AND S. SACHDEV : Universal Relaxational Dynamics of Gapped One-Dimensional Models in the Quantum Sine-Gordon Universality Class. *Phys. Rev. Lett.* 95 (18) 187201 (2005).
- [33] H. DE RAEDT, S. MIYASHITA, AND M. K. : Magnetic energy-level diagrams of high-spin (Mn_{12} -acetate) and low-spin (V_{15}) molecules. *Physica Status Solidi (B)* 241 (6) 1180 (2004). cond-mat/0306275.
- [34] K. FABRICIUS, U. LÖW, AND J. STOLZE : Dynamic correlations of antiferromagnetic spin- $\frac{1}{2}$ XXZ chains at arbitrary temperature from complete diagonalization. *Phys. Rev. B* 55 (9) 5833 (1997). cond-mat/9611077.
- [35] K. FABRICIUS AND U. LÖW : Dynamical properties of the compound CuGeO_3 and α' - NaV_2O_5 at nonzero temperatures. *Phys. Rev. B* 57 (21) 13371 (1998).
- [36] N. HAGA AND S. ICHIRO SUGA : Dynamical structure factor of $S = \frac{1}{2}$ two-leg spin ladder systems. *Phys. Rev. B* 66, 132415 (2002). cond-mat/0205576.
- [37] K. HIDA AND I. AFFLECK : Quantum vs. Classical Magnetization Plateaus of $S = \frac{1}{2}$ Frustrated Heisenberg Chains. *J. Phys. Soc. Jpn.* 74, 1849 (2005). cond-mat/0501697.
- [38] G. BOUZERAR, A. P. KAMPF, AND G. I. JAPARIDZE : Elementary excitations in dimerized and frustrated Heisenberg chains. *Phys. Rev. B* 58 (6) 3117 (1998). cond-mat/9801046.
- [39] J. KARADAMOGLU AND X. ZOTOS : Diffusive Transport in Spin-1 Chains at High Temperatures. *Phys. Rev. Lett.* 93 (17) 177203 (2004).

BIBLIOGRAPHY

- [40] A. BRÜHL, B. WOLF, V. PASHCHENKO, M. ANTON, C. GROSS, W. ASSMUS, R. VALENTI, S. GLOCKE, A. KLÜMPER, T. SAHA-DASGUPTA, B. RAHAMAN, AND M. LANG : Effects of Two Energy Scales in Weakly Dimerized Antiferromagnetic Quantum Spin Chains. *Phys. Rev. Lett.* 99, 057204 (2007). cond-mat/0703431.
- [41] B. KUMAR : Quantum spin models with exact dimer ground states. *Phys. Rev. B* 66, 024406 (2002).
- [42] H.-J. MIKESKA AND C. LUCKMANN : Finite Temperature Dynamics of the Spin $\frac{1}{2}$ Bond Alternating Heisenberg Antiferromagnetic Chain. *Phys. Rev. B* 73 (18) 184426 (2006). cond-mat/0602387.
- [43] W. ZHENG, C. J. HAMER, R. R. P. SINGH, S. TREBST, AND H. MONIEN : Linked cluster series expansions for two-particle bound states. *Phys. Rev. B* 63, 144410 (2000). cond-mat/0010354.
- [44] T. NIKUNI, M. OSHIKAWA, A. OOSAWA, AND H. TANAKA : Bose-Einstein Condensation of Dilute Magnons in TlCuCl_3 . *Phys. Rev. Lett.* 84 (25) 5868 (2000).
- [45] K. OKUNISHI AND T. TONEGAWA : Magnetic phase diagram of the $S = \frac{1}{2}$ antiferromagnetic zigzag spin chain in the strongly frustrated region : cusp and plateau. *J. Phys. Soc. Jpn.* 72, 479 (2003). cond-mat/0211458.
- [46] K. OKUNISHI AND T. TONEGAWA : Fractional S^z excitation and its bound state around the $\frac{1}{3}$ plateau of the $S = \frac{1}{2}$ Ising like zigzag XXZ chain. *Phys. Rev. B* 68, 224422 (2003). cond-mat/0307121.
- [47] K. OKUNISHI AND T. TONEGAWA : Fractional S^z Excitation and Its Boundstate for the $S = \frac{1}{2}$ Antiferromagnetic Zigzag Spin Chain in a Magnetic Field. *J. Phys. Soc. Jpn.* 74S, 151 (2005).
- [48] M. OSHIKAWA, M. YAMANAKA, AND I. AFFLECK : Magnetization Plateaus in Spin Chains: “Haldane Gap” for Half-Integer Spins. *Phys. Rev. Lett.* 78 (10) 1984 (1997).
- [49] B. S. SHASTRY AND B. SUTHERLAND : Excitation Spectrum of a Dimerized Next-Neighbor Antiferromagnetic Chain. *Phys. Rev. Lett.* 47 (13) 964 (1981).
- [50] M. TAKIGAWA, T. ASANO, Y. AJIRO, M. MEKATA, AND Y. J. UEMURA : Dynamics in the $S = 1$ One-Dimensional Antiferromagnet AgVP_2S_6 via ^{31}P and ^{51}V NMR. *Phys. Rev. Lett.* 76 (12) 2173 (1996).

- [51] D. A. TENNANT, C. BROHOLM, D. H. REICH, S. E. NAGLER, G. E. GRANROTH, T. BARNES, K. DAMLE, G. XU, Y. CHEN, AND B. C. SALES : Neutron scattering study of two-magnon states in the quantum magnet copper nitrate. *Phys. Rev. B* 67, 054414 (2003).
- [52] T. TONEGAWA, K. OKAMOTO, K. OKUNISHI, K. NOMURA, AND M. KABURAGI : Magnetization plateaux in an anisotropic $S = \frac{1}{2}$ antiferromagnetic chain with frustration and bond-alternation. *Physica B* 346-347, 50 (2004).
- [53] K. P. SCHMIDT AND G. S. UHRIG : Excitations in One-Dimensional $S = \frac{1}{2}$ Quantum Antiferromagnets. *Phys. Rev. Lett.* 90, 227204 (2003).
- [54] G. S. UHRIG AND B. NORMAND : Magnetic Properties of $(VO)_2P_2O_7$ from Frustrated Interchain Coupling. *Phys. Rev. B* 58 (22) R14705 (1998).
- [55] A. WEISSE, G. BOUZERAR, AND H. FEHSKE : A new model to describe the physics of $(VO)_2P_2O_7$. *Eur. Phys. J. B* 7, 5 (1998).
- [56] S. BREHMER : *Dynamik linearer Ising-Heisenberg-Antiferromagneten*. Diploma thesis, Universität Hannover, 1994.
- [57] S. BREHMER : *Niederenergetische Anregungen in eindimensionalen Quanten-Antiferromagneten*. Ph.D. thesis, Universität Hannover, 1998.
- [58] I. N. BRONSTEIN AND K. A. SEMENDJAJEW : *Taschenbuch der Mathematik*. 2. ed. Thun, Frankfurt am Main : Verlag Harri Deutsch, 1995. ISBN 3-8171-2002-8.
- [59] A. K. KOLEZHUK : Private communication.

Publications

The subsequent list provides a brief abstract of the publications [7, 42] presenting the scientific work underlying this thesis.

H.-J. MIKESKA AND C. LUCKMANN

Finite Temperature Dynamics of the Spin $\frac{1}{2}$ Bond Alternating
Heisenberg Antiferromagnetic Chain
Physical Review B 73, 184426 (2006)

We present results for the dynamic structure factor of the $S = \frac{1}{2}$ bond alternating Heisenberg chain over a large range of frequencies and temperatures. Data are obtained from a numerical evaluation of thermal averages based on the calculation of all eigenvalues and eigenfunctions for chains of up to 20 spins. Interpretation is guided by the exact temperature dependence in the non-interacting dimer limit, which remains qualitatively valid up to an inter-dimer exchange $\lambda \approx 0.5$. The temperature induced central peak around zero frequency is clearly identified and aspects of the crossover to spin diffusion in its variation from low to high temperatures are discussed. The one-magnon peak acquires an asymmetric shape with increasing temperature. The two-magnon peak is dominated by the $S = 1$ bound state, which remains well defined up to temperatures of the order of J . The variation with temperature and wave vector of the integrated intensity for one-magnon and two-magnon scattering and of the central peak are discussed.

S. NOTBOHM, D. A. TENNANT, B. LAKE, P. C. CANFIELD, J. FIELDEN,
P. KÖGERLER, H.-J. MIKESKA, C. LUCKMANN, AND M. T. F. TELLING
Temperature effects on multi-particle scattering in a gapped quantum magnet,
Journal of Magnetism and Magnetic Materials 310, 1236 (2007)

We report measurements of the temperature effects on the dimerized antiferromagnetic chain material, copper nitrate $\text{Cu}(\text{NO}_3)_2 \cdot 2.5\text{D}_2\text{O}$. Using inelastic neutron scattering we have measured the temperature dependence of the one- and two-magnon excitation spectra as well as the temperature induced one-magnon intra-band scattering in a single crystal. Comparison is made with numerical evaluations of thermal averages based on the calculation for a chain of 16 spins.

Acknowledgements

This thesis would not have been possible without the help of many people whom I owe my utmost thank. Although the task to name every and all of them is doomed to fail from the very beginning, I will nevertheless do my best in doing justice to everyone involved in this thesis.

First and foremost, I would like to express my deepest thank to my supervisor Prof. HANS-JÜRGEN MIKESKA for accepting me as PhD student in his research group and for his unstinting and extensive support. I hardly believe that I could have performed this work without his encouragement and guidance.

In addition, I want to thank Prof. HOLGER FRAHM, who willingly agreed to review this thesis, for his support during my research.

Next, my thank goes to Priv.-Doz. ALEXEI KOLEZHUK for his many suggestions which opened new views on my work and to Prof. ERIC JECKELMANN, who put his Linux cluster at my disposal for numerical calculations.

Speaking of computers, I would also like to thank my fellow system administrators MARTIN MÜLLER, HENNING FEHRMANN, and CARSTEN VON ZOBELTITZ for their collaboration in keeping the institute's computer network running. Furthermore, all three of them took over my work without murmur when I had to concentrate more on physics.

HELGE KREUTZMANN receives my thank for countless interesting conversations during lunch time.

Without MARTIN PAECH, who gave me lots of hints regarding typography, the appearance of this thesis would be much less appealing.

I would like to thank the members of the condensed matter group and the Institute for Theoretical Physics, especially Prof. HANS-ULRICH EVERTS, KLAUS OSTERLOH, JÖRN BRÖER, and ALEXANDER SEEL for lots of discussions, coffee and cakes.

I very much appreciated the grant of computational resources on the JUMP super-computer at the Neumann Institute for Computing at Forschungszentrum Jülich.

Schließlich gehört mein größter Dank meinen geliebten Eltern HANS und RENATE LUCKMANN, die mir diese Ausbildung ermöglicht und mich mit unendlicher Liebe und Geduld unterstützt haben. Ohne sie wäre diese Arbeit undenkbar gewesen.

Curriculum Vitae

Carsten Luckmann

10. 10. 1973 geboren in Hannover

Allgemeine Schulbildung

1980–1984 Stadtschule Wunstorf
1984–1986 Orientierungsstufe, Schulzentrum an der Aue, Wunstorf
1986–1993 Hölty-Gymnasium Wunstorf
1993 Allgemeine Hochschulreife

Wehrdienst

10/1993–06/1994 Wehrdienst in Munster

Hochschulbildung

10/1994–01/2000 Studium der Physik an der Universität Hannover
10/1998–10/1999 Diplomarbeit am Institut für theoretische Physik zum Thema
»Elektromagnetische Pion-Produktion am Nukleon«
01/2000 Diplom in Physik an der Universität Hannover
seit 03/2001 Promotion am Institut für Theoretische Physik der Gottfried
Wilhelm Leibniz Universität Hannover

Index

- A**
azurite, 16, 98, 127
- B**
bond alternating Heisenberg chain, *see* Heisenberg chain, bond alternating
bond state, 21, 32, 126
Brillouin zone, 20
- C**
central peak, *see* excitation, central
characteristic exponent, 48
continuum
 two-magnon, 21
copper nitrate, 16, 125
critical field, 35f, 44, 47
 $\text{Cu}(\text{NO}_3)_2$, 16, 125
cut-off frequency, 32
- D**
degeneracy, 26, 112
density of states, 22
detailed balance, 35
diagonalization
 full, exact, 15, 112, 125, 131ff
diamond chain
 distorted, 16, 97ff, 126
 ferrimagnetic phase, 107
 ground state, *see* ground state, diamond chain
 phase diagram, 100ff
 phase transition, 116
 spin fluid, 16, 102ff, 107ff, 116, 126f
 symmetric, 98f, 102
 tetramer-dimer, 16, 105f, 116, 127
 tetramer-dimerized, 112ff
dimers, 19, 102, 107
 non-interacting, 20, 22ff, 36, 45
dispersion, 36
distorted tetramer, *see* tetramer, distorted
domain wall, 112ff, 127
 propagation, 112f
double peak, 117
dynamic structure factor, *see* structure factor, dynamic
- E**
eigenstates, 21
 diamond chain, 102
 dimer, 22
 distorted tetramer, 100
 symmetric tetramer, 100
excitation
 central, 24ff, 28, 31f, 43ff, 47, 50f, 76, 125f
 one-magnon, 21, 24ff, 28ff, 43ff, 50f, 76, 125f
 two-magnon, 28, 32f, 44f, 49, 126
exclusive structure factor, *see* structure factor, exclusive
- F**
ferromagnon, 37
finite size, 21
finite temperature, 49ff

free spins, 102

G

gap, 20, 26, 30, 35, 116

gapless, 20, 39

ground state, 35f, 45, 47

 diamond chain, 102, 105f

 symmetric tetramer, 100

H

Haldane chain, 30, 36

Hamilton operator, 20, 34f, 97ff, 131f

 diamond chain, 102

 distorted tetramer, 100

Heisenberg chain, 19f, 107ff, 126

 bond alternating, 15, 19ff, 125

 specific heat, *see* specific heat, bond

 alternating Heisenberg chain

 spectrum, 21

 structure factor, *see* structure factor

Hilbert space, 20

Householder algorithm, 132f

I

integrated structure factor, *see* structure factor, exclusive

L

ladder, 36

lattice constant, 19

line shape, 28, 30ff

longitudinal structure factor, *see* structure factor, longitudinal

low energetic subsystem, 102, 107

Luttinger liquid, 39

M

magnetic field, 26, 34ff, 116f, 125f, 132

magnetization, 36, 47, 49ff, 77

magnetization plateau, 16, 102, 107f, 117

magnon, 20, 36

N

neutron scattering, 16, 22, 40, 125

non-interacting dimers, *see* dimers, non-interacting

numerical calculations

 full, exact diagonalization, 21

numerical methods, *see* diagonalization, full, exact, *see* Householder algorithm

 dynamic structure factor, 133ff

 specific heat, 136f

O

one-magnon peak, *see* excitation, one-magnon

P

particle number, 32

partition function, 23

peak, *see* excitation

phase transition, *see* diamond chain, phase transition, 127

plateau, *see* magnetization plateau

S

saturation, 35ff, 44, 47

soliton, 16, 112ff, 127

 propagation, 112

soliton propagation, 127

specific heat

 bond alternating Heisenberg chain, 37ff, 125

 distorted diamond chain, 17, 116f, 126

- non-interacting dimers, 39
- spin fluid, *see* diamond chain, spin fluid
- structure factor
 - dynamic, 16, 21, 23, *see also* structure factor, longitudinal, *see also* structure factor, transverse, 26ff, 125
 - exclusive, 26, 46, 125
 - integrated, *see* structure factor, exclusive
 - longitudinal, 34, 40, 43ff, 49ff, 125
 - transverse, 34, 40, 43ff, 47, 49f, 76ff, 126
- symmetric tetramer, *see* tetramer, symmetric
- symmetry
 - rotational, 34, 40
 - translational, 20f

T

- tetramer, 99
 - distorted, 100
 - symmetric, 99f
- tight binding, 112
- transverse structure factor, *see* structure factor, transverse
- two-magnon peak, *see* excitation, two-magnon

W

- wave function, 35
- wave vector, 20f, 33, 43, 49, 99, 132

Z

- Zeeman, 35, 47, 76, 132
- zero temperature, 47ff